Multifunctional silk: from fabrication to application

Singh, Manish

2020

Multifunctional silk: from fabrication to application

MANISH SINGH | DIVISION OF PURE AND APPLIED BIOCHEMISTRY | LUND UNIVERSITY

Multifunctional silk: from fabrication to application

Manish Singh

LUND
UNIVERSITY

DOCTORAL DISSERTATION

To be publicly defended for the degree of Ph.D. at the Faculty of Engineering Lund University, Sweden, in Lecture Hall B, Kemicentrum, Lund, on Thursday, 5th March 2020 at 1 pm.

Faculty opponent

Prof. Hynd Remita,
Department of Chemistry, Université Paris-Saclay

Organization LUND UNIVERSITY	Document name DOCTORAL DISSERTATION
	Date of issue 5 March 2020
Author(s)	Sponsoring organization

Title and subtitle
Multifunctional silk: from fabrication to application

Abstract

Silk fibers offer untapped internal structures to template the formation of nano-objects and active coatings. So far, access to all or part of the internal and organized structures has been a significant challenge. The aim of the thesis is, therefore, to identify and exploit silk templating ability to create value-added multifunctional hybrid materials with enhanced conductive and catalytic properties. The application of nanotechnology in textiles is limited by the difficulties of loading the textile fibers with nanoparticles (NPs), and by the uncontrolled leakage of the loaded NPs. We first demonstrate using supercritical carbon dioxide (sc-CO_2) impregnation that the four major commercially available Indian silk (mulberry, eri, tasar and muga) could be loaded without leakage with standard gold NPs sized between 5-150 nm.

Next, we developed a one-step synthesis and impregnation of metal oxides in the silk fibers using mild sonication. Here we sonochemically reduce potassium permanganate ($KMnO_4$) to manganese oxide (MnO_2) in silk fibers. The obtained MnO_2-Silk hybrid fibers effectively decomposed hydrogen peroxide (H_2O_2) and oxidized the typical horseradish peroxidase substrates, such as o-phenylenediamine (OPD), and 3,3′,5,5′- tetramethylbenzidine (TMB) in the presence or absence of H_2O_2. The oxidative properties of MnO_2-Silk fiber hybrid showed an enzyme-like behavior for the catalase-like activity, oxidase-like activity, and peroxidase-like activity. The operational stability of the MnO_2-Silk fiber hybrid over ten cycles showed a constant residual activity of about 25-30 % after 2-3 cycles indicating that MnO_2-Silk fiber hybrid could be used as a satisfactory oxidoreductase enzyme mimics. We used potentiometric titration to understand the surface charges on the MnO_2-Silk hybrid materials. We identified the reactive species as $Mn^{4+}_{1-x}Mn^{3+}_{x}O_{2-x}(OH)_x$ with a pK of approximately 5.2.

We further developed an *in-situ* UV-Visible spectroscopy based method to study the mechanism of formation of MnO_2 on a silk film and its associated enzymatic activity. The results suggested a three components route for sonication and auto-reduction (as control) to form MnO_2-Silk from $KMnO_4$. Overall, we found that the smaller size, more mono-dispersed, and deeper buried MnO_2 NPs in silk film prepared by sonication, conferred a higher catalytic activity and stability to the hybrid material.

The dimensions and oxidation states of the MnO_2-Silk hybrid material were determined by the use of X-rays structural and spectroscopic methods: a small-angle X-ray scattering (SAXS), anomalous small-angle X-ray scattering (ASAXS), and near-edge X-ray absorption fine structure (NEXAFS). ASAXS allowed us to analyze the MnO_2 alone. We found that the MnO_2 NP had a size below 20 nm. NEXAFS (pre-peak and main peak) confirms the formation of Mn(IV) oxide.

Finally, we demonstrated that the combination of $scCO_2$ impregnation and sonochemistry could yield new or improved multifunctionality. Here we fabricated a soft working electrode for the simultaneous degradation and detection of hydrogen peroxide (H_2O_2). The multifunctional silk hybrid showed an enzyme-like behavior for the degradation of H_2O_2 with a Km of about 13 mM. Together these studies suggest that judicious access and use of silk internal structures can enhance silk already remarkable properties.

Key words: Silk, Sonochemistry, Supercritical impregnation, Nanofiller, Soft biosensor, Enzyme mimic

Classification system and/or index terms (if any)

Supplementary bibliographical information		Language: English
ISSN and key title		ISBN: 978-91-7422-728-4 (print) ISBN: 978-91-7422-729-1 (pdf)
Recipient's notes	Number of pages 236	Price
	Security classification	

Multifunctional silk: from fabrication to application

Manish Singh

LUND
UNIVERSITY

Cover photo of Lund University by Kennet Ruona

Back photo of a collage of silk diversity by collecting different images from internet

Faculty of Engineering
Pure and Applied Biochemistry, Department of Chemistry

ISBN 978-91-7422-728-4 (print)
ISBN 978-91-7422-729-1 (pdf)

Printed in Sweden by Media-Tryck, Lund University
Lund 2020

Dedicated to my father

Table of Contents

Popular summary

It has been more than 25 years since the discovery of nanoparticles (NPs). They are found now in fields as varied as information technology (IT), defense, cosmetics, medicine, security and textiles. In the latter, applications to control odor and smart embedded electronics dominate.

However, the incorporation of nanoparticles into textile fibers has inevitable drawbacks down- and upstream, for example, NPs leakage and toxic chemical pre-treatment. The leakage, as well as the pretreatment step, harms the environment and humans wearing the garments. Leaked NPs are small enough to be absorbed by the skin and irritate. Inhaling small solid particles can not only cause short-term irritation of the lungs but may also cause long-term lung damage and eventually cancer.

The most commonly used NPs in the textile industry is of silver, titanium, or gold origin. The Gothenburg (Sweden) environmental administration conducted a research and found four washed garments leaked silver NPs to differing degrees. Furthermore, studies have shown that an increased concentration of silver NPs in underground water, sludges, and fertilizer is harmful to humans, aquatic life, plants, and other species. The phenomenon is not limited solely to the textile industry, other sectors too leak NPs with dramatic consequences for public health and the environment.

In 2009, the University of Ulster, Northern Ireland, claimed that NPs, such as titanium dioxide, could induce neurodegenerative disease. They can have an impact on the protein misfolding, causing progressive degeneration and resulting in the death of neuron cells.

In the presented thesis, we advance the state-of-the-art processes to generate and understand leakage-free silk fibers. The process developed, involves the impregnation of gold nanoparticles (Au NPs) as well as the direct synthesis of manganese dioxide (MnO_2) NPs in and on silk fibers. The impregnation of the Au NPs happened under supercritical carbon dioxide ($scCO_2$) conditions. $scCO_2$ is a carbon dioxide (CO_2) state found above the critical pressure of 72.9 atm, and the critical temperature 31.1°C. The process is clean, with no harmful organic solvent wastes.

We applied the $scCO_2$ impregnation method to four varieties of textile silks from India, i.e., mulberry, tasar, eri, and muga. The difference between the tested silks is in the type of worms producing the fiber and the type of leaves they feed on.

Each of the silks was successfully impregnated with the Au NPs for up to 150 nanometers. $scCO_2$ transport properties are the key hereby merely changing the temperature and pressure, one can balance the liquid-like viscosity and the gas-like diffusivity of CO_2 to achieve selective impregnation. In other words, the highly penetrating and softening $scCO_2$ helped expand the silk fibers, and eventually, to load the gold nanoparticles. Upon return to atmospheric conditions, the Au NPs were permanently trapped in the silks, without sacrificing any of the texture or other properties of silk.

The second process involved the directed synthesis of MnO_2 in and on the silk fibers, using a mild sonication procedure. The primary motivation was to fabricate a hybrid material made of silk and MnO_2 to create artificial enzymes.

Typically, natural enzymes mediate every biological process in living organisms, and they are capable of accelerating the rate of specific chemical reactions at very high speeds for specific substrates and reactions. However, enzymes' industrial applications are hindered by their fragile nature and high production cost. Thus, there is a need for the discovery and development of artificial enzymes. More precisely, cheap, versatile and reusable enzyme mimics are highly sought after in application, where robustness, cost, and reusability are critical. Typical examples include water decontamination, commodity chemical production, food, pharma, and fuel cells. Recently, researchers have made tremendous progress in designing nano-materials with similar functions as natural enzymes. These nanomaterials show several advantages compared to natural enzymes, such as reusability, low cost, tenability and high stability under adverse conditions.

In this thesis, we develop a one-step method to produce stable enzyme mimics, using a green approach to combine silk fibers and MnO_2 NPs. The new hybrid material shows excellent oxidative capability in removing model organic dyes, breaking peroxide and, most interestingly, excellent reusability. The same protocol tested on waste silk from the silk industry showed good promise. The possibility of using waste silk opens a cost-effective way for the production of smart textiles and other value-added silk-based materials.

The challenge is, however, to understand why silk is so successful at controlling the metal oxide particle formation, its stability and long-lasting catalytic activity.

The in-depth characterization work combines laboratory-based and advanced instruments at large-scale facilities, here, the synchrotron light source at BESSY II in Berlin. The combination of techniques helped explain the molecular mechanism of MnO_2-silk NP fabrication and activity.

For the laboratory-based method, we developed an *in situ* method to determine the mechanism of formation of MnO_2 on silk membranes and monitor its enzymatic activity. We anticipate that other metal oxide (Fe, Cu, Ce, Zn, niobium nitride or molybdenum diselenide) formations and catalytic activities can be studied using the same method. The aim is to mimic other enzymes' catalytic modalities and broaden the applications to, for example, self-cleaning, catalysis,

semiconducting, superconducting or light-emitting properties, chemical sensors, and fuel cells.

For the advanced characterization at large-scale facilities, we found that silk as a protein helps form only small MnO_2 NPs (less than 20 nanometres in size), in stabilizing pockets. As a result, the MnO_2 in silks appeared as better and reusable catalysts as compared to pure MnO_2 NPs.

Finally, we tested the hypothesis that with the correct processing methods, one should be able to build multiple functionalities in the silk fibers with minimum damage. We focused on creating silk fibers that are simultaneously conductive and catalytic for applications in soft electronics.

Until now, conductive and flexible natural textile fibers were difficult to produce, due to the existing methods of fabrication yielding the uncontrolled formation of the conductive layer on the fiber or textile. We developed, therefore, a two steps scalable protocol: (i) to fabricate silk fibers with good conductivity and flexibility needed for fabric weaving or other smart fibers or textile applications, and (ii) to add a catalytic MnO_2 to the already conductive fibers. The first step involves $scCO_2$ aided-impregnation of pyrrole monomers, followed by oxidative polymerization of the pyrrole into highly linear and conductive poly-pyrrole.

The second step involves mild sonication. Here we synthesized MnO_2 NPs on the already conductive silk fibers. This remarkable double and independent templating feature of silk fibers, provide an easy route to tailor catalytic properties and electrical properties. We describe, for the first time, a combined approach to build multifunctionality and achieve enhanced conductivity and catalytic efficiency in silk fiber. We show that the final fiber works as a soft sensor to detect and remove hydrogen peroxide.

Overall, with our novel synthetic and characterization methods, we can solve the problem of leakage from the silk textile industry, build multi-functionalities in silk fiber and produce cost-effective disposable soft biosensors. Future research could focus on generalizing our approach to other natural polymers.

Abstract

Silk fibers offer untapped internal structures to template the formation of nano-objects and active coatings. So far, access to all or part of the internal and organized structures has been a significant challenge. The aim of the thesis is, therefore, to identify and exploit silk templating ability to create value-added multifunctional hybrid materials with enhanced conductive and catalytic properties. The application of nanotechnology in textiles is limited by the difficulties of loading the textile fibers with nanoparticles (NPs), and by the uncontrolled leakage of the loaded NPs. We first demonstrate using supercritical carbon dioxide (sc-CO_2) impregnation that the four major commercially available Indian silk (mulberry, eri, tasar and muga) could be loaded without leakage with standard gold NPs sized between 5-150 nm.

Next, we developed a one-step synthesis and impregnation of metal oxides in the silk fibers using mild sonication. Here we sonochemically reduce potassium permanganate ($KMnO_4$) to manganese oxide (MnO_2) in silk fibers. The obtained MnO_2-Silk hybrid fibers effectively decomposed hydrogen peroxide (H_2O_2) and oxidized the typical horseradish peroxidase substrates, such as o-phenylenediamine (OPD), and 3,3′,5,5′- tetramethylbenzidine (TMB) in the presence or absence of H_2O_2. The oxidative properties of MnO_2-Silk fiber hybrid showed an enzyme-like behavior for the catalase-like activity, oxidase-like activity, and peroxidase-like activity. The operational stability of the MnO_2-Silk fiber hybrid over ten cycles showed a constant residual activity of about 25-30 % after 2-3 cycles indicating that MnO_2-Silk fiber hybrid could be used as a satisfactory oxidoreductase enzyme mimics. We used potentiometric titration to understand the surface charges on the MnO_2-Silk hybrid materials. We identified the reactive species as $Mn_{1-x}^{4+}Mn_x^{3+}O_{2-x}(OH)_x$ with a pK of approximately 5.2.

We further developed an *in-situ* UV-Visible spectroscopy based method to study the mechanism of formation of MnO_2 on a silk film and its associated enzymatic activity. The results suggested a three components route for sonication and auto-reduction (as control) to form MnO_2-Silk from $KMnO_4$. Overall, we found that the smaller size, more mono-dispersed, and deeper buried MnO_2 NPs in silk film prepared by sonication, conferred a higher catalytic activity and stability to the hybrid material.

The dimensions and oxidation states of the MnO_2-Silk hybrid material were determined by the use of X-rays structural and spectroscopic methods: a small-

angle X-ray scattering (SAXS), anomalous small-angle X-ray scattering (ASAXS), and near-edge X-ray absorption fine structure (NEXAFS). ASAXS allowed us to analyze the MnO_2 alone. We found that the MnO_2 NP had a size below 20 nm. NEXAFS (pre-peak and main peak) confirms the formation of Mn(IV) oxide.

Finally, we demonstrated that the combination of $scCO_2$ impregnation and sonochemistry could yield new or improved multifunctionality. Here we fabricated a soft working electrode for the simultaneous degradation and detection of hydrogen peroxide (H_2O_2). The multifunctional silk hybrid showed an enzyme-like behavior for the degradation of H_2O_2 with a Km of about 13 mM. Together these studies suggest that judicious access and use of silk internal structures can enhance silk already remarkable properties.

Abbreviations

ASAXS	Anomalous small-angle x-ray scattering
ATR-FTIR	Attenuated total reflectance Fourier transform infrared spectroscopy
Ag NP	Silver nanoparticle
Au NP	Gold nanoparticle
H_2O_2	Hydrogen peroxide
$KMnO_4$	Potassium permanganate
MB	Methylene blue
MnO_2	Manganese dioxide
MnOx	Manganese oxides
NEXAFS	Near edge x-ray absorption fine structure
NP	Nanoparticle
OPD	o-phenylenediamine dihydrochloride
PPy	Polypyrrole
SEM	Scanning electron microscopy
SAXS	Small-angle x-ray scattering
$ScCO_2$	Supercritical carbon dioxide
SCF	Supercritical fluid
TiO_2	Titanium dioxide
TMB	3,3′,5,5′-Tetramethylbenzidine
UV-Vis	Ultraviolet-visible
XRD	X-ray powder diffraction

List of papers

Paper 1. **Manish Singh**, Estera S. Dey, Sunil Bhand and Cedric Dicko. Gold NPs uptake and reduced leakage dependent on access to size-dependent internal volumes in silk fibers (Submitted to supercritical journal).

Paper 2. **Manish Singh**, Chris Musy, Estera S. Dey, and Cedric Dicko. Rapid fabrication and optimization of silk fibers supported and stabilized MnO_2 catalysts. Fibers and Polymers 2017, Vol.18, No.9, 1660-1670.

Paper 3. **Manish Singh**, Estera S. Dey, and Cedric Dicko. Manganese oxide functionalized silk fibers for enzyme mimics application (Manuscript form).

Paper 4. **Manish Singh**, Kishan Bharadwaj, Estera S. Dey, and Cedric Dicko. Sonication enhances the stability of MnO_2 NPs on silk films template for enzyme mimic applications (Submitted to Ultrasonics sonochemistry).

Paper 5. Raul Garcia-Dieza, **Manish Singh**, Christian Gollwitzer, Estera Dey, Michael Krumrey, Cedric Dicko. Biomorphic manganese partition in catalytic silk by the combination of X-ray analytical methods (manuscript form).

Paper 6. **Manish Singh**, Paulo Bollella, Lo Gorton, Estera S. Dey, and Cedric Dicko, Conductive and enzyme-like silk fibers for soft sensing application, Biosensors, and Bioelectronics, (2019) 111859.

My contribution to the papers

Paper 1. I designed, planned and performed all the experiments. I wrote the first draft of the manuscript, which was then revised and edited together with the co-authors.

Paper 2. Chris Musy and I performed all the experiments. I wrote the first draft of the manuscript, which was then revised and edited together with the co-authors.

Paper 3. I designed, planned and performed all the experiments. I wrote the first draft of the manuscript, which was then revised and edited together with the co-authors.

Paper 4. Kishan Bharadwaj and I performed all the experiments. I wrote the first draft of the manuscript, which was then revised and edited together with the co-authors.

Paper 5. Raul Garcia-Diez performed the SAXS, ASAXS and NEXAFS and other x-ray spectroscopic methods. The data was analyzed, interpreted and written up by all the co-authors.

Paper 6. I designed, planned and performed all the experiments. The cyclic voltammetry experiments were performed together with Paolo Bollella. I wrote the first draft of the manuscript, which was then revised and edited together with the co-authors.

Introduction

The textile industry is likely to be one of the most polluting in the world. The reason which makes the life cycles of textile products unsustainable is the use of conventional chemical processing or wet processing methods [1-5]. This conventional wet processing of textiles, such as pre-treatment, dyeing and chemical finishing are expensive, environmentally unsafe and thus, can significantly affect the final performance of the treated textiles [1, 2]. A large body of research addresses the development of eco-friendly textile processing techniques, e.g., nano-, bio-, plasma technologies, which could lower their toxicity, replace harsh chemicals and avoid generation of effluents and adverse harmful effects on the environment. This can be done by lowering the usage of materials, water and energy consumption, which ultimately lowers the cost and upgrades the performance and functional properties of a textile [6]. However, bio- and plasma-based technologies can be complicated and costly, so, the economic aspect should be considered before using such techniques [4]. In order to achieve improved fabric functionalities and performance properties, the research interest is increasingly inclining towards using nanotechnology [7-10]. More repeatability, reliability, and robustness are some of the main advancements of using nanotechnological aspects in textiles [10].

In recent years, the development of textile-based nanocomposites has been an area of high scientific activities and industrial interest, due to added functionalities from the combination of textiles with an inorganic nanofiller. The primary purpose of adding nanofillers in textiles is to increase the mechanical strength and improve physical properties, such as electrical conductivity and antistatic behavior. Furthermore, it also enhances functionalities such as anti-microbial, UV protection, flame retardance, self-cleaning, controlled hydrophilicity or hydrophobicity, and protection against fire [11-15]. Additionally, the homogeneous distribution of nanofiller in polymer matrices can increase the composite toughness and abrasive resistance [16-18]. Extra functionalities imparted to composite fibers vary with specific properties of the nanofillers used, as mentioned in Figure 1.

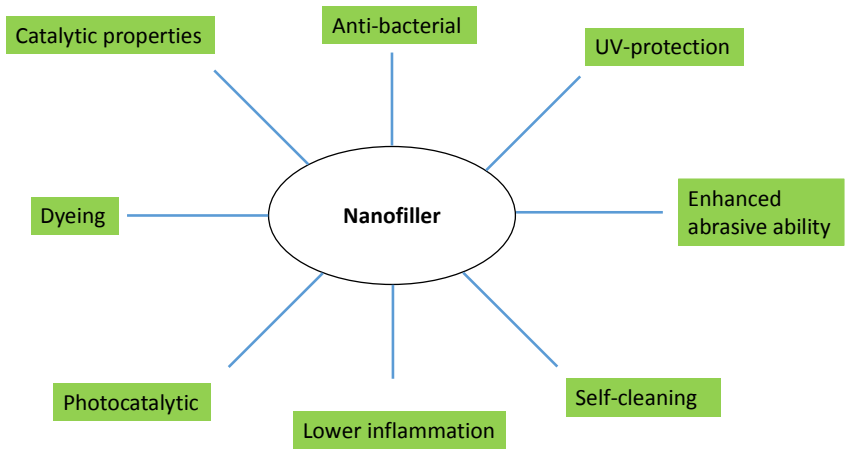

Figure 1.
Some possibilities of textile functionalization by nanofiller.

Despite the fact, some micro-size filler particles, such as clay, metal oxides and carbon black, have previously been used in making polymer-based composite materials for decades, reducing their size into nanometre scales, resulting in better performances and new market interest. There are several ways of distribution of nanofillers in polymer matrices, through mechanical and chemical approaches. State of the art methods for natural fibers modification (e.g., cotton, silk) include plasma treatment [19], *in situ* synthesis [20], solvothermal synthesis [21], chemical assembly [22], deposition [23], merely dipping the textile into nano-particulate dispersion [21] and subsequent padding and drying [24, 25] and sonochemical reduction [26].

The above methods have their drawbacks, such as decreases in the tensile strength of the fibers, the ability to disperse nanofillers homogenously, energy-intensive, excessive use of water, hazardous solvents and effluents, harsh chemical pre-treatment and leakage of NPs from the fiber after multiple washes [27-29]. These limitations may lead to serious environmental and health issues. More specifically, the existing methods to produce silk fibers or textile nanocomposite materials cannot overcome the challenge of obtaining a uniformly distributed nanofiller with a lower environmental impact and leakage.

It is clear that the ability to produce functional textiles with the desired properties, employing the existing production methods, is rather insecure and may never represent a serious alternative for the existing manufacturing methods. The principal aim of this thesis is, therefore, to develop multifunctional silk using green and scalable technologies, such as $scCO_2$ and sonochemistry. To accomplish this aim, we have considered the following objectives presented in the next section.

Objectives

- To utilize supercritical carbon dioxide ($scCO_2$) to access the fiber interior
- To utilize sonication for metal oxides nanoparticles (NPs) synthesis
- To understand the mechanism of formation of metal oxide NPs in the presence of silk
- To characterize the metal oxide NPs on silk fiber
- To fabricate multifunctional fibers for sensing (conductivity and catalysis)

Thesis structure Outline

This thesis contains five chapters.

Chapter 1 describes the general overview of silk-based hybrid materials: synthesis, characterization, and applications.

Chapter 2 highlights challenges in regard to the leakage of nanoparticles (NPs) from textiles and focuses on the available space in silk fiber for NPs loading. The outcome of this chapter is demonstrated by using standardized gold NPs of various sizes and highlights that supercritical fluid impregnation provides a safe and sustainable route for gold NPs loading without leakage (**Paper 1**).

In Chapter 3, we characterize MnO_2-Silk as an enzyme mimic, exhibiting the typical Michaelis–Menten kinetics and a high affinity for catalase, oxidase and peroxidase substrates. The pk spectra helped identify the charges of the MnO_2 NPs on the silk fiber and understand the interaction of the MnO_2-silk hybrid material with H_2O_2, TMB and OPD substrates. (**Paper 3**). Additionally, we demonstrate the mechanism of formation of MnO_2 on a silk film and its associated enzymatic activities, using *in situ* UV-visible spectroscopy (**Paper 4**). Furthermore, we characterize the MnO_2-Silk hybrid material using x-ray structural and spectroscopic methods, such as small-angle x-ray scattering (SAXS), anomalous small-angle x-ray scattering (ASAXS) and near-edge x-ray absorption fine structure (NEXAFS), to examine the structural integrity (SAXS), the average size of the metal oxides (SASX), the dimensions of the metal oxides (ASAXS) and the metal ion oxidation state (NEXAFS) (**Paper 5**).

In Chapter 4, we describe how to engineer multifunctionality using a combination of $scCO_2$ and sonication to form a polypyrrole (PPy)-MnO_2-silk hybrid. We found that the resulting hybrid fiber acted as a soft working electrode for the simultaneous degradation and detection of H_2O_2 (**Paper 6**).

In Chapter 5, we summarize chapters 2, 3 and 4, with an emphasis on achieved results, methods and techniques used and current limitations. Furthermore, we focus on the future perspectives of this study.

Chapter 1. Silk-based hybrid materials: synthesis, characterization, and applications

Silk is a protein-based natural polymer present in the glands of arthropods such as silkworms, spiders, scorpions, mites and bees. Silk is later spun into fibers during their metamorphosis stage [30]. The silk fibers collected from different arthropods show variation in their composition, structure and properties [30-33]. Silk from silkworms has been discussed extensively in the literature due to its extraordinary features such as unique biodegradability and biocompatibility, strong mechanical strength, tunable degradation, ease of processing, adequate supply [34]. The stable physical and chemical properties, unique biodegradability and biocompatibility make it a very promising biomaterial [35-37]. Silk fibers have a complex structural and chemical composition, which consists of different kinds of amino acids, among which the content of glycine (43~46%), alanine (25~30%) and serine (12%) composes about 80% of the total amino acid [31-33]. Silk fiber from silkworms consist of two primary proteins: the outer layer called sericin and fibroin, as illustrated in Figure 2 [34]. Sericin is a glue-like amorphous protein, which is water-soluble and can be removed through the degumming process, often during the cocoon unwinding using hot water. It is placed across the surface of two parallel fibroin fibers, which helps in binding the fibroin fiber together and keeping the structural integrity of the fibers (Figure 2) [30, 34, 38].

In contrast to sericin, silk fibroin is the primary component of the silk fiber with a semi-crystalline structure that provides stiffness and strength. Silk fibroin is composed of numerous minute fibrils, which can be separated into crystalline (β-sheet crystals with strong hydrogen bonding) and amorphous regions (with varying degrees of hydrogen bonding) (Figure 2) [34]. The amino acid sequence in the crystalline region of the silk fibroin is mainly composed of glycine residues, alternating with alanine and serine. The sequence in the amorphous region of the silk fibroin contains a tyrosine-rich domain [36, 37, 39].

The structure of silk fibroin consists of a heavy (H) chain (~390 kDa) and a light (L) chain (~26 kDa), which are further linked with a single disulfide bond at the C-terminus of the H-chain, making an H–L complex [34, 40]. Furthermore, a glycoprotein P25 (~25 kDa) is non-covalently bonded to the H–L complex. The H-chain, L-chain and P25 are gathered in a ratio of 6:6:1 to form silk [34, 40].

Three structural terminologies, such as silk I, II and III, have been reported in the literature to exist in silk fibroins. Silk I is a water-soluble structure and contains a random coil and α-helix, and the silk II structures are insoluble and mainly contain antiparallel β-sheet structure (Figure 2), whereby the antiparallel β-sheet energy is the lowest and, thus, the most stable [33, 35-37, 39]. The strong hydrogen bonds between adjacent segments of silk II contribute significantly to the stiffness and strength of silk fibroins. Silk III is an unstable structure observed at the water-air interface [34]. The silk I structure can be changed to a silk II through treatment with organic solvents, such as methanol [41, 42]. To form water-soluble silk fibroins, degummed silk fiber undergoes dissolution using concentrated salt solutions, resulting in a non β-sheet state fibroin solution which is further dried to form stable, less ordered, noncrystalline, silk fibroin films, hydrogels and sponges, with different structures ranging across the nano-, micro- and macro-scale [43, 44].

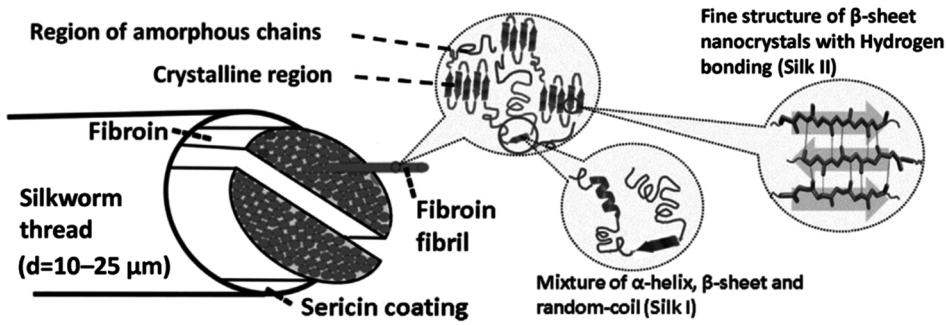

Figure 2.
Illustrative representation of the silk fibroin structure highlights the diameter of a single silkworm thread. Reproduced from [34].

There are different varieties of available commercial silk produced from the silkworms, namely mulberry, tasar, eri, and muga. All these types of silk differ in their physical characteristics and structures [45, 46]. For example, mulberry has the highest density, indicating a relatively more compact structure compared to the non-mulberry fibers; it has more oriented structures. However, their birefringence values are not significantly different from one another [47]. When comparing their microstructural parameters and mechanical properties, a significant difference among these varieties is observed. Microstructural parameters, such as crystallinity, density, etc., have a direct correlation with mechanical properties [47]. Table 1 summarizes the different varieties of silk with their most salient chemical and physical properties [45, 47-50]. Knowing silk properties will help us understand or predict chemical interactions with other materials.

Table 1. Silk properties

	Mulberry	Eri	Muga	Tasar
Average density (g/cm^3)[a]	1.357	1.288	1.34	1.323
Average moisture regain (%)[a]	7.04	8.03	7.61	8.52
Sericin content (%)[b]	10.4 – 24.4	6.5 – 10.1	8.6 – 12.7	8.2 – 14.4
Acid dye exhaustion (%)[c]	89.82	58.38	57.02	59.10
Disperse dye exhaustion (%)[d]	23.67	13.55	12.59	16.20
Elongation (%)	13.5	20.8	22.3	26.5
Tenacity (g/d)[e]	3.75	3.7	4.35	4.5
Initial modulus (g/d)	95	89	81	84
X-ray crystallinity (%)	38.2	32.6	35.0	35.2
Glass transition (˚C) [f]	200 – 220	220 – 235	215 – 235	235 - 250
Basic/Acidic ratio [g]	0.65	1.3	1.24	0.97
Hydrophilic/hydrophobic ratio [g]	0.28	0.35	0.38	0.44
Bulky/non bulky side groups ratio [g]	0.17	0.24	0.28	0.33
Glycine/Alanine ratio [g]	1.58	0.8	0.82	0.81

[a] average of outer, middle and inner silk cocoons layers
[b] low and high sericin content in fibers (from reference [24])
[c] Texacid fast red A (acid dye)
[d] Foron scarlet S-3GFL (disperse dye)
[e] g/d: gram per denier
[f] from references [45, 50]
[g] from reference [24]. Adapted from **Paper 1.**

Silk hybrid based on nanomaterials

Hybrid materials incorporate both organic and inorganic constituents. It is emerging as a promising class of materials due to the diverse and complementary nature of the properties inherited by its organic and inorganic constituents.
With the integration of nanomaterials with silk, new features are being discovered, which are different from its conventional applications, based on the uniquely small size and surface effects [22, 24, 51-53]. Upon addition of specific functional inorganic nanomaterials to the silk fiber surface, the obtained natural fibers will exhibit the combined properties of the original components, resulting in silk hybrid-based nanomaterials. The development represents an emerging and interdisciplinary topic at the border of the textile field, material sciences and nanotechnology.

In this regard, the mixing of both organic and inorganic constituents are done to improve properties or to gain additional functionalities in the resultant hybrid materials. These hybrid materials are garnering a considerable amount of interest, due to their versatile applications in important areas such as catalysis, biosensor, wearable device, ultraviolet (UV) blocking ability and antibacterial activity [22, 52, 54-56].

Literature shows several strategies or approaches to make functional silk fiber-based nanomaterial with post-modification, or *in situ* modifications of silk fibers [22, 24, 51-53, 55, 57-62]. The *in situ*-modification approach has been developed to make functional silk hybrid nanomaterials via feeding silkworms. This approach shows that nanomaterials can enter silk through the silkworm's metabolism [57-59]. The final silk nanomaterials' composite possesses not only excel in functional properties but also exhibit excellent mechanical properties and thermal stability [57-59, 63]. Nanomaterials such as silver NPs, iron oxide (Fe_3O_4), carbon nanotubes, graphene and titanium dioxide (TiO_2) have been used for feeding silkworms [57-59, 63]. However, a significant challenge is about finding the right dose, achieving high efficiency of the process, and it is also a considerable challenge to keep silkworms healthy during the feeding period. Furthermore, the scale-up of the processes from small-scale rearing laboratory experiments to large-scale poses a great challenge [63].

The post-modification approach can produce functional silk fiber-based nanomaterials from regenerated silk fibroin solutions by using wet spinning, dry spinning and electrospinning processes [55, 60-62]. Here, NPs such as carbon nanotubes, graphene, nano titanium oxide, gold NPs (Au NPs), silver (Ag) NPs, MnO_2, carbon nanotubes, graphene oxide are added to the regenerated silk protein solution, and then the regenerated silk based nanomaterial composite fiber was obtained via dry- or wet-spinning [55, 60-62].

However, compared with natural silk fiber, the obtained regenerated silk fiber was brittle, weaker, possessed lower mechanical properties and showed no spinning ability, hindering the scope and area of its application. Additionally, this post modification approach is difficult to control, as it involves a complex multistep preparation.

Another post modification approach is to functionalize the silk fiber surface with nanomaterials, using a physical and chemical process. For instance, many metal or metal oxide NPs such as MnO_2, TiO_2, Ag NPs, zinc oxide (ZnO) and Fe_3O_4 NPs have been successfully used to prepare metal/metal oxide NPs coated silk fibers. Moreover, this functionalized silk was endowed with remarkable catalytic UV protection, antimicrobial and magnetic properties. New functions lead to new applications of silk fiber and improve the added value of natural silk. Different synthetic procedures are being used to functionalize silk with nanomaterials, including laser ablation, auto-reduction, hydrothermal methods and synthesis using polyelectrolytes, sol-gel synthesis, chemical assembly, deposition, dip coating, self-assembly and thermal reduction via electrostatic force [21, 24, 51-53, 64-67].

The above coating methods have drawbacks, specifically a decrease in the tensile strength of the fibers, excessive use of water, hazardous solvents and effluents, and the process demands harsh chemical pre-treatment and leakage of NPs from the fiber after multiple washes. Furthermore, these typical methods do not prevent

or reduce the wash fastness of the hybrid silk. Consequently, large amounts of potentially toxic compounds are leaked into the environment, which may lead to serious environmental and health issues. The limiting factor is the undefined available space in silk or textiles fibers for functionalization with NPs. The above limitation clearly shows the need for an environmentally friendly approach to produce silk based nanomaterials.

In my doctoral research, I used sustainable and scale-up technologies, such as supercritical carbon dioxide ($scCO_2$) and sonication, to optimize the manufacturing process of silk-based nanomaterials, followed by a thorough analysis of the structure, properties and application of this novel functional silk-based nanocomposites. Chapter 2 and Chapter 3 focus on the development of a sustainable route to solve the problem of nanofillers leakage, stabilization of nanofiller in silk fibers and understanding of the chemistry of catalysts in functional silk fibers with the desired properties.

Different experimental methods have been used in different phases of the thesis project. We can broadly divide the experiments into two parts, namely the procedures for the preparation of silk-based hybrid composite and the different techniques used for the characterization of these composites.

Methods

Gold nanoparticle (Au NPs)-Silk fiber

Preparation of silks fibers to be impregnated with Au NPs

A bundle of fibers was weighed (0.051 ± .003 g) and gently rinsed twice with 10 ml of double-distilled water and dried at room temperature for 12 h on the lab bench. The dry silk fibers were then immersed in 10 mL of reacting solution (water and NPs) in a 20 ml glass vial. In all experiments, we used aluminum foil to cover the glass vial and magnetic bars to mix the solutions.

Impregnation of silk fibers under supercritical and atmospheric conditions

The $scCO_2$ impregnation was performed in a modified SFE-100 from Thar Technologies, Inc. (Pittsburg, PA). Figure 3 illustrates the experimental apparatus. It consisted of a steel reaction vessel of 100 ml volume, immersed in a thermostated water bath (see temperature details in the results section) with a magnetic stirrer. The glass vial (20 ml) was inside the reaction vessel. To reach the desired pressure, the CO_2 was pumped in at 11 grams per minute. For the impregnation of the four silks, the temperature was kept at 40°C and the pressure at 200 bars. For the detailed study of the impregnation using the fully degummed mulberry silk, the final pressures and temperatures were adjusted according to the

experimental design table. The control impregnation happened at atmospheric pressure and at the corresponding temperature and time, to match the supercritical conditions. The magnetic agitation speed of impregnation was kept constant at 300 rpm. Figure 4 shows the impregnation of Au NPs into silk fibers using $scCO_2$ and control.

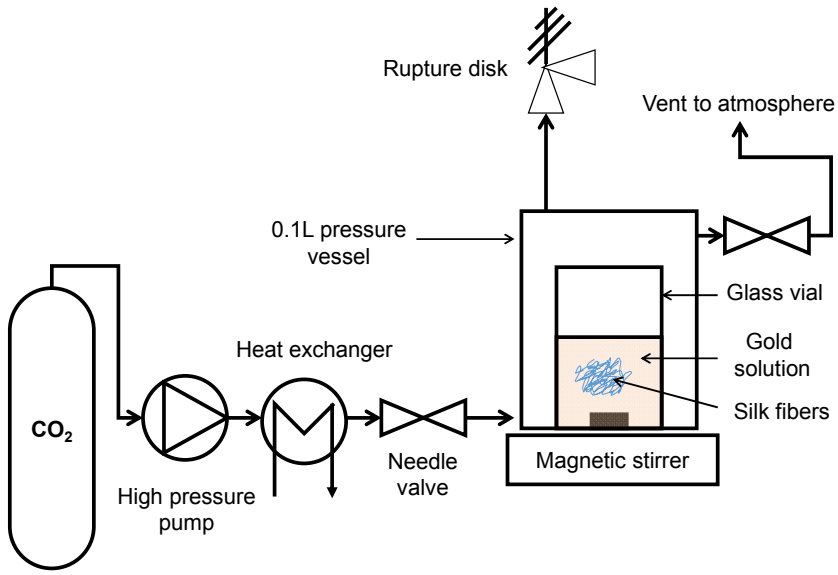

Figure 3.
Schematic diagram of supercritical CO_2 set up. Briefly, when reaching supercritical conditions, the water and Au NPs become a ternary mixture of water/Au NPs/$scCO_2$. The new mixture has enhanced diffusion and interfacial properties allowing the Au NPs to be transported in the fibers. Adapted from **Paper I.**

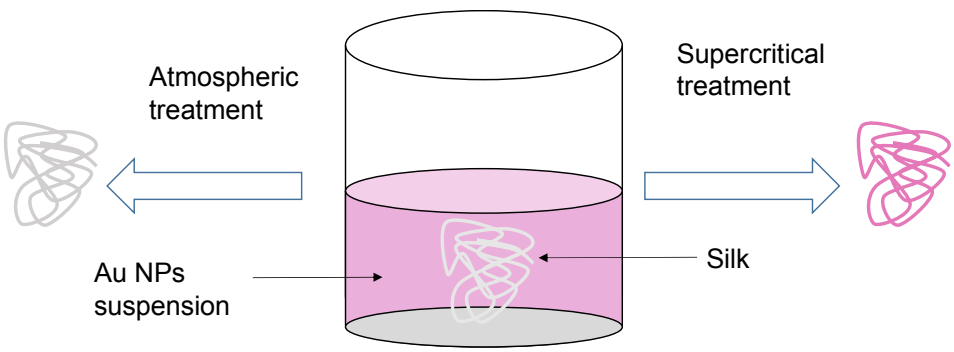

Figure 4.
Schematic showing the impregnation of gold nanoparticles (Au NPs) on silk fiber using supercritical carbon dioxide ($scCO_2$) and atmospheric treatment (control).

MnO_2 NPs-Silk fiber

In-situ synthesis of MnO_2 NPs on silk fiber using sonication

Approximately 0.1 g of silk yarn (fibers of mulberry, tasar, eri, and muga) was submerged in 10 ml of $KMnO_4$ solution (5 mM, 10 mM, and 20 mM) in a 20 ml glass vial. Without delay, the reaction mixture was irradiated with ultrasound waves (for 20 min, 45 min, 150 min, and 360 min) using a Bandelin sonorex sonication bath at 35 kHz and 320 W. The temperature of the bath was not controlled, except otherwise stated. After irradiation, the modified fibers were removed from the glass vial and washed thoroughly with deionized water and air-dried overnight at room temperature. The supernatant was further characterized by UV absorbance to determine the fraction of $KMnO_4$ consumed.

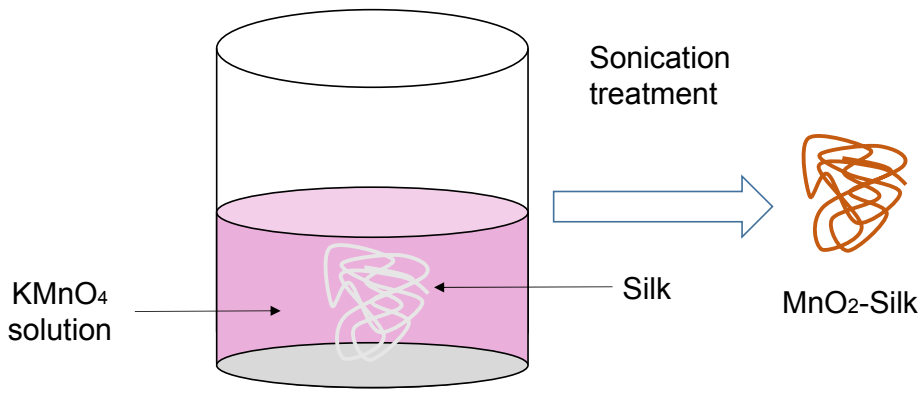

Figure 5.
Schematic showing the formation of MnO_2 NPs on silk fiber.

In-situ synthesis of MnO_2 NPs on silk film using sonication and auto-reduction (control)

To monitor and determine NPs formation and resulting activities, we designed optically transparent and structurally stable silk films as templates for MnO_2 NP formation [68, 69]. In **Paper 4**, we explained the process of preparation of aqueous regenerated silk fibroin from degummed silk. Then, we prepared a stable and transparent silk film from the regenerated silk fibroin stock solution.

Here, Figure 6 illustrates the steps to obtain a MnO_2-silk film using sonication. The auto-reduction samples (i.e., no sonication) were obtained with the same steps, with the sonication probe switched off. The first step (Figure 6) involved the methanol treatment of individual films. 2 ml of 30 % methanol was added to the quartz cuvette containing the silk-film and left to react for 10 min. Then a washing step was initiated in deionized water, to remove the excess organic solvent. After the washing, the film was dried for 2 min in the film holder. The

curvette was loaded with 2 mL of 0.5 mM $KMnO_4$ solution at optimum condition to the selected dilution. The sonicator probe was carefully inserted into the cuvette containing the $KMnO_4$ solution; the probe tip was at an optimal height to reduce the formation of bubbles entering the light path (Figure 6B). Two small magnetic stirrers were also added to the cuvette (not shown in illustration). Measurement of the UV spectra started when the dry methanol treated film was inserted into this cuvette (Figure 6). The stirring was set at 400 rpm, and the temperature maintained at 20°C. Once the reaction had terminated, the silk film was washed in double distilled water to remove any unbound $KMnO_4$. Henceforth, the reacted silk will be referred to as MnO_2-Silk film. Figure 6 depicts the silk film after methanol treatment and the MnO_2-Silk film after optimal MnO_2 formation treatment.

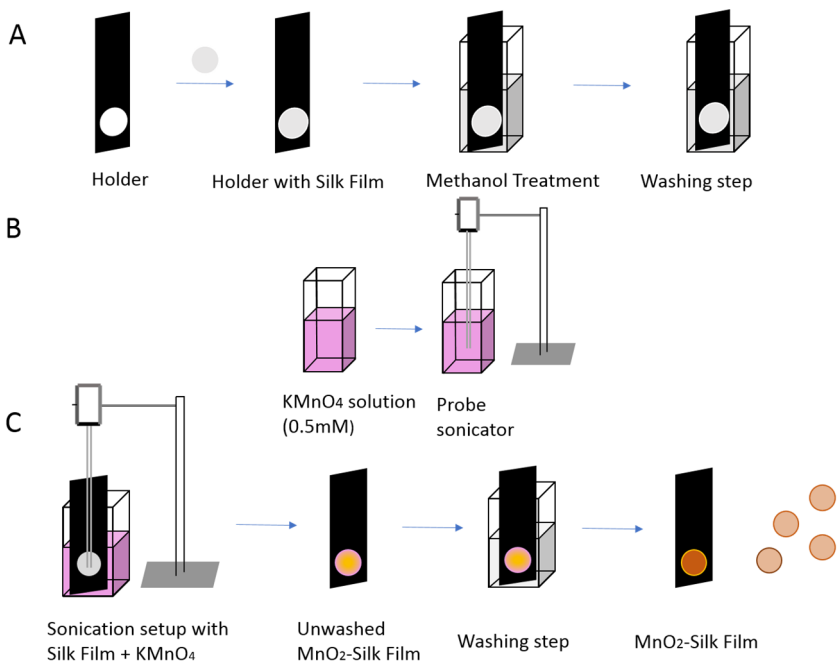

Figure 6.
Illustration of synthesis of MnO_2 NPs on silk film using sonication. Adapted from **Paper 4**.

Polypyrrole (PPy)-MnO_2 NPs silk fiber

Supercritical aided impregnation of pyrrole monomers followed by oxidative polymerization to polypyrrole at atmospheric conditions

The $scCO_2$ impregnation was performed in a modified SFE-100 system from Thar Technologies, Inc. (Pittsburg, PA). Note that we kept the temperature below 45˚C to limit any detrimental structural changes in the silk fibers. In the 20 mL glass vial, we added approximately 0.1 ± 0.02 g of silk and 10 mL of a solution containing different concentrations of the pyrrole monomer (5, 10, 25, and 50% (vol./vol.) dissolved in milliQ water. The impregnation was performed at three different CO_2 pressures of 50, 100, and 200 bar, using a CO_2 flow rate of 11 g/min. The time for impregnation was started when the desired pressure was reached. At the set pressure, the CO_2 flow was stopped, and the reactor was sealed. The fibers were impregnated for 20 min, after which the reactor pressure was slowly returned to atmospheric pressure using a bleeding valve. Before transferring the impregnated fibers to the oxidative polymerization vessel, the fibers were gently blotted with some tissue paper. In a 20 mL beaker, a 0.175 M $FeCl_3$ solution was prepared and pre-cooled to 4 °C in an ice-bath. The pyrrole-impregnated fibers were rapidly added to the beaker. The reaction was performed in the dark (closed beaker and under aluminum foil) under constant stirring at 100 rpm for 2 h. After the polymerization, the final fibers were thoroughly rinsed with water and air-dried overnight in a fume hood. The fibers were stored in a sealed container in the dark until further use.

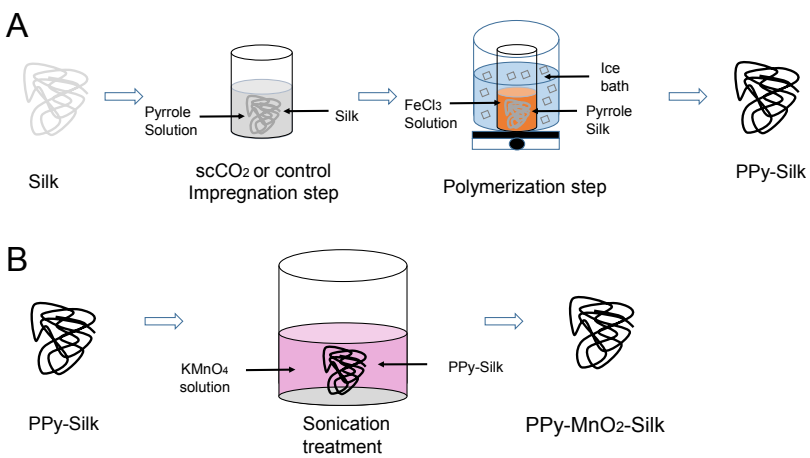

Figure 7.
Schematic diagram of the formation of (A) PPy-Silk and (B) PPy-MnO_2-silk using supercritical carbon dioxide ($scCO_2$) or atmospheric (control) aided impregnation of pyrrole monomers followed by oxidative polymerization to polypyrrole at atmospheric conditions.

Atmospheric impregnation of pyrrole monomers followed by oxidative polymerization to polypyrrole at atmospheric conditions

For the control, the impregnation of the pyrrole monomers was performed under atmospheric pressure (in the air) at room temperature, using the same steps as above. Approximately 0.1 ± 0.02 g of silk yarn was impregnated with different concentrations of the pyrrole monomer (5, 10, 25, and 50% vol./vol.) at atmospheric pressure, under magnetic stirring for 30 min, 2h, 6 h, 18 h, 24 h, 48h, and 96 h. We used the same procedure after impregnation for the oxidative polymerization.

MnO_2 NPs synthesis on PPy-silk fibers

The fabrication method for the synthesis of catalytic MnO_2 nano-particles on silk fibers was adapted, as shown in Figure 5. Briefly, in a 20 mL glass vial, approximately 0.1 g of PPy-silk fibers were mixed with 10 mL of a 20 mM $KMnO_4$ solution. Without delay, we irradiated the reaction mixture with ultrasonic waves for 45 min using a Bandelin Sonorex sonication bath at 35 kHz and 320 W. After sonication, the modified fibers were removed from the glass vial and washed thoroughly with deionized water and air-dried overnight at room temperature. The fibers were stored in a sealed container in the dark for further analysis. The supernatant was further characterized by UV absorbance to determine the fraction of $KMnO_4$ consumed using an absorption peak of $KMnO_4$ at 526 nm.

Characterization techniques

Here, we describe the different characterization techniques used to characterize the nanomaterial-based silk composite hybrid material. Primarily, the powder x-ray diffraction (PXRD), henceforth XRD, FTIR-ATR, UV-visible absorption spectroscopy, SEM, small-angle x-ray scattering (SAXS), anomalous small-angle x-ray scattering (ASAXS) and near-edge x-ray absorption fine structure (NEXAFS) techniques were used.

X-ray powder diffraction (XRD)

XRD can be used for the qualitative and quantitative identifications of solid phases. This technique can analyze diffraction from micro-crystalline and amorphous powder. The powder diffraction pattern can only provide one-dimensional data due to the rotational projection of the randomly oriented reciprocal lattices.

The XRD method involves the interaction between the incident monochromatized x-rays (Cu Kα1 radiations) with the atoms of a periodic lattice family of planes (identified by a system of Miller Indices, hkl) in the polycrystalline material. The

X-rays were scattered by atoms in an ordered lattice interference, constructively following the directions given by Bragg's law:

$$n\lambda = 2d\sin\theta \quad (1)$$

Where, n is an integer standing as the order of reflection, λ is the wavelength of the x-rays, d is the distance between two lattice planes and θ is the angle between the incoming x-rays and the normal to the reflecting lattice plane. The identification of the solid phase is based on the comparison of the set of reflections of the sample to that of pure reference phases, distributed by the International Center for Diffraction Data (JCPDS-ICDD).

The XRD pattern was collected in transmission mode on a Stoe Stadi MP instrument using Cu Kα1 radiation. The instrument was enabled with a curved germanium monochromator and an MYTHEN detector. The samples were scanned in the range $2\theta = 10–90^{o}$, with an accumulation time of 20 min. Each silk was bundled and mounted between two transparent Mylar disks.

Fourier transform infrared attenuated total reflectance (FTIR-ATR)

The FTIR-ATR spectra of silk fibers or modified silk fibers were measured with an iD5 ATR accessory with diamond crystal (Thermo Scientific). Each spectrum was background corrected and collected between 550-4000 cm^{-1}. Each spectrum was an average of 32 scans at 4 cm^{-1} resolution. The FTIR-ATR spectra were further processed to extract four structural parameters, namely: the crystallinity degree, the tyrosine ratio, the amide I/II ratio, and the hydrogen bond index. The crystallinity degree of silk fibers was calculated by comparing the peaks' intensities at 1263 and 1230 cm^{-1} as follows:

$$Crystallinity\ degree\ (\%) = \frac{A_{1263}}{A_{1230}+A_{1263}} * 100 \quad (2)$$

Where A_{1263} and A_{1230} are the intensities of the peaks at 1263 and 1230 cm^{-1}, respectively.

The tyrosine ratio was calculated by estimating the area under the tyrosine peaks at ± 830 and ± 850 cm^{-1} and computing the ratio of intensities at 850 / 830 cm^{-1}. The weak features at ± 850 and ± 830 cm^{-1} make a doublet attributed to Fermi resonance of the aromatic side chain of the tyrosine residue. The ratio is indicative of the local environment of tyrosine residues within the fibers and, by extension, the local environment of the amorphous regions of the silks.

Furthermore, the ratio of the maximum intensities of amide I (at around 1640 cm^{-1}) and II (at around 1540 cm^{-1}) peaks were also calculated to estimate the total change in secondary structure upon treatment. Moreover, the amide I region (1600–1700 cm^{-1}) was deconvoluted to extract the secondary structure composition of the silks.

Data analysis for UV-Visible spectroscopy

The spectra (single or kinetic series) collected were processed and visualized with Spectragryph software [70] and Matlab (The Mathworks Inc.). To determine the percentage of $KMnO_4$ consumed, we used the $KMnO_4$ absorbance intensity at 525 nm. To correct for scattering contribution from the particles, the peak at 525 nm was baseline corrected. To identify the peaks that were changing during the kinetics, we calculated the second derivative (spectral feature enhancement) and computed the 2D correlation spectra - 2D-COS [71]. The three results from the 2D-COS are a power spectrum, synchronous correlation, and asynchronous correlation. The power spectrum or auto-correlation shows the peaks that are changing (appearing or disappearing) from the kinetics series. The synchronous correlation shows the peaks' changes that are correlated with one another. The asynchronous correlation informs on the sequence order of peaks' changes (e.g., peak 1 and 2 are correlated, and peak 1 changes before peak 2). The analysis of the kinetic traces was performed using XPfit eXPonential Fitting Software (SoftScientific a division of Alango).

Conductivity measurement using four-probe set up

The conductivity of the dry PPy-silk fibers was measured using the four-probe method with a Fluke 45 multimeter and a PS3003 DC power supply (HQ power supplies). The set up consisted of two silver-plated electrodes onto which the fibers were glued with conductive silver glue. In between the silver-plated electrode and separated by a distance of 1.5 cm, two miniature copper clamps were used to measure the voltage drop across the modified silk threads when a 2 A current was applied. For each sample, three different silk yarns were selected randomly for the conductivity measurement. The measured conductivity was normalized to the mass gain of PPy and expressed in $S.m^{-1}.mg^{-1}$.

Potentiometric acid-base titration

All titrations were performed in a glass vessel with the lid, as part of a Mettler-Toledo DL50 Graphix titrator unit interfaced by LabX v3.1 software to a personal computer. All solutions used in this experiment were carefully prepared to be O_2, and CO_2 degassed, and of analytically known concentrations. All titrations were carried out in a constant-temperature/pressure variable volume air-tight reactor to eliminate the transfer of volatiles (e.g., CO_2) during the titration.

Two separate buret exchange units with 20-mL burets were used, one for acid and one for base. The temperature was kept constant at 22°C. The electrode was two-point calibrated, provided with a fresh buffer before each experiment (pH 4, 7). The DL50 unit was programmed with an "end-point equivalence point titration" method, which adds the same volume of titrant at each step. The method is as follows: After an initial pause of 3 sec, 150 µL of titrant was added; when the signal drift reached 0.01 mV/min, another 150 µL of titrant was added, and this process was repeated until the titration was halted when the pH reached 2 or 12.

For all samples, two methods were applied: (i) direct titration by acid or base, (ii) overnight acid equilibration using HCl (to a pH ≈ 2), followed by a base titration. Although tested, the overnight alkaline equilibration using NaOH was not considered, simply because NaOH hydrolyzes the silk fibers. The ionic strength was set at 0.5 M (using NaCl), both for titrant and titrand (analyte). Table 2 summarizes the samples and conditions used.

Table 2. Titration samples. Adapted from Paper 3,

Sample ID	Titration type [a]	Titrant	Samples
Native silk	Acid	0.1 M HCl + 0.5 M NaCl	40 ml 0.5 M NaCl + 200 mg Silk
	Base	0.1 M NaOH + 0.5 M NaCl	200 mg Silk + 40 ml 0.5M NaCl + 0.1 ml of 5 M HCl
Free MnO_2 particles	Acid	0.1 M HCl + 0.5 M NaCl	40 ml 0.5 M NaCl + 200 mg free MnO_2 particles
	Base	0.1 M NaOH + 0.5 M NaCl	200 mg free MnO_2 particles+ 40 ml 0.5 M + 0.1 ml of 5 M HCl
MnO_2-Silk hybrid fibers	Acid	0.1 M HCl + 0.5 M NaCl	40 ml 0.5 M NaCl + 200 mg MnO_2-Silk
	Base	0.1 M NaOH + 0.5 M NaCl	40 ml 0.5 M NaCl + 200 mg MnO_2-Silk + 0.1 ml of 5 M HCl
Supernatants		0.1 M NaOH + O.5 M NaCl	Supernatants of acid equilibrated samples

[a] For base titration the fibers were equilibrated in 40 mL of 0.5 M NaCl + 0.1 mL of 5M HCl. After the overnight acidification, the fibers were rinsed thoroughly in milliQ water, blotted and then added to a freshly prepared 40 mL solution of 0.5 M of NaCl + 0.1 ml of 5 M HCl, and immediately titrated with a base

The different titration data were analyzed using the linear programming method (LPM) proposed by Brassard et al. [72]. All data analysis was performed using a custom script in Matlab (The MathWorks Inc.). Measured pH values were converted to [H+] using the Davies equation [73] for ionic force larger than 0.2 M, resulting in the effective concentration (ion activity).

The linear programming method assumes that a heterogeneous mixture of binding sites can be treated as a sum of n monoprotic sites [72, 74]. For the j^{th} addition of acid or base, the charge balance expression can be written [72]:

$$C_{bj} - C_{aj} + [H^+]_j - [OH^-]_j = \sum_{i=1}^{n} \left(\frac{L_{Ti} K_i}{K_i + [H^+]_j} \right) - ANC \quad (3)$$

Where C_{bj} and C_{aj} correspond to concentrations of base and acid for the j^{th} addition of titrant, and ANC corresponds to the initial acid-neutralizing capacity of the system. For the i^{th} site, the acidity constant is K_i, and the ligand concentration is LT_i. In this model, the terms on the left can be estimated using experimental data, and the terms on the right are the fitting parameters. The problem is then treated as a set of n multiple linear equations, one for each titration step j [72, 74]. Each equation is linear because it is assumed that the titration profile of the ligands arises from the sum of n monoprotic sites, with constants ranging from K_i to K_n.

Contrary to the standard FITEQL [75] and Protofit [76] methods that solve equation 1 by setting the number of sites (n) and varying both LT_i and K_i. Brassard et al. showed that to prevent any convergence problems caused by the correlation of LT_i and K_i, it is preferable to fix the pK values as a grid from a minimum to a maximum value at fixed step sizes. The ligand concentration associated with each pK value is assigned a positive value where zero is a possible result; the result is the so-called pK spectrum. Consequently, an adequate number of sites correspond to the number of non-zero pK values. The minimum and maximum pK correspond respectively to the minimum and maximum measured pH. For the experiments here, the pK grid was defined from 2 to 12 in steps of 0.2. Note that a more reliable range is 4 to 10. Outside this range, errors for acid-base titrations are substantial. There may be sites outside this range, but they are difficult to observe using a glass electrode.

Component analysis

Single wavelength analysis of kinetics, although convenient, can be misleading. Here we analyze the whole UV-visible absorption curves to extract the individual components of the UV-visible spectra and their concentration profiles. The starting step is the determination of the number of independent components. Consider *N* UV-visible spectra collected at different times. The data can be arranged in a matrix *A*, where the rows correspond to different wavelengths (λ), and the columns are the spectra at time t. Applying a singular value decomposition to the data matrix deconvolves the signal into a set of orthogonal basis functions, as follows [77]:

$$A = UWV^T \qquad (4)$$

For the case of *M* different wavelengths, A is an M x N matrix. The matrix U is also an M x N. W is a N x N diagonal matrix containing the singular values wi on the main diagonal. The singular values are ordered in descending order. According to Henry and Hofrichter [77] the number of correct, independent basis functions $U_i(\lambda)$ correspond to the number of distinctly absorbing species. They further suggested the following three criteria to determine the number of signal-containing components: (1) Inspection of the basis functions—by plotting the basis functions Ui(λ) as a function of q, one can estimate which of the Ui(λ) contain appreciable levels of signal and which correspond to noise. (2) Singular values—the size of the singular values gives an estimate of the relative importance of the corresponding basis components. (3) Autocorrelations of the basis functions—by computing the left and right singular vectors autocorrelations

$$C_i^U = \sum_{j=1}^{M-1} U_i(\lambda_j) U_i\,(\lambda_{j+1}) \qquad (5)$$

$$C_i^V = \sum_{j=1}^{M-1} V_i(\lambda_j) V_i\,(\lambda_{j+1}) \qquad (6)$$

of each of the basis functions, an estimate of the "noisiness" is obtained. Components which contain detectable signal typically have autocorrelations close to 1.0 (>0.95), whereas components that correspond to noise tend to have C_i < 0.8.

Following the identification of the number of components, we use a multi-curve resolution weighted alternating least square method (MCR-WALS) to fit the kinetics[78]. A critical step in the use of the MCR-WALS is the initial guesses for the components spectra and concentration profiles. Here given the fact the components spectral features are highly overlapped with an increasing baseline due to particle formation, we need to have a robust guess procedure. We, therefore, used a modified version of the original simplisma algorithm [79]. In the modified version [80] both the conventional spectra (for pure variables of broad peaks) and second-derivative spectra (for pure variables of narrow peaks, overlapping with the broad peaks) are used to resolve spectra with wide and narrow peaks, minimizing baseline problems by resolving them as separate components. All the analysis was performed using custom scripts in Matlab.

SAXS

The scattering experiments were performed with the SAXS setup of Helmholtz Zentrum Berlin [81] at the four-crystal monochromator beamline of PTB [82] at the synchrotron radiation facility BESSY II (Helmholtz-Zentrum Berlin, Germany) with a photon energy of E = (8000.0 ± 0.8) eV. The density gradient capillary was moved in steps of 0.5 mm along the central vertical axis of the capillary, where a scattering pattern was collected for 45 to 100 sec. At these positions, the solution transmittances were previously measured at an energy of E = (5500.0 ± 0.6) eV in order to calibrate the suspending medium electron density [83]. Scattering curves with different contrasts were measured at three different diffusion times, adding to a total of ca. 40 curves. The X-ray photons were collected at a distance L = (4539 ± 1) mm with a vacuum-compatible Pilatus 1M hybrid-pixel detector (Dectris Ltd, Baden, Switzerland) with a pixel size of d = (172.1 ± 0.2) μm [84].

The rotationally symmetric scattering patterns were circularly integrated and converted to momentum transfer q using the expression:

$$q = \frac{4\pi E}{hc} \sin\left(\frac{1}{2}\arctan\left(\frac{R}{L}\right)\right) \qquad (7)$$

where h is the Planck constant, c is the speed of light, and R is the distance to the beam center. The obtained scattering curves were normalized to the exposure time, the measured suspension transmittance, and the incident photon flux, measured by means of a calibrated transparent silicon diode [85]. Also, the scattering background of pure water was subtracted.

ASAXS data analysis

The scattering equation involves the atomic scattering term $|f(q,E)|^2$, which shows negligible energy-dependence far from an absorption edge, but near an edge, the dispersion and absorption terms become significant. For a material comprising two kinds of scattering objects, one consisting of the resonant element and the other not, the scattering pattern from the former can be isolated from the resonant component. Using the notation of Ballauf *et al*. [86], and reproduced from [87], the scattering intensity is:

$$I_s(q,E) = F_0(q)^2 + 2F_0(q)\nu(q)f'(E) + \nu(q)^2\left[f'^{(E)^2} + f''(E)^2\right] \qquad (8)$$

Where $F_0(q)$ is the non-resonant scattering amplitude (i.e.total scattering from non-resonant objects, plus non-resonant scattering from the resonant objects), $\nu(q)$ is the scattering amplitude from the resonant objects, and f´(E) and f´´(E) are the atomic dispersion and absorption terms [86], tabulated by Henke *et al*. [88]. This expression is general and applies to both hard and soft X-ray resonance effects.

The first term, $F_0(q)^2$, is the non-resonant scattering intensity. The difference in intensity between measurements performed at two energies comprises the last term, $\nu(q)^2[f'(E)^2 + f''(E)^2]$, which is purely resonant scattering, and the central term, $2F_0(q)\nu(q)f'(E)$, which is mixed. The mixed term can be isolated by measuring the scattering intensity at least at one additional energy below the absorption edge, and knowing or measuring f´(E) and f´´(E). These can be obtained experimentally from X-ray absorption spectroscopy measurements, since f´´(E) is the absorption, and applying a Kramers–Kronig transformation to obtain f´(E) [89]. However, in practice, it is not always possible to perform these measurements. In cases where the scattering feature involving the target species is located in a q-range sufficiently far removed from other non-resonant scattering features, qualitative information about the resonant scattering feature (position and shape, but not absolute intensity) can be obtained by only taking the difference pattern between two measurements performed at different energies below the absorption edge [90]. This has been demonstrated for systems such as small metal NPs attached to support materials having a much larger particle or pore size [90-93] and biological support materials [94, 95].

Cyclic voltammetry

Cyclic voltammetry was performed by using a PalmSens potentiostat (Model Emstat2, Palm Instruments BV, Utrecht, The Netherlands) controlled with the PSTrace software, version 4.5. A three-electrode electrochemical cell was used with an Ag|AgCl (saturated KCl) as a reference electrode, a platinum wire as a counter electrode, and the PPy- MnO_2-Silk as the working electrode. 5 mM, H_2O_2 was used as a substrate. All measurements were performed at room temperature in 50 mM phosphate buffer saline (PBS) at pH 7.4.

Application

Methylene blue degradation

To confirm the oxidative properties of the MnO_2 NPs, we used the MB dye. The MB degradation test was performed by placing 0.1 g of the MnO_2-Silk fiber or PPy-MnO_2-Silk fiber in contact with 50 ml of the dye solution at 1 mg/l in water, and under vigorous stirring. The solution was circulated in a quartz flow cell in a UV-visible absorption spectrophotometer (Biowave II spectrometer) and returned to the reaction beaker. The recirculation assay was run for 15–45 sec. The color removal was monitored by the decrease of the dye's main absorption peak at 665 nm. The rate of degradation was estimated from the decrease of the initial slope of the main peak as a function time.

H_2O_2 degradation

The degradation of H_2O_2 was performed by placing 20 mg of the PPy- MnO_2-Silk fiber hybrid in contact with 25 mL of a 25 mM H_2O_2 solution prepared in a 50 mM sodium phosphate buffer at pH = 7.4 and under stirring. The degradation reaction was monitored for 25 min (a data point every 5 min) as the oxidation current produced at a Pt electrode with a constant applied potential of + 0.7 V for 20 s (Sire P200 series, Lund, Sweden). Importantly, the oxidation of H_2O_2 at the platinum electrode contributed to the disappearance of H_2O_2, we measured and calculated the contribution from the SIRE to the disappearance of H_2O_2 to be less than 7 % (within the experimental error). The rate of catalytic degradation of H_2O_2 was estimated by considering the initial slope of the decrease in current as a function of time.

TMB and OPD degradation

To quantify the peroxidase and oxidase-like activities, we used chromogenic substrates such as TMB and OPD. When TMB oxidizes, its colors change from colorless to blue, and when OPD oxidizes, its color changes from colorless to orange. These activities were monitored kinetically at specific wavelengths: 652 nm for TMB and 450 nm for OPD using a UV-visible absorption spectrophotometer (Biowave II spectrometer).

TMB stock solution of 4.16 mM in DMSO was prepared and stored in the fridge, before every activity assay. The assay was prepared by diluting the TMB stock to obtain the final concentrations (0.12, 0.22, 0.32, 0.42, and 0.52 mM) with phosphate citrate buffer 50 mM at pH 5, 7.4 and 9.

Furthermore, the assay for OPD was prepared by diluting the OPD with phosphate citrate buffer 0.05 M to obtain the final concentration (3.7, 5.7, 7.7, 9.7, and 11.7 mM) at pH 5, 7.4, and 9.

To ensure that we measured the MnO_2 attached to the silk fibers, and not some residuals leaching into solution; we devised the following method (figure 8).

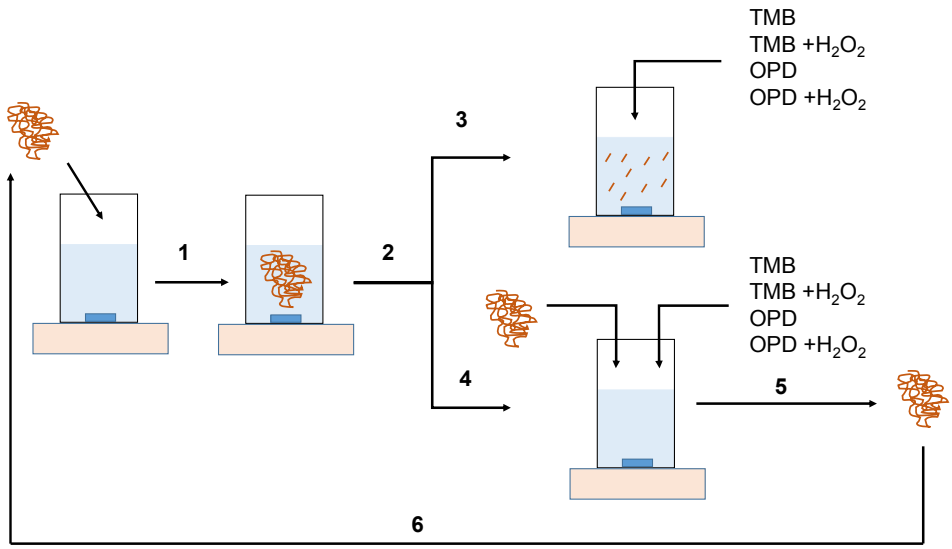

Figure 8.
Method for the MnO_2-Silk catalytic activity. For each MnO_2-Silk, step (1) consisted of adding the fibers the activity buffer without TMB and OPD and vigorously stir for 4 minutes (i.e., the assay time). In step (2), the fibers were recovered, and the supernatant immediately tested for activity in step (3) by adding TMB or OPD. The fibers were rinsed in double distilled water and gently blotted and tested for activity in step (4) in a fresh buffer. In step (5), the fibers were recovered, rinsed in double-distilled water, and gently blotted using tissue paper. For the re-usability (step 6), we returned to the start of the process and step (1). Adapted from **Paper 3**.

For each MnO_2-Silk, step (1) consisted of adding the fibers the activity buffer without TMB and OPD and vigorously stir for 4 minutes (i.e., the assay time). In step (2), the fibers were recovered, and the supernatant immediately tested for activity in step (3) by adding TMB or OPD. The fibers were rinsed in double distilled water and gently blotted (using tissue paper), and tested for activity in step (4) in a fresh buffer. In step (5), the fibers were recovered, rinsed in double-distilled water, and gently blotted using tissue paper. For the re-usability (step 6), we returned to the start of the process and step (1).

The OPD and TMB oxidation was performed by placing 5 mg of MnO_2-Silk fiber in a 10 mm path length quartz cuvette with 3 ml of the TMB solution (0.12, 0.22, 0.32, 0.42, and 0.52 mM) or 3 mL of the OPD (3.7, 5.7, 7.7, 9.7, and 11.7 mM) solution, in the presence/absence of H_2O_2 (3.3 mM) under vigorous stirring. Each reaction was performed for 4 min. The catalytic activity was calculated as a measure of the initial rate of the curve change for TMB at 652 nm and OPD at 450 nm.

Chapter 2. The problem of nanofillers leakage and stabilization in fibers and textiles for smart applications

Substances such as CO_2, water and *n*-hexane behave as supercritical fluids (SCF) above their critical temperatures and critical pressures [96]. SCFs have already found their applications in many areas such as extraction, dyeing, impregnation, polymerization, fractionation, degumming/cleaning, in the formation of metal or metal oxide nanoparticles (NPs) and in polymers synthesis and modification, to name a few [97-111]. Among the SCFs, CO_2 has attracted more interest due to its low cost and toxicity, non-flammability and easily attainable critical temperature and pressure [108, 110, 112-114].

Impregnation is the process of adding a substance onto or in a polymer matrix to improve the property of the material. The primary purpose of impregnation of NPs in textile fibers is to increase the mechanical strength, improve physical properties—such as electrical conductivity, antistatic behavior—and add functionalities—such as anti-microbial, catalytic properties, UV protection, flame retardance and self-cleaning [19, 97, 115, 116].

There are several ways to impregnate or synthesize NPs onto or in fibers. A now-standard method includes plasma treatment, *in situ* synthesis, sol-gel synthesis, chemical assembly, depositions, dip coating and sonochemical reduction [19, 20, 22, 23, 25, 26]. The above conventional aqueous or solvent-based coating/impregnation methods have drawbacks, such as a decrease in the tensile strength of the fibers, low diffusion rates, high temperature, limited penetration depth, very long contact time, consumption of high energy, water, solvents, the process demands harsh chemical pre-treatment, hazardous solvents and leakage of NPs from the fiber after multiple washes [28, 29]. The harsh chemical pretreatment step and leakage of NPs from fibers and textiles may lead to serious environmental and health issues [28, 29, 117].

Within this context, the use of sc-CO_2 is an attractive alternative [112, 118-121]. The synthesis/impregnation of NPs on a polymeric substrate under scCO_2 has several advantages, due to some of its unique properties: low toxicity, non-flammable, inexpensive, low surface tension and no-toxic residue in the treated medium after removal [112, 118-121]. Typically, the exposure of natural and synthetic polymers to scCO_2 results in swelling and enhanced chain mobility of

the polymers helps to load the additives [104, 122, 123]. Recent examples and applications using $scCO_2$ with dyes, conductive monomers, inorganic metal/metal oxide NPs in various inorganic and organic substrates have demonstrated the usefulness of the method [97, 99, 104, 105, 109, 110, 121, 124]. Silk, on the other hand, has had a limited application with $scCO_2$, mainly within silk fibers dyeing [104, 125], grafting [67, 126] and controlled drug delivery application [43]. To the best of our knowledge, there is no report yet of metal/metal-oxide NPs impregnation in silk fibers using $scCO_2$.

Among the functional metal NPs, Au NPs have attracted much attention from researchers because of its promising optical, electronic, magnetic, catalytic and biomedical applications [13, 24, 127]. Due to the synergistic effect gained from the physical or chemical interactions between the organic (silk) and inorganic (Au NPs) components, functionalization of silk materials with Au NPs can be utilized for different applications, such as wearable sensor [127], ultraviolet (UV)-blocking ability and antibacterial activity [128]. Further, Au NPs silk-based hybrid showed enhanced Raman signals for use as an active SERS substrate for the detection of trace analytes [129]. More and more articles have disclosed new approaches for the preparation of NPs based silk hybrids (such as, Au NP [24], Ag NP [25], TiO_2 and Ag NPs [22]) with significant antibacterial activity and UV protection capacities. However, the typical methods used, namely dip coating and wet chemistry, do not prevent or reduce the wash fastness of the hybrid textiles. Consequently, large amounts of potentially toxic compounds are leaked into the environment. The limiting factor is the undefined available space in textiles fibers for functionalization with NPs. Moreover, literature concerning supercritical NP impregnation of textiles, or even polymer, does not have any insights on the available space for loading NPs.

In this chapter, with a green and straightforward approach, using $scCO_2$ as a carrier fluid, we explored the impregnation in four types of Indian textile silks (mulberry, eri, muga, and tasar), with five standard sizes of Au NPs (5, 20, 50, 100 and 150 nm). Furthermore, we discuss the effects of $scCO_2$ NPs impregnation on silk structure, an estimate of loading capacity in different varieties of silk with different gold sizes and the mechanism of impregnation of NPs in/on silk fiber

Fiber post-processing

The evaluation of the robustness of the impregnation process was tested by successive water washes and evaluation of the wash supernatant by UV absorption. The three different stages in the wash process were: (i) directly after impregnation—Au loading, (ii) after fiber gentle washing—wash leakage and (iii) after a harsher wash at 50^{o}C for 1 h—fastness leakage (Figure 8). The liquid supernatants were measured by UV absorbance, and we calculated the Au loading, wash leakage, fastness leakage and total efficiency as follows:

$$Gold\ loading\ (\%) = \left(1 - \frac{A_1}{A_0}\right) * 100 \quad (9)$$

$$Wash\ leakage\ (\%) = \frac{A_2}{A_0 - A_1} * 100 \quad (10)$$

$$Fast\ leakage\ (\%) = \frac{A_3}{(A_0 - (A_1 + A_2))} * 100 \quad (11)$$

$$Total\ efficiency\ (\%) = \frac{A_0 - (A_1 + A_2 + A_3)}{A_0} * 100 \quad (12)$$

Where, A_0 is the absorbance of Au suspension before impregnation, while A_1, A_2, and A_3 are the absorbance of the liquid supernatant after impregnation, water wash and fastness treatment, respectively. The total efficiency of Au nano-particles in silk fibers is calculated as the cumulative loss of Au through the three wash steps.

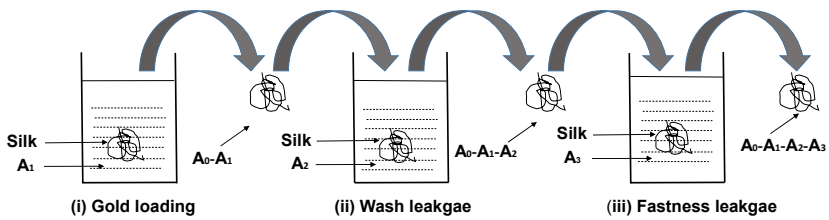

Figure 9.
Three different stages in the wash process. Where, A_0 is the absorbance of Au suspension before impregnation, while A_1, A_2, and A_3 are the absorbance of liquid supernatant after impregnation, water wash, and fastness treatment.

Characterization

The evaluation of the impact of the impregnation procedure was conducted using XRD and FTIR-ATR

XRD

XRD confirmed the presence of the Au NPs with an increasing diffraction peak at 38˚. Note that the silks diffraction peaks were conserved regardless of the Au NPs size used. No further attempt at analyzing the XRD was deemed necessary.

FTIR

Effect of $scCO_2$ impregnation on silk structure

Figure 10 shows the effects of Au NPs size on a global structural parameter: amide I/II ratio. Changes in the amide I/II ratio indicates that a structural change has occurred. For mulberry and muga silk fibers, we observed no differences between the $scCO_2$ treatment and control at different Au NPs sizes. Interestingly, both traces overlapped with the amide I/II ratio of their native silk (horizontal line in the figure 10).

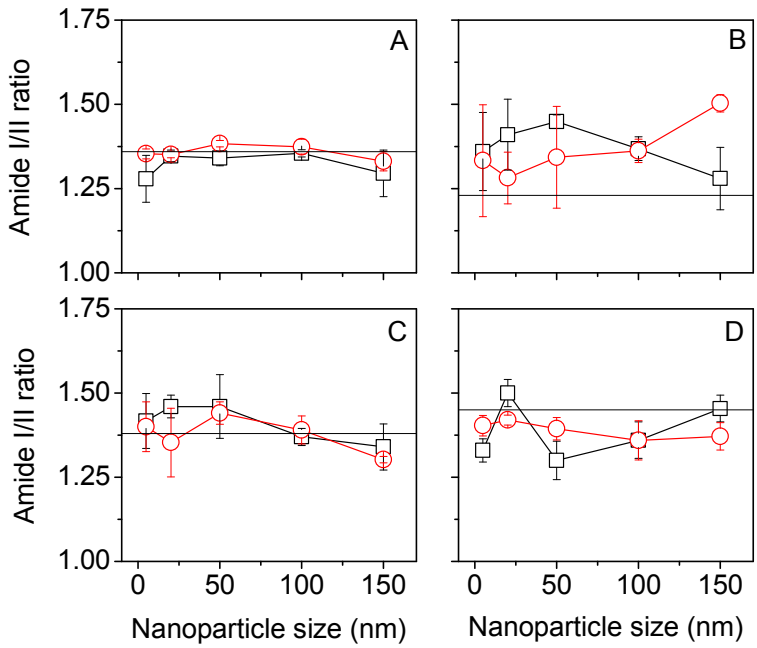

Figure 10.
FTIR-ATR change in amide I/ II ratio for Mulberry (A), Eri (B), Muga (C), and Tasar (D) silks. Black squares (□) are $scCO_2$ samples, red circles (O) are control samples. The horizontal line in the amide I/II ratio is native silk. We found that for $scCO_2$ treatment alone, the amide I/II ratio was not significantly different from the native silks. Adapted from **Paper 1.**

Tasar silk presented a similar trend to mulberry and muga, except that the amide I/II ratio was consistently lower compared to the native tasar. For eri silk, on the other hand, the amide I/II ratio showed differences between treatments and departed from the native eri silk amide I/II ratio.

The detail of the changes in the amide I/II ratio can be resolved by fitting the amide I peak with a sum of Gaussian contribution. The position and relative area of the Gaussian peaks were then interpreted in terms of secondary structure content and fraction. Figure 11 illustrates the results of such an analysis. Four

secondary structures were extracted for the four silks, namely a peak centered at around 1620 cm^{-1} representing intermolecular β-sheets, a peak centered at 1655 cm^{-1} representing a mixture of random coil and α-helices, a peak centered at about 1678 cm^{-1} representing β-turns and a weak peak centered at around 1695 cm^{-1} representing β-sheets structures (Table 3).

Table 3. Consensus assignment for silk secondary structure determination by FTIR. Reproduced from [130]

Wavenumber range (cm^{-1})	Assignment
1605-1615	(Tyr) side chains/aggregated strands
1616-1621	aggregate beta-strand/ beta-sheets (weak)[a]
1622-1627	beta-sheets (strong)[a]
1628-1637	beta-sheets (strong)[b]
1638-1646	random coils/extended chains
1647-1655	random coils
1656-1662	alpha-helices
1663-1670	turns
1671-1685	turns
1686-1696	turns
1697-1703	beta-sheets (weak)[a]

[a] Intermolecular beta-sheets
[b] Intramolecular beta-sheets

In all silks, the β-sheets content appeared constant, regardless of the impregnated Au FNP. In only mulberry, we found an inter-conversion from the random coil/α-helical structures to β-turns, with increasing Au NP sizes. Noteworthy, the overlapping signal from water in the amide I region that may bias the decomposition of secondary structures. For example, $scCO_2$ drying followed by washing and high-temperature treatment may affect the water signal contribution in the amide I differently.

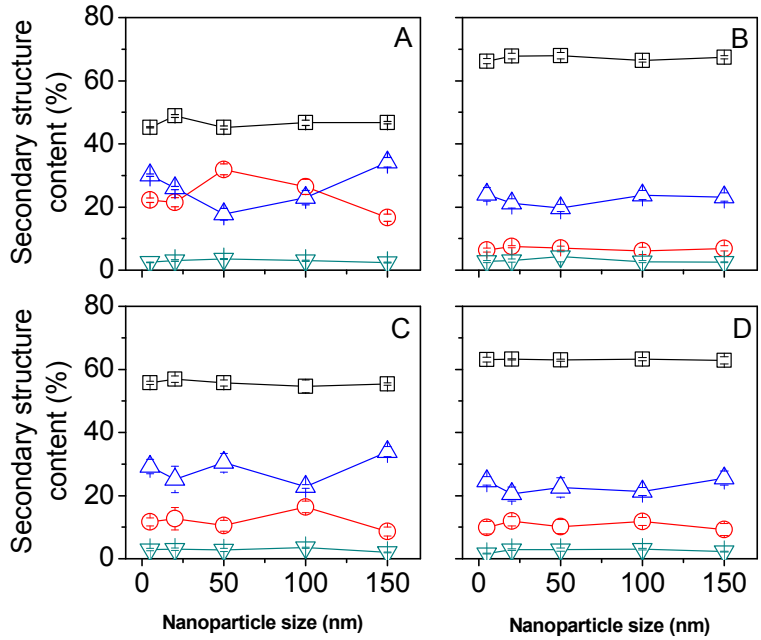

Figure 11.
FTIR-ATR changes in secondary structure content as a function of Au NP size for Mulberry (A), Eri (B), Muga (C), and Tasar (D) silks. Black squares (□) are inter β-sheets, red circles (O) are β-turns, blue triangles (Δ) are α-helices and random coils, inverted green triangles (∇) are intra β-sheets. Adapted from **Paper 1.**

In Figure 12, we compared the tyrosine ratio. The relative intensities of the tyrosine doublet (intensity at 850 cm^{-1}/intensity at 830 cm^{-1}) were used as spectral markers of the environment of the hydroxyl groups and the strength of hydrogen bonds involving these groups. The tyrosine residues usually exist in the amorphous regions, which contain most of the amino acids with bulky and polar side chains. An increase in the tyrosine ratio led to the conclusion that the hydrogen bonds involving the tyrosine residues were weak, and consequently, the mobility of the tyrosine residues was higher.

We found that for mulberry, muga and tasar, the tyrosine ratio was constant and close to the value of the respective native silks. On the other hand, eri silk showed a constant tyrosine ratio with increasing Au NP size but a systematically lower ratio, when compared to native eri silk, suggesting the amorphous region being stiffer after the treatment.

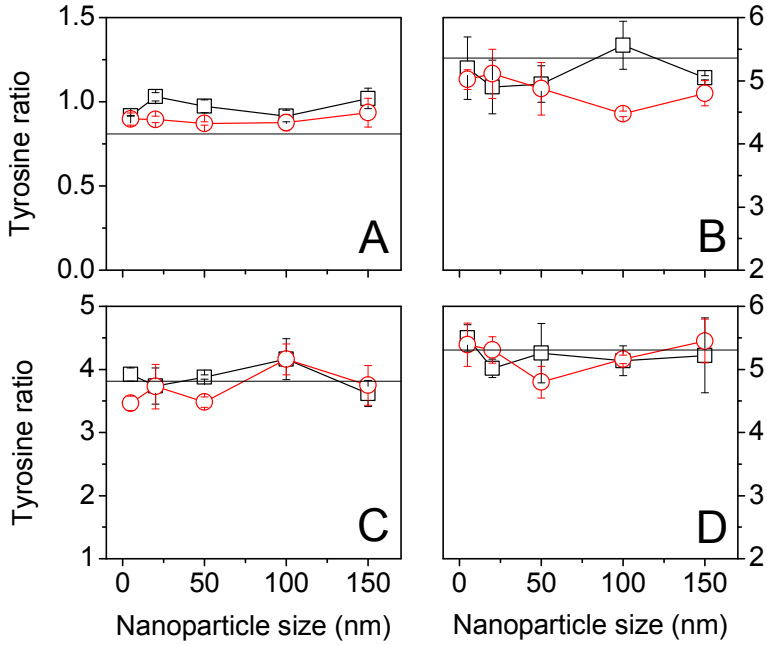

Figure 12.
FTIR-ATR changes in tyrosine ratio for Mulberry (A), Eri (B), Muga (C), and Tasar (D) silks. Black squares (□) are $scCO_2$ samples, red circles (O) are control samples. The horizontal line is the tyrosine ratio in native silk. We found that for $scCO_2$ treatment alone, the tyrosine ratio was not significantly different from the native silks. Adapted from **Paper 1.**

In the figure 13, as expected from the secondary structure decomposition with constant β-sheet content, we observed a constant crystallinity for all the silks with increasing Au NP size. Importantly, the crystallinity did not vary substantially from the native silks', except for Eri, where we found a systematically higher value.

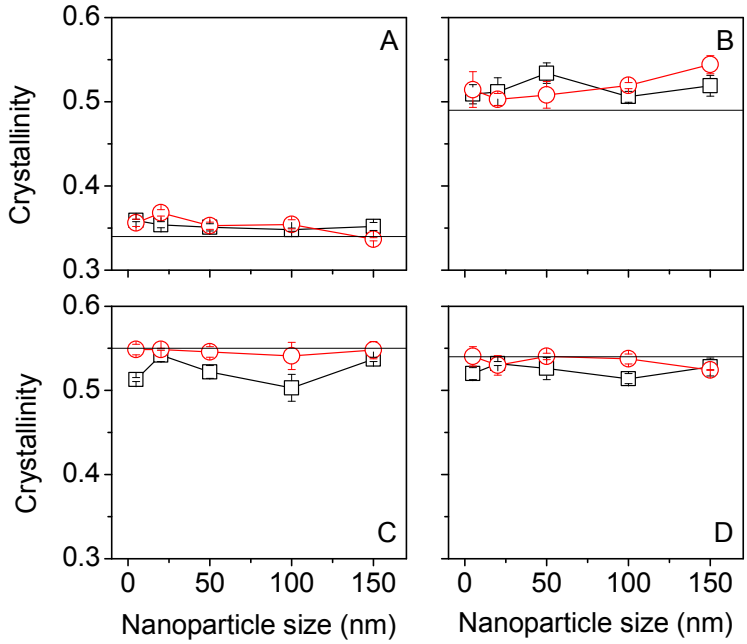

Figure 13.
FTIR-ATR change in crystallinity for Mulberry (A), Eri (B), Muga (C), and Tasar (D) silks. Black squares (□) are $scCO_2$ samples, red circles (O) are control samples. The horizontal line is the crystallinity in native silk. We found that for $scCO_2$ treatment alone, the crystallinity was not significantly different from the native silks. Adapted from **Paper 1.**

Gold (Au) loading capacity and color change in different silks with different Au sizes

Figure 14 shows the color changes in the silks due to the Au plasmonic effect. Note that the color changes for muga and tasar silks were not as evident as in mulberry and eri, since the former ones were already colored.

The total efficiency of Au loading was above 90% for the $scCO_2$ treated mulberry silk fiber, with Au NPs sizes of 5, 20, 50, 100 nm except for 150 nm, where the efficiency dropped to 75.9 ± 3.4%. In the controls, at atmospheric pressure, the total efficiency was constant from 5 to 100 nm at 24.0 ± 6.2%, dropping to approximately 12% for the 150 nm particle sizes.

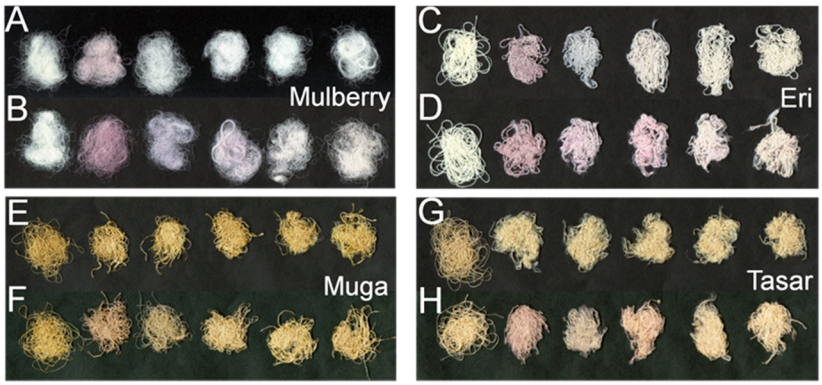

Figure 14.
Photographs of the various silks after Au NPs impregnation. Mulberry: $scCO_2$ (A), control (B); Eri: $scCO_2$ (C), control (D); Muga: $scCO_2$ (E), control (F); and Tasar: $scCO_2$ (G), control (H). In all photographs, the first fiber bundle from the left was the native untreated silk, then the fibers treated with five different sizes Au NPs (5, 20, 50, 100, and 150 nm), respectively. The color changes correlate with the initial Au solutions' colors. Adapted from **Paper 1.**

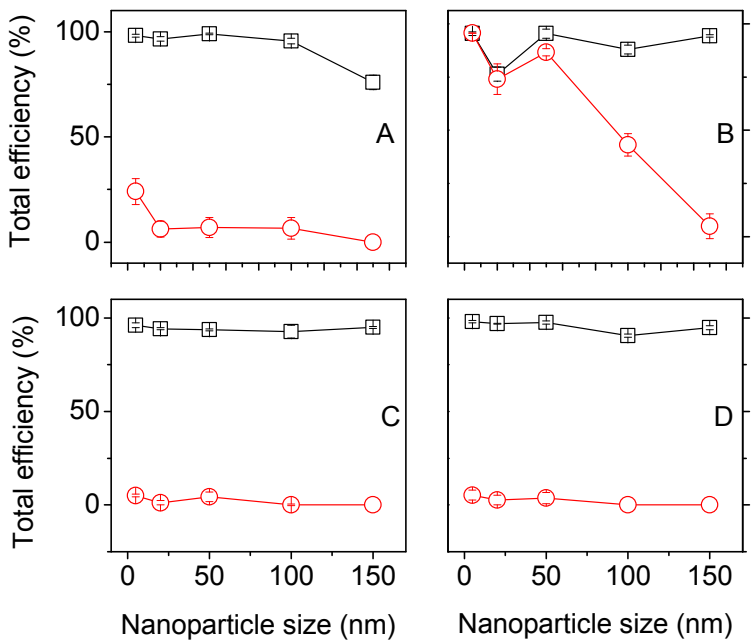

Figure 15.
Comparison of total efficiency at supercritical and control impregnation, of Indian silks: (A) Mulberry (B) Eri (C) Tasar (D) Muga with five different sizes Au NP (5, 20, 50, 100 and 150 nm). Black squares (□) are $scCO_2$ samples, red circles (O) are control samples. Adapted from **Paper 1.**

For the other three silks, namely eri, tasar and muga, the total efficiency of the Au loading was above 90% for $scCO_2$ impregnation, regardless of the Au NPs'

sizes. In the controls, however, eri silks showed exceptionally high efficiency at 98.3 ± 0.01, 89.6 ± 2.9 and 94.6 ± 0.7% for 5, 20 and 50 nm sized NPs, respectively. Beyond, the total efficiency dropped to 77.2 ± 2.1 and 61.9 ± 2.3% for 100 nm and 150 nm NPs, respectively, tasar and muga in the controls showed a total efficiency of about 10%, regardless of the size of the NPs.

Mechanism of Au NPs impregnation on silk fiber

Our observations of the total efficiencies for Au NPs for the four silks' studies showed an all-or-nothing effect, meaning that the process parameters had little influence. Consequently, the four silks behaved identically under $scCO_2$ impregnation, and expectedly, there was no correlation with any of the silk properties shown in Table 1. The only remarkable observation is the control from eri silk that displayed efficiencies comparable to the $scCO_2$ ones, up to 50 nm Au NPs. However, we found no significant properties of eri that could explain this behavior.

Nevertheless, the studied silks could host Au NP with sizes up to 150 nm. In **Paper 1**, the detailed study of the degummed mulberry silk impregnation mechanism suggested that the Au NPs were limited to the silk inter-fibrillar space and, more specifically, around the amorphous regions. Further research on ternary systems comprising "CO_2 + nonsoluble nanoparticles + fibers solid substrates," is required for a detailed understanding of mass transfer and diffusion in the substrate and the influences on the properties of the bulk material, such as crystallinity, morphology, anisotropy and reactivity [107]. Altogether, our results led to the hypothesis that under the supercritical conditions used in our experiment, the transportation of the NPs occur due to a gradient in the surface tension. Park et al. [131] found, for example, that polystyrene (a polymer close to silks) surface tension decreases with CO_2 increased solubility in the polymer (i.e., higher pressures and higher temperatures). Most interestingly, they also found that the polymer surface tension was independent of the polymer conformational entropy; in other words, its internal organization. One could envision a transportation phenomenon akin to the Marangoni flow [132], however, the nature of the gradient remains unclear.

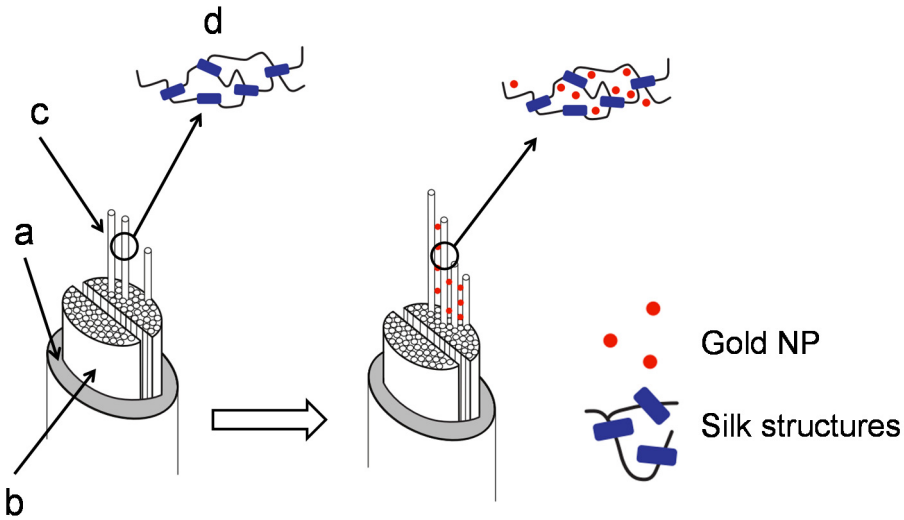

Figure 16.
Au NPs impregnation in silk. The typical silk fiber consists of (a) sericin coating, (b) fibroin brins, (c) fibrils, and (d) the secondary structure (idealized here the β-sheet as blue rectangles and the α-helices, random coils and turns as curvy black lines). After impregnation, the Au NPs were found in the inter-fibrillar spaces. Adapted from **Paper 1**.

Chapter 3. Silk -Manganese dioxide (MnO_2) as enzyme mimics

Nanomaterials can pave a vital route to the fabrication, design and construction of artificial catalysts as enzyme mimics [133-135]. Nanomaterials offer advantageous properties, more than its microsized and bulky counterparts, due to the large surface to volume ratios, better transport properties, new physical properties and confinement effects resulting from its nanoscale dimensions—the basis for designing novel catalysts with multiple functions and applications in energy storage, chemical synthesis, biomedical, thermoelectrics and solar cells [136-143]. Furthermore, these nanomaterials exhibit several characteristics such as controlled synthesis at low cost, flexibility in structure design and composition, tunability of the catalytic activity, higher stability against stringent conditions activities and potential use in bioassays and medical diagnostics [133-135]. Nanomaterials include carbon-based nanomaterials, metal and metal oxide-based nanomaterials [144, 145]. Carbon-based nanomaterials such as carbon nanotubes [146], carbon nanodots [147] graphene oxide [148] and graphene-hemin nanocomposites [149] have been discovered to demonstrate unique, enzyme-mimic catalytic activities. In addition to carbon-based nanomaterials, metal-based and metal oxide-based nanomaterials have also emerged as efficient enzyme mimics [136, 150-153].

Many metal-/metal oxide-based nanomaterials enzyme mimics have been developed, and these nanomaterials have the advantages of low cost and high stability during catalytic activities [134, 136, 138, 139, 146, 150, 151, 154-164]. Practically, mimicking oxidases [139, 150], peroxidases [138, 139, 146, 158-161] and catalases [151, 154, 156, 157, 161, 163, 165] have been focused upon. Examples include FeO_x [138], MnO_x [139] CoO_x (native) [156] and cerium oxide [150, 151]. Recently, many nanomaterials-based enzyme mimics have been developed, such as to mimic oxidases [139, 150], peroxidases [139, 140, 158, 161, 163, 164] and catalases [154, 157, 166]. Examples include iron oxides (FeO_x) [136, 138, 167], manganese oxides (MnO_x) [54, 139, 168-170], cobalt oxides (CoO_x) (native) [156] and cerium oxides [150, 151].

Nanomaterials include carbon-based nanomaterials, metal, and metal oxide-based nanomaterials [144, 145]. Carbon-based nanomaterials such as carbon nanotubes [146], carbon nanodots [147] graphene oxide [148], graphene−hemin nanocomposites [149], have been discovered to show unique enzyme-mimic catalytic activities. In addition to carbon-based nanomaterials, metal-based

nanomaterials, and metal oxides- based nanomaterials have also emerged as efficient enzyme mimics [136, 150-153].

MnO_2 NPs have gathered a considerable amount of interest as an enzyme mimic [54, 139, 168-170]. The wide variety of $MnO_2^{III, IV}$ (i.e., oxidation III and IV) (see Table 4) have been synthesized and used to oxidize various types of organics contaminants [170, 171], and reduce toxic heavy metals [170, 172-174]. Structurally, MnO_2 oxides comprise edge-sharing and/or corners-sharing MnO_6 octahedral crystals, which are further organized to form layered or tunnel structures [170, 171, 174, 175]. MnO_2 exhibits a broad range of absorption peaks (200–600 nm) and is considered one of the strongest oxidizing solid-phase species exsiting in nature [170, 171, 174, 175]. The oxidizing capabilities of $MnO_2^{III, IV}$ depend on several factors, such as the amount of different phases of Mn^{III} or Mn^{IV} (as different phases have different redox abilities), the crystallinity of oxides and surface area [175]. Moreover, single and double coordinated oxygen atoms in MnO_2 at the vacancy and edge sites show different adsorption reactivities [175].

Table 4. Summary of Mn(III/IV) oxides commonly used (reproduced from [170])

Name	Nominal chemical formula	Structure	Example of Model compounds	Notes
Acid birnessite	$Mn^{IV}O_2$	layered	[176]	Referred to as triclinic birnessite
Birnessite	$(Na_{0.3}Ca_{0.1}K_{0.1})(Mn^{IV},Mn^{III})_2O_4 \cdot 1.5H_2O$	layered	[177]	Referred to as δ-MnO_2; interlayer cations vary with synthesis method
δ-MnO2	$Mn^{IV}O_2$	Layered	[178]	Referred to as birnessite or hydrous manganese oxide
Buserite	$Na_4Mn_{14}O_{27} \cdot 21H_2O$	layered	[179]	Hydrated form of birnessite
Feitknechtite (β-MnOOH)	$Mn^{III}OOH$	layered	[180]	
Hollandite (α-MnO2)	$Ba(Mn_6^{IV}Mn_2^{III})O_{16}$	2 x 2 tunnel structure		Often synthesized as nanorods
Cryptomelane	$K(Mn_7^{IV}Mn^{III})O_{16}$	2 x 2 tunnel structure	[176]	Often nanorods/wires
Ramsdellite (γ-MnO_2)	$Mn^{IV}O_2$	2 x 1 tunnel structure		Often nanorods/wires
Pyrolusite (β-MnO_2)	$Mn^{IV}O_2$	1 x 1 tunnel structure	[176]	Often synthesized as nanowires
Manganite (γ-MnOOH)	$Mn^{III}OOH$	1 x 1 tunnel structure	[181]	
Hausmanite	$Mn^{III}_2Mn^{II}O_4$	Spinel	[182]	Natural forms often contain Fe^{III} as an impurity
Biogenic Mn oxides	Often $Mn^{IV}O_2$	Often layered with basic interlay cations		Biogenic oxides contain appreciable amounts of Mn(III)

The most common synthesis procedure of preparing a MnO_2 nanostructure is using the redox method [175, 183], which includes [184] auto-reduction [65] and sonochemical [185] and hydrothermal methods. However, these methods result in the formation of an uneven specific surface area, with suboptimal surface reactivity [183]. Recently, the synthesis of MnO_2 nanostructure material on silk fibers demonstrated the gain in control over the size, dispersion, and stabilization of MnO_2 NPs [53, 54, 65, 169]. The presence of a sufficient amount of amino acids with hydroxyl and carboxyl side chains [186], but also from the recycled tannins from the silkworm plant-based food source [187]. As such, silks offer interfaces amenable to chemical processes such as hydrolysis, redox, and coordination [53, 65, 169, 188].

In **Paper 2** and **Paper 6**, we have found that when optimally prepared, the MnO_2-Silk hybrid fibers can be re-used [54, 169]; However, the mechanism of *in-situ* formation of MnO_2, the catalytic mechanisms, the reason for the stability of MnO_2 NPs on silk, distribution of NPs on, or in an organic template remained unclear [53, 65, 169, 188]. Overall challenge is in measuring and understanding the organic (silk)-inorganic (NPs) interface and how it mediates particle formation as well as long-lasting catalytic activity.

In this chapter, we demonstrate that MnO_2-Silk fiber acted as a satisfactory enzyme mimic exhibiting typical Michaelis–Menten kinetics and high affinity for H_2O_2, OPD, and TMB substrates. We explored the re-usability of the MnO_2-Silk with different substrates (OPD and TMB), and further, we performed acid-base potentiometric titrations to identify the distribution of pK on the MnO_2-Silk fibers to infer the possible distribution of the MnO_x oxides. Next, we explain the development of an *in situ* monitoring method, providing new insights into the kinetics of the formation of MnO_2 nanoparticles on silk film and their enzymatic activities. Furthermore, from a multivariate component analysis view, the transformation of MnO_2 from $KMnO_4$ using sonication and auto-reduction was also analysed. Additionally, we also examined the direct analysis of the kinetic and kinetic rates for the formation of MnO_2 NPs on silk film as well as the *in situ* catalysis of TMB using sonication and auto-reduction. To separate the contribution from MnO_x from the silk, we used a combination of anomalous X-ray small-angle scattering (ASAXS) and near-edge X-ray absorption fine structure (NEXAFS).

Characterization of MnO_2-Silk fiber

XRD

In **Paper 2**, we identified XRD patterns of the four silks at optimal manganese oxide conditions; (a) mulberry, (b) eri, (c) muga, and (d) tasar. The manganese

dioxide is identified at 36.7° corresponding to (100) reflection and 65.7° corresponding to the (110) reflection [2,14].

FTIR

In **Paper 2**, to clarify the chemical environment of the MnO_2 NPs, we measured and compared the FTIR-ATR spectra in the region below 1000 cm^{-1} of the unmodified silks and the MnO_2-Silk fibers. The four silks modified with MnOx showed clear differences in the FTIR-ATR peaks' positions. This suggested, in addition to a dominant MnO_2, that other polymorphs of manganese dioxide were present.

MnO_2-Silk reactivity

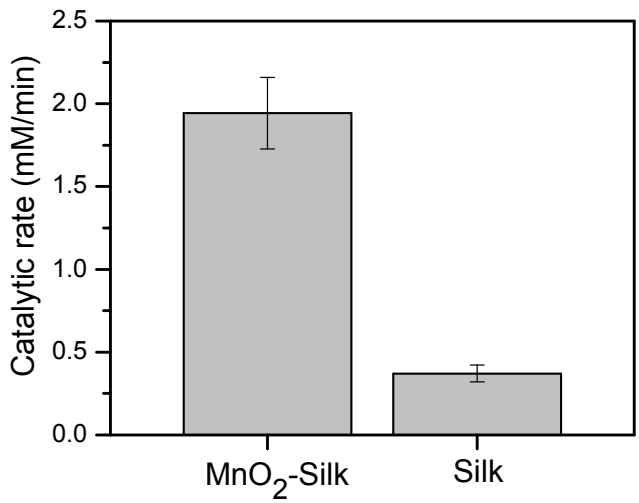

Figure 17.
Decomposition of H_2O_2 by MnO_2 silk fiber and untreated silk. The catalytic degradation rate of 25 mM H_2O_2 by MnO_2-Silk fiber and native silk was 1.94 ± 0.21 and 0.37 ± 0.05 mM/min, respectively. Adapted from **Paper 3**.

Figure 17 shows that MnO_2-Silk exhibited catalase like activities, i.e., MnO_2-Silk facilitate the decomposition of H_2O_2 while the untreated silk showed a minimal effect. How is the decomposition mediated? $Mn^{IV}O_2$ and H_2O_2 are both oxidants. Already in 1947, Broughton *et al*. [189] demonstrated that the following equation governed the potential (i.e., oxidative capacity) of the bare MnO_2 NPs:

$$MnO_2 + 4H^+ + 2e^- \rightarrow Mn^{++} + 2H_2O \quad (13)$$

And that the solution immediately adjacent to the MnO_2 surface was saturated with manganese hydroxide Mn(OOH). The authors found that the decomposition of the H_2O_2 occurs within the manganese hydroxide interface. It is now generally agreed [190] that the excess surface oxygen enhances the decomposition of H_2O_2 via the following reaction:

$$H_2O_2 + O_2^- \rightarrow O_2 + OH^- + OH^- \qquad (14)$$

Later on, Kanugo *et al*. [191] showed that the active site on the same bare MnO_2 NP, for the decomposition of H_2O_2, is Mn^{4+} in the pH range of 3–8, and Mn^{3+} in pH the range 8–14. Importantly they observed, that the decomposition of H_2O_2 attains its maximum at pH of about 11.5–12.0 and then decreases with a further increase in pH. In summary, if the MnO_2 catalyst donates an electron, then the possible active site is Mn^{3+}:

$$Mn^{3+} + H_2O_2 \rightarrow OH^- + OH^- + Mn^{4+} \quad (15)$$

On the other hand, if the catalyst accepts an electron, the possible active site is Mn^{4+}:

$$Mn^{4+} + H_2O_2 \rightarrow H^+ + HO_2 + Mn^{3+} \qquad (16)$$

The relative rates of both reactions depend on the redox potential of the catalyst in the pH of the medium (equation 13). They further propose that the catalytic form of MnO_2 would have the following stoichiometry: $Mn_{1-x}^{4+}Mn_x^{3+}O_{2-x}(OH)_x$. In this model, Mn^{3+} ions have replaced Mn^{4+} and allow for favorable electron exchange for the catalytic activity.

Moving away from the bare particles, not much chemical information is available for the templated MnO_2 NP. One approach is to determine the structure of MnO_2 and infer the possible reactivity. Triller *et al*. [157] successfully produced binuclear manganese complexes with organic molecules as templates; they found that complex with $Mn_2^{II,\,II}$ and $Mn_2^{III,\,IV}$ (similar to the corresponding oxidation states of manganese catalase from *Thermus thermophilus* and *Lactobacillus plantarum*) had an efficient catalyst for the disproportionation of hydrogen peroxide. From their work and others [175, 192, 193], a correlation emerges on the role of the organic template, the structures of the Mn_2 and MnO_x complexes, and their chemical reactivity.

When using larger-sized templates, for example, Liu et al. found using X-ray powder diffraction (XRD) that for MnO_2 templated by bovine serum albumin (BSA) the γ-MnO_2 was the predominant form. They also found using X-ray photoemission spectroscopy (XPS) that there were three types of oxygen species in different oxygen-containing functional groups: the oxygen in Mn–O–Mn, the oxygen in Mn–O–H, and the oxygen in H–O–H. However, no direct evidence for

the oxidation states. In **Paper 2**, we found using XRD that instead, the δ-MnO_2 form was dominant in the MnO_2-Silk hybrid [169]. Interestingly manganese oxide is invariably δ-MnO_2 with a distribution of $Mn^{II, III, IV}$ [170, 194]. Generally, with the increasing size and complexity of the templating phase, it is more and more challenging to extract chemical and structural information of the metal or metal oxides.

We choose, therefore, to approach the reactivity of the MnO_2-Silk via potentiometric titration and a selection of substrates. The rationale for that comes from equation (13) and the dependence of the MnO_2 oxidative potential on pH; and equations (15) and (16) combined with a judicious choice of substrates, namely H_2O_2 (catalase activity), TMB (oxidase activity), OPD (oxidase activity), TMB + H_2O_2 (peroxidase activity), OPD + H_2O_2 (peroxidase activity).

pK distributions

The role of pH and surface-active oxygen prompted us to measure the surface properties of the MnO_2-Silk hybrid fibers. We, therefore, used potentiometric acid-base titration to calculate the pK distribution of MnO_2-Silk, and MnO_2 micro-sized particles (control) and the untreated silk fiber. We used a base titration with an overnight acidification method (see Chapter 1, characterization techniques section for details) to ensure a full protonation of all accessible and titratable species. Figure 18 summarizes the pK distributions for the MnO_2-Silk, MnO_2 control particles, and silk.

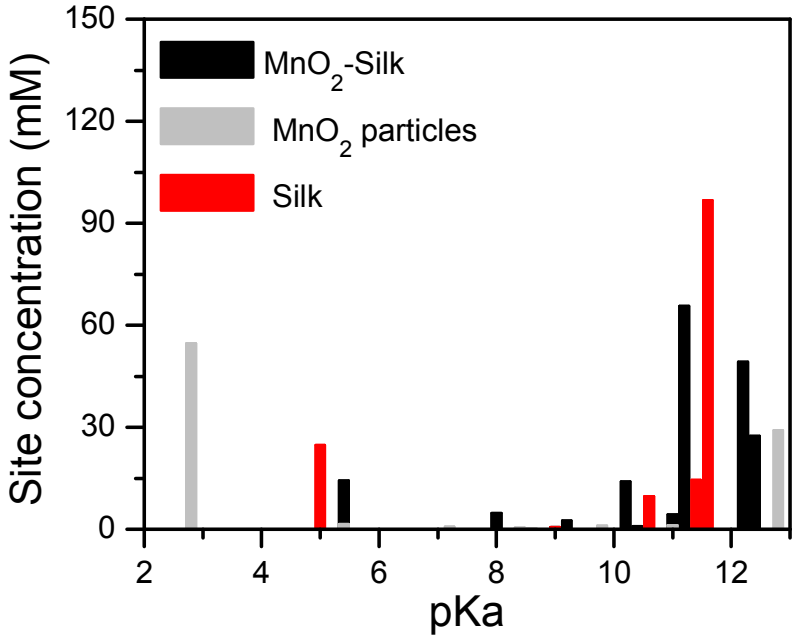

Figure 18.
pK distribution of MnO_2-Silk, MnO_2 particles, and silk, after overnight acidification and rinsing (see materials and methods section for details). Adapted from **Paper 3**.

For the commercially available MnO_2 particles, the pK distribution showed a significant peak at around pH = 3, in keeping with the reported point of zero charges for MnO_2 [195]. Although not directly comparable, the commercially available MnO_2 provided a reference point. For the MnO_2-Silk, we found no peak at around pH = 3 in the pK distribution. We found a pK at around 5.2, higher than the pK of about 4.5 found in the fique-MnO_2 hybrid fiber system [168]. We also observed that the native silk had a pK at 4.5, which disappeared or shifted in the MnO_2-Silk system. Overall, native silk and MnO_2-Silk showed different pK distributions. MnO_2-Silk, pK distribution around pH = 5, 8, 9, and 10 suggested (when we excluded the contributions from the bare silk and water alone) the co-existence of $Mn^{III}O_2$ and $Mn^{IV}O_2$ [190, 196]. As for other polyvalent metal oxides hydrates, the surface sites of colloidal hydrous manganese dioxide is amphoteric [196]. Within the pH range considered and above the point of zero charges, the acid-base behavior of MnO_2 can be split into an acid H_2MnO_3, and the oxides Mn_2O_2 and Mn_3O_4 [196]. The titration of the supernatant after the MnO_2-Silk overnight acidification showed more peaks in the pK distribution at around pH = 6, 7, and 9 (data not shown). Noteworthy, a portion of MnO_2 NP on the MnO_2-Silk fibers was released in solution by acid equilibration (and not by rinsing), suggesting that in any re-usability studies, MnO_2 could be further detached from the surface and contribute to the loss of total activity after each cycle.

Kinetics analysis of MnO_2-Silk fiber activities

UV-visible absorption spectroscopy was used to investigate the kinetics of the TMB and OPD oxidase and peroxidase activities MnO_2-Silk, and amperometry was used to measure the catalase- like activity for the decomposition of H_2O_2. The data were fitted to the Michaelis–Menten model, and the parameter summarized in Table 5.

Table 5. Kinetic parameters of the MnO_2-Silk. Adapted from Paper 3.

Catalyst [a]	Type of reaction	Substrate	K_m (mM)	V_{max}
MnO_2-Silk	catalase	H_2O_2	11.13 ± 2.26	2.74 ± 0.25 mM/min
MnO_2-Silk	oxidase	TMB	0.72 ± 0.25	0.85 ± 0.19 mM/min
MnO_2-Silk	peroxidase	TMB + H_2O_2	1.22 ± 0.42	0.93 ± 0.24 mM/min
MnO_2-Silk	oxidase	OPD	50.99 ± 38.3	0.49 ± 0.31 mM/min
MnO_2-Silk	peroxidase	OPD + H_2O_2	26.75 ± 20.10	0.42 ± 0.23 mM/min
HRP[b]	oxidase	OPD	0.59	2.8 μM.min^{-1}
HRP[b]	peroxidase	H_2O_2	0.34	5.7 μM.min^{-1}
MnO_2-BSA[b]	catalase	H_2O_2	14.31	2.5 μM.min^{-1}
MnO_2-BSA[b]	oxidase	OPD	0.31	4.9 μM.min^{-1}
MnO_2-BSA[b]	oxidase	TMB	0.04	346.8 μM.min^{-1}

[a] the untreated silk showed no activity towards H_2O_2, TMB, and OPD
[b] Data from reference [139]

For the oxidase-like activity with TMB and OPD substrate, $K_m = 0.72 \pm 0.25$ mM, $V_{max} = 0.85 \pm 0.19$ mM/min and $K_m = 50.99 \pm 38.3$ min^{-1}, $V_{max} = 0.49 \pm 0.31$ mM/min were obtained, respectively. And for peroxidase-like activity with TMB and OPD substrate, $K_m = 1.22 \pm 0.42$ mM, $V_{max} = 0.93 \pm 0.24$ mM/min and $K_m = 26.75 \pm 20.10$ mM, $V_{max} = 0.42 \pm 0.23$ mM/min were obtained, respectively. The K_m values for the catalase like activity by MnO_2-Silk and MnO_2-BSA were comparable to one and other. The same was valid for oxidase/peroxidase-like activity against TMB substrate, while the results tested against OPD were dramatically different. No reasonable comparison could be drawn from the V_{max} since the amounts of MnO_2-Silk catalysts were not accessible, and the amounts of H_2O_2 used for the peroxidase reactions were different.

Importantly, we observed that at different pH levels of 5, 7.4 and 9, the rates of substrates degradation decreased (Figure 19). Simply said, the electron donor capability of the Silk-MnO_2 was reduced. According to equation (15), it meant that Mn^{3+} was less and less available. Equation (13) suggested for increasing pHs a more stable MnO_2. According to our potentiometric titration the putative reactive species $Mn^{4+}_{1-x}Mn^{3+}_{x}O_{2-x}(OH)_x$ had a pK of approximately 5.2; consequently, at increasing pHs, the reactive species should carry more negative charges; and most likely influence the adsorption of the substrates onto the catalysts.

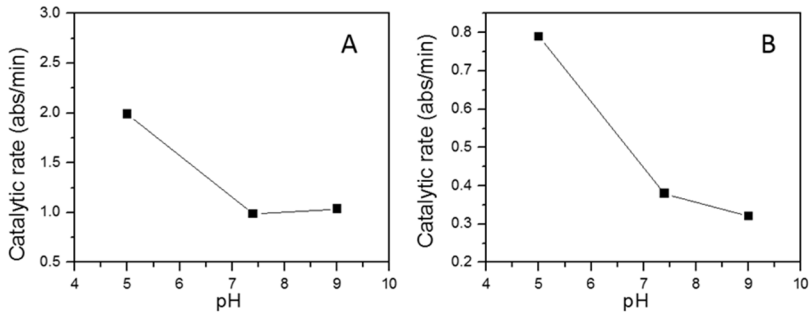

Figure 19.
The relative catalytic activity (taking account of leakage activity) at different pH = 5, 7.4, and 9, were measured with the OPD substrate to have (A) a peroxidase-like activity and (B) an oxidase-like activity. For TMB substrate, the same pattern is obtained (data not shown).

Others have suggested that the different forms of MnO_x such as $Mn_2(OH)^{3+}$, $Mn(OH)_2$ distribution on the silk fibers were the reason for the pH effects. Interestingly, in **Paper 2,** our result from FTIR supported the structural polydispersity of MnO_2 [169]. The single pK for the MnO_2-Silk found suggested that even though we observed a structural diversity, only one species was active.

Operational stability of MnO_2-Silk

Using MnO_2-Silk fiber, we conducted an operational stability or recyclability test. This test consisted of successive oxidation of TMB and OPD substrates by the same fiber for the peroxidase (with H_2O_2) and oxidase-like activities (without H_2O_2), respectively. The method illustrated in figure 8 allowed us to estimate the activity from the MnO_2-Silk fibers alone and some leaked activity from loosely attached MnO_2 NPs. Figures 20A and 20B show the peroxidase (with H_2O_2) like activities with TMB and OPD, respectively. Similarly, Figure 20C and 20D showed the oxidase (without H_2O_2) like activities with TMB and OPD, respectively.

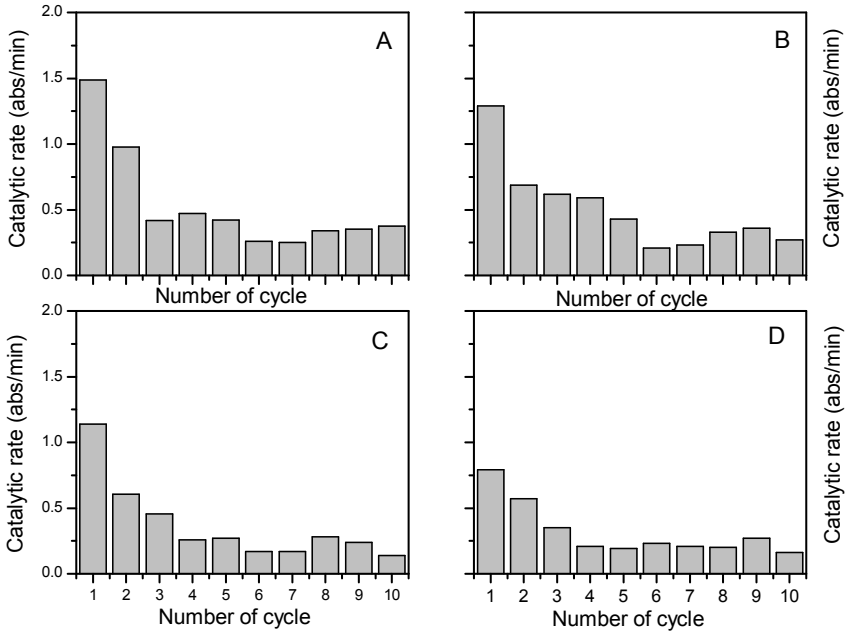

Figure 20.
Operational stability (re-usability) of the MnO_2-Silk for peroxidase (with H_2O_2) like activity (A) (B); and oxidase (without H_2O_2) like activities (C) (D) with TMB and OPD substrates, respectively. Adapted from **Paper 3**.

Remarkably after about 2-3 cycles, the catalytic activities were stable at around 25-30 % of the starting activity. A cautionary warning, though, Drodz *et al*. [197] found that the use of TMB, OPD, and ABTS, substrates designed for horseradish peroxidase, can yield anomalous catalysis depending on the pH, substrate concentration and metal/metal oxides concentration, and the amount of H_2O_2 used. The possible anomalous catalysis might explain, in part, the initial rates we observed.

Generally, the biphasic nature of the relative rate of degradation (faster loss in the first cycles and slower changes in the following cycles) was also reminiscent of the typical biphasic behavior observed for immobilized enzymes. Note that this applies because we considered only the catalytic activity from the fibers. By analogy, therefore, in the first 2-3 cycles, the MnO_2-Silk fibers lose the MnO_2 that could be deactivated. In our context, the MnO_2 able to lose its Mn^{III} reactive component irreversibly. For the later cycles, the MnO_2 left on the fibers were well anchored and stabilized in the $Mn^{4+}_{1-x}Mn^{3+}_{x}O_{2-x}(OH)_x$ form. Most importantly, the constant rates observed with increasing cycle numbers suggested an actual catalytic mechanism as compared to the typical stoichiometric reactivity of the bare MnO_2 particles.

Direct analysis of the kinetics

In **Paper 4**, first, we develop optically, transparent, and stable silk film, since support needs to have optical transparency while monitoring using UV-vis spectroscopy. Then, we present a detailed analysis of the process parameters that allowed us to find optimal conditions to have the most stable silk film with highly catalytic MnO_2 NPs. Using these optimal conditions, we followed the auto reduction and sonication kinetics by *in-situ* monitoring the absorbance of the characteristic UV-vis wavelength of $KMnO_4$ and MnO_2.

Auto-Reduction kinetics

Figure 21 shows the UV spectra kinetic series of the auto-reduction (no-sonication) conversion of $KMnO_4$ into MnO_2 in the presence of a silk film. The spectra were collected every 4 seconds for 16 h. Note the disappearance of the $KMnO_4$ peaks between 500 and 600 nm, and the scattering contribution from 400 to 1000 nm. To remove the scattering effect and resolve more peaks, we computed the second derivative of the kinetics spectra. To detect the peaks that changed during the kinetics, we used a power spectrum analysis [71]. The power spectrum showed only the peaks that changed during the kinetics. The power spectrum is only positive, meaning that we do not know if a peak change is positive or negative.

Figures 21C and 21D show the power spectra associated with the raw data and second derivative, respectively. We observed a significant peak forming at around 459 nm and tentatively assigned this peak to MnO_2. $KMnO_4$ peaks were readily identified with a center peak at 525 nm. Note the upturn at 600 nm, which was associated with an increase in baseline due to the increase of the scattering contribution from NPs. Interestingly, Figure 21D showed a more detailed contribution in the region between 400 and 500 nm, as well as below 300 nm.

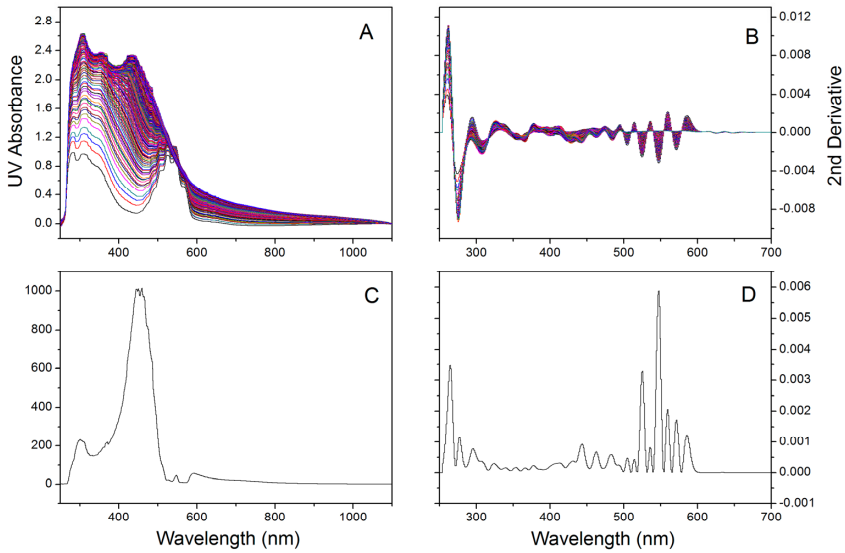

Figure 21.
(A) UV spectra kinetic series of $KMnO_4$ into MnO_2 in the presence of a silk film with auto-reduction (no-sonication) and (B) 2nd derivative, power spectrum for raw kinetics (C) and (D) 2nd derivative. Adapted from **Paper 4**.

In the former, we identified three main peaks suggesting three different sizes or species of MnO_2 NPs. In the latter, the position of the peak suggested changes associated with the silk proteins. Using merely the signal at 459 nm (MnO_2) and 525 nm ($KMnO_4$), we plotted, the kinetics of the process (Figure 22).

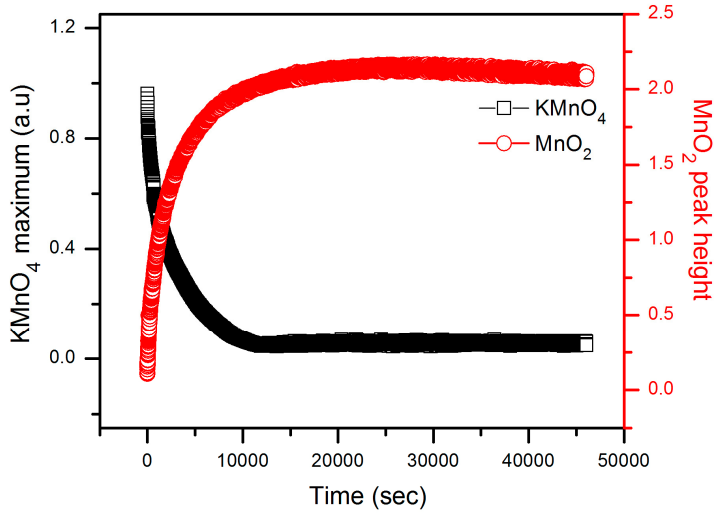

Figure 22.
The rates of MnO_2 formation and $KMnO_4$ consumption extracted from the power spectrum in the case of the auto-reduction of permanganate on silk film. Adapted from **Paper 4**.

The quantification of the kinetics rates for the MnO_2 growth curve and $KMnO_4$ decrease curve was performed using XP-Fit software. Table 6 summarizes the rates of these exponential terms.

Sonication kinetics

Figure 23 shows the UV spectra kinetic series of the sonication induced conversion of $KMnO_4$ into MnO_2 in the presence of a silk film. The spectra were collected every 4 seconds for 30 minutes. To remove the scattering effect and resolve more peaks, we computed the second derivative of the kinetics spectra.

Figure 23C and 23D show the power spectra associated with the raw data and second derivative, respectively. We observed a significant peak forming at around 430 nm (Figure 23C). We tentatively assigned the 430 nm peak to MnO_2. $KMnO_4$ peaks were readily identified (Figure 23D) with a center peak at 525 nm.

Interestingly, when comparing Figure 21D and 23D, we found that the MnO_2 contribution for the sonication had only one broad peak instead of three. The difference suggested a more monodisperse particle formation and, or less, chemical polymorphism. At that point, because of the limited sample thickness, any X-ray powder diffraction analysis to identify the MnO_x failed.

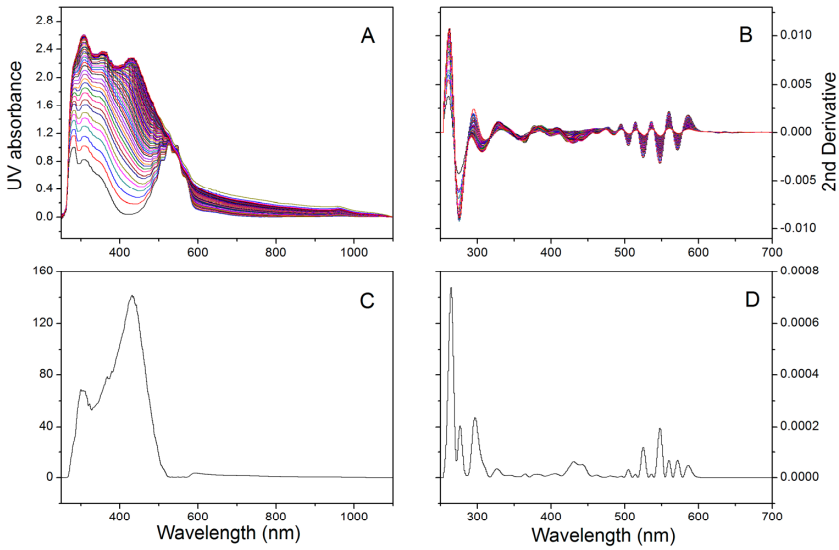

Figure 23.
(A) UV spectra kinetic series of $KMnO_4$ into MnO_2 in the presence of a silk film with sonication) and (B) second derivative, power spectrum for raw kinetics (C) and (D) second derivative. Adapted from **Paper 4**.

We also found when comparing Figures 23C and 21C that the sonication peak associated with MnO_2 was formed at 439 nm, whereas, in the auto-reduction process, the peak was formed at 459 nm. The observed shift towards lower wavelength was associated with smaller sized MnO_2 NP. The rates corresponding to the signal of MnO_2 (at 439 nm) and $KMnO_4$ (at 525 nm) are plotted in Figure 24.

Two controls ($KMnO_4$ with no silk film) were run for 30 min and 16 h, under the same sonication and auto-reduction conditions. From the kinetics, we observed no peak formation between 400 and 500 nm for both conditions. The second derivative showed a small change in the 360-380 nm region. We also observed that the $KMnO_4$ peak intensity at around 525 nm did not change much compared to the previous two processes (in the presence of silk). The power spectrum shows that there is a significant peak formation at 380 nm. A careful reading of the second derivative spectra, however, shows no significant change in this region but a baseline shift at the lower wavelength. Regardless of this effect, we can exclude the formation of MnO_x particles (intermediate form, in the formation of MnO_2). For example, Mn_3O_4 has an absorption peak at 380 nm [10].

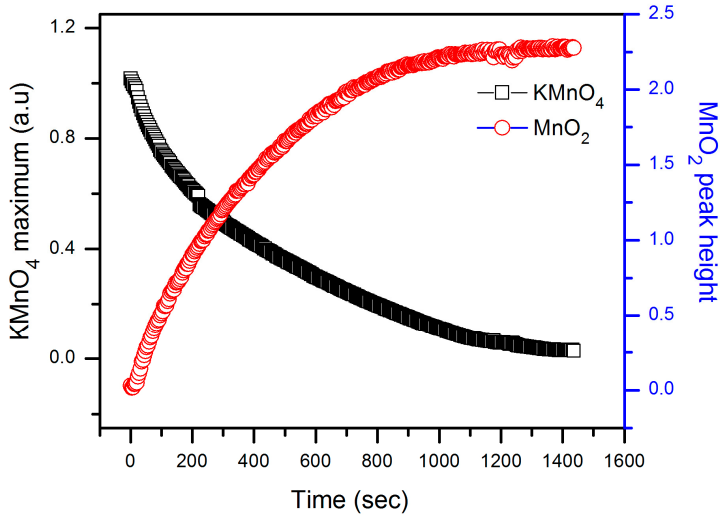

Figure 24.
The rates of MnO_2 formation and $KMnO_4$ consumption extracted from the power spectrum in the case of sonication of permanganate on silk film. **Adapted from** Paper 4**.**

Evaluation of the kinetic rates

Evaluation of the kinetic rates from single wavelengths decay curves

With respect to the analysis of the kinetics rate for the MnO_2 growth curve, the $KMnO_4$ decrease curve was obtained using XP-Fit software. Several exponential terms were fitted using XP-Fit, and the number of significant exponentials to fit was determined by using an F-test. The comparison of the rates (Table 6) demonstrated that sonication accelerated the formation of MnO_2.

Table 6. Rates of $KMnO_4$ consumption and MnO_2 formation. Adapted from Paper 4.

Process	Rates of the reaction (abs/s)	
	$KMnO_4$ Consumption	MnO_2 Formation
Sonication	0.0035	0.013
		0.0017
Auto-Reduction	0.002	0.009
	0.0002	0.001
		0.0002

Most interestingly, the auto-reduction process had one more rate for the $KMnO_4$ consumption and MnO_2 formation as compared to the sonication process. We tentatively assigned this very slow step with the maturation of the particles.

The finding that auto-reduction has one extra rate than sonication suggested the two different routes in kinetics for the transformation of $KMnO_4$ to MnO_2 on silk film under sonication and no-sonication conditions.

Multivariate curve resolution of the kinetics of MnO_2 formation

To understand the mechanism of MnO2 formation, the multivariate curve resolution analysis – weighted alternating least square (MCR-WALS) method was used to uniquely identify the species (fractional concentration) involved in the reaction [78, 198]. Figure 25 summarizes the components spectra and their composition as a function of time for sonication with and without silk. We found three components for the kinetics of formation of MnO2 with silk by sonication and two components in the absence of silk.

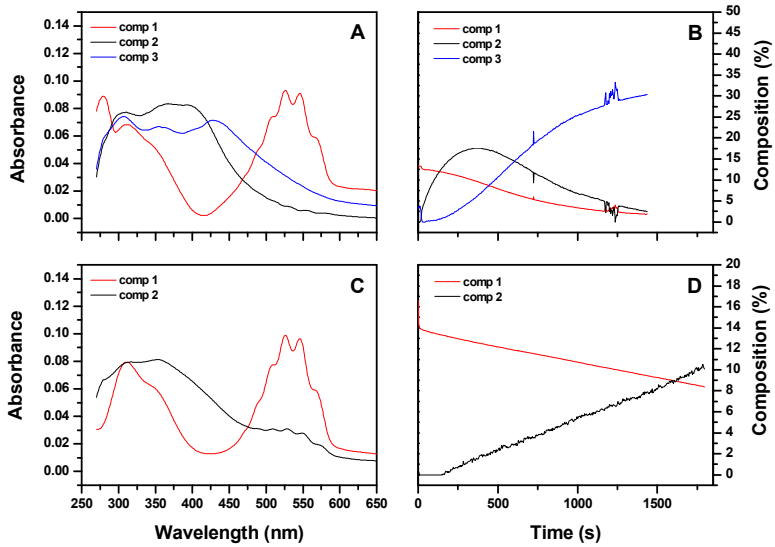

Figure 25.
Component analysis for the sonication method for MnO_2 formation from $KMnO_4$ with silk. Panel (A) and (C) are the component spectra with silk and without silk, respectively. Panel (B) and (D) are the concentration profiles with and without silk, respectively. Adapted from **Paper 4**.

From Figure 25, we readily identified component 1 as $KMnO_4$ and component 3 as MnO_2. On the other hand, Component 2 from the concentration profiles (Figure 25) appeared quickly and progressively disappeared as MnO_2 was formed. We tentatively assigned component 2 to a complex between the silk and MnO_x.

For auto-reduction, we also found 3 components for the formation kinetics of MnO_2 (Figure 26). Component 1 corresponded to $KMnO_4$ and component 3 to MnO_2.

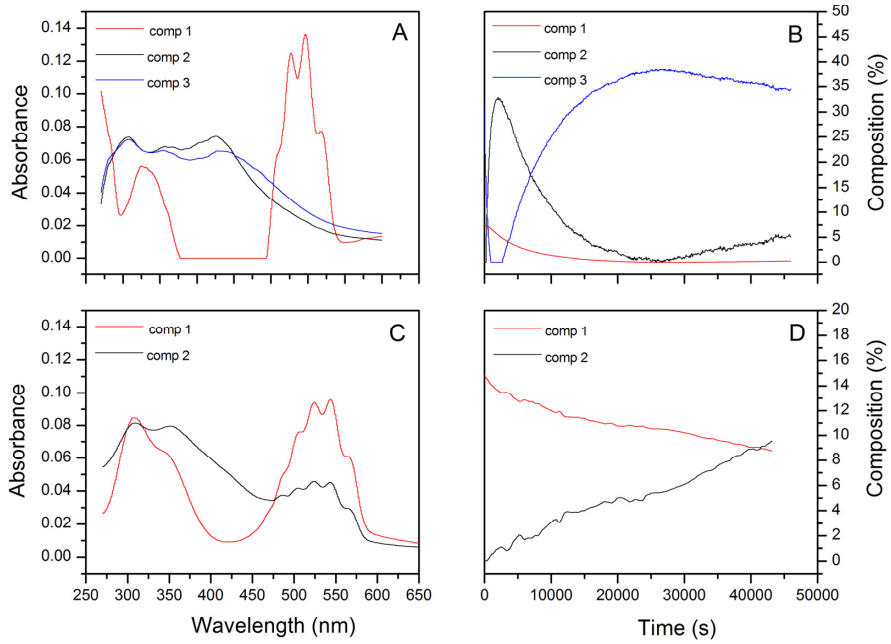

Figure 26.
Component analysis for the auto-reduction method for MnO_2 formation from $KMnO_4$ with silk. Panel (A) and (C) are the component spectra with silk and without silk, respectively. Panel (B) and (D) are the concentration profiles with and without silk, respectively. Adapted from **Paper 4**.

When we compared component 3 in sonication and auto-reduction, we found a better-defined peak of MnO_2 in the sonication sample than with the auto-reduction sample. The intermediate component 2 in both cases appeared to have the same concentration profile suggesting the same synthesis route. However, the spectra appeared to be different. The $KMnO_4$ signal sharply shadowed the silk contribution. However, when we took into account the component analysis of the samples without silk. We found that the protein peak at 208-295 nm (from tyrosine and tryptophan) changed during the kinetics.

In-situ catalysis of TMB by the MnO_2-silk film

In a manner similar to the *in-situ* monitoring of the MnO_2 NPs formation, a method was developed to measure the activity of MnO_2-Silk film with the TMB substrate. Typically, the MnO_2-Silk film was added to the cuvette containing TMB along with buffer, and the course of the catalysis recorded immediately. Figure 27A shows the kinetics of a MnO_2-Silk film with TMB carried out for 2 minutes with continuous stirring of the reaction mixture. In the graph, we

observed the formation of a peak at 652 nm (and 900 nm), correlated to the appearance of blue color as the reaction happened (Figure 27B).

Similarly, the activity of the MnO_2-Silk from the auto-reduction process is shown in Figure 25C, and 25D was also tested with TMB substrate. The Figure 25C shows the kinetics of TMB oxidation and Figure 27D the traces at 650 and 900 nm.

A direct comparison of the specific activity of the two processes was precluded by the inability to estimate the amount of MnO_2 in each film. Nevertheless, assuming the same amount of MnO_2 (e.g., we observed the same % $KMnO_4$ consumption), we could confirm that sonication yielded better catalysis for the sonication sample. Interestingly, we found a toe region in Figure 27B that is not present in Figure 27D. The delayed catalysis suggested a diffusion-limited step, most likely from the difference in the accessibility of MnO_2 in both samples. For example, MnO_2 for the sonication method would be more buried within the silk film than the MnO_2 from the auto-reduction method.

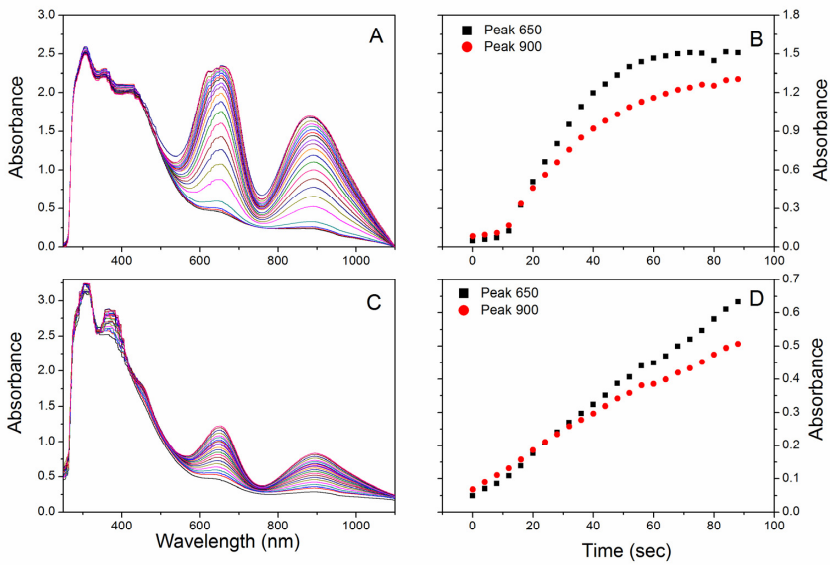

Figure 27.
In-situ catalysis of TMB substrate for sonication process (A), and extracted rates at 650 and 900 nm (B). Auto-reduction process, catalysis (C), and extracted rates at 650 and 900 nm (D). Adapted from **Paper 4**.

Synthesis of MnO_2 on silk fibers

Silk fiber has a complex structural and chemical composition as described in Chapter 1 [37, 199]. Figure 28 considers the silk fibers at different levels: it mainly consists of a gummed outer layer called sericin (Figure 28a) and fibroin (Figure 28b). Silk fibroin is composed of numerous minute fibrils (Figure 28c), which could be separated into crystalline (β-sheet crystals with strong hydrogen bonding) and amorphous regions with varying degrees of hydrogen bonding.

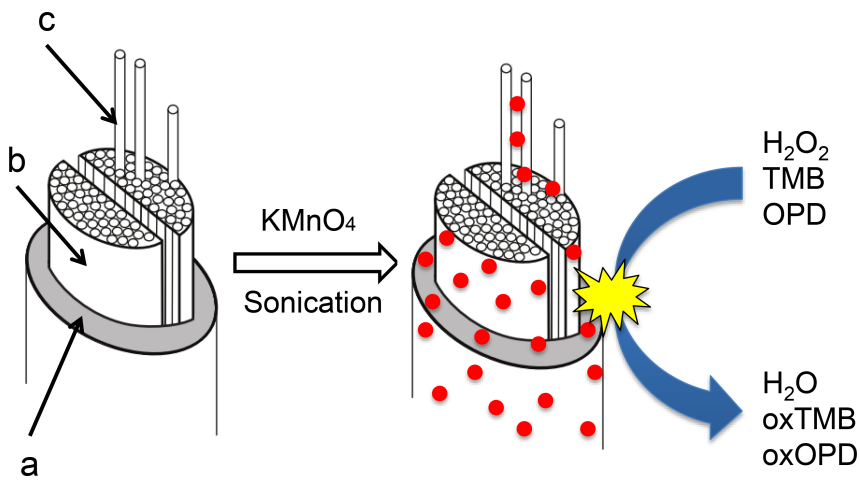

Figure 28.
A putative mechanism for MnO_2 formation and catalytic activity. The fiber to the left is the native silk with sericin coating (a), the fibroin brins (b), and the fibrils (c). Upon sonication and in the presence of $KMnO_4$, MnO_2 is formed and deposited on and into the fiber. The stabilized MnO_2-Silk hybrid showed catalase, oxidase, and peroxidase-like activities. Adapted from **Paper 3**.

The formation of MnO_2 on/in the silk may be a multistep process involving the binding of MnO_4^- molecule, followed by reduction, nucleation, and crystal growth to form MnO_2 NPs. Other studies have suggested that the silk regions containing tyrosine residues could help for the reduction of MnO_4^- precursor to MnO_2 NPs [54, 169]. The optically transparent silk films and an *in-situ* sonication approach showed smaller size, more mono-dispersed, and deeper buried MnO_2 NPs in silk film conferred a higher catalytic activity and stability to the hybrid material. The MnO_2 NPs formation followed a two exponentials growth rates with an identified (MnO_x – Silk) complex as intermediate.

To simplify the experiment, we choose only two types of silks and two concentrations of the starting $KMnO_4$ (i.e., 5 and 20 mM). A complete exploration of the parameters can be found in **Paper 2**. For the silks, we choose the *Bombyx mori* silkworm silk, domesticated and widespread silk, and the wild Tasar silk from the *Antheraea mylitta* silkworm. Note that Tasar silk is structurally (generally, the saturniid family) very similar to spider silk [200, 201], as compared to *Bombyx mori* silk.

Standard SAXS

Figure 29 compares the standard (i.e., non-energy resolved) SAXS for the untreated silks, and the silks treated with 5 and 20 mM of $KMnO_4$. The native silks showed the well-documented double diffraction peaks from the β-sheet crystals at around 1.3 and 1.6 nm^{-1} [202]. In the case of Tasar, only one of the peaks is visible. In the presence of manganese oxides, a broad peak appeared at around 0.75 nm^{-1} and 1 nm^{-1} for the Mulberry and Tasar silks, respectively. A rough estimate suggested small particles in the 5 to 8 nm range in diameter. Note the disappearance of the silk diffraction peaks. We found, however, by FTIR-ATR that the secondary structures of the silks, as well as β-sheets structure content, did not change significantly (data not shown).

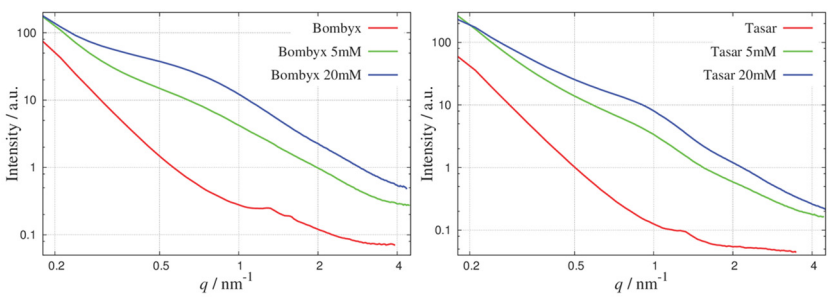

Figure 29.
Features around q = 1 nm^{-1} show the formation of small MnO_x particles of MnO_2 supported Bombyx and Tasar. Further, these feature increases with increasing concentration of $KMnO_4$. Adapted from **Paper 5**.

ASAXS

The measurements were performed at 7 different energies close to the Mn absorption K-edge between 6450 and 6538 eV. The data has been normalized to a Glassy Carbon with 90 μm thickness. Figure 30 shows an overlay of SAXS curves at four different energies. The ASAXS effect was more pronounced for the 20 mM than 5 mM treated silks. We noted the broad peaks at around 0.75

nm^{-1} (*Bombyx mori*), and 1 nm^{-1} (Tasar) decreased in intensity with increasing incident X-ray energy. The intensity decrease supported the fact that most of the Mn were in a particle form.

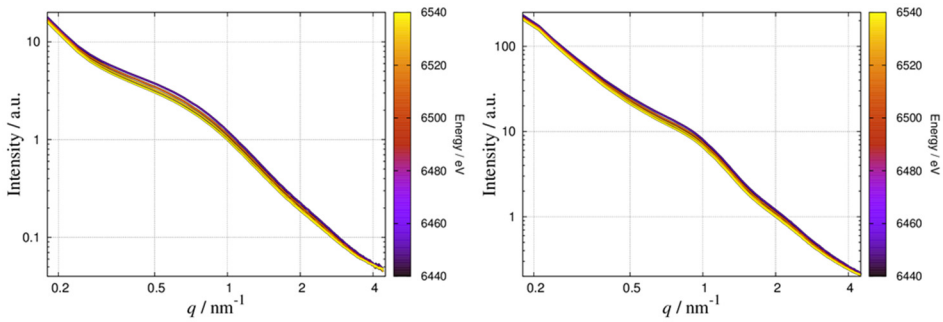

Figure 30.
Energy resolved SAXS curves for Mulberry and Tasar treated with 20 mM of $KMnO_4$. Each panel shows four scattering curves of the ASAXS sequence. Adapted from **Paper 5**.

Resonant term evaluation

We used the scattering curves measured at three different energies near the absorption edge (at 6538 eV), to decouple the scattering contribution of the Mn-containing parts from the rest. Figure 31 shows the scattering corresponding to parts of the sample containing Mn.

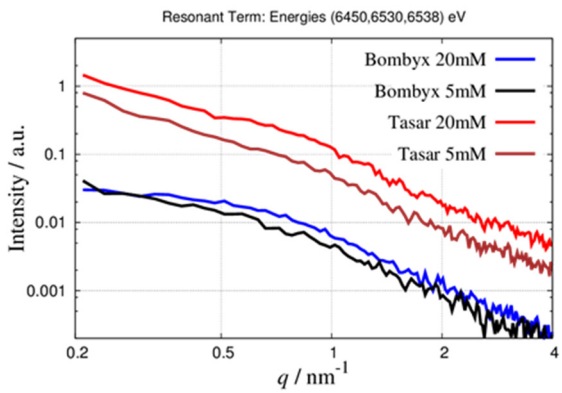

Figure 31.
Resonant term calculated for the samples containing manganese. Adapted from **Paper 5**.

We tentatively considered the MnO_2 as colloids of a spherical shape with a typical lognormal size distribution. Figure 32 (left panel) shows the fit for this form factor to the resonant term. There is a good agreement between the fit and the data in

the mid-q region. In the low-q region (i.e., larger sizes), the Tasar silk fit deviated more than the one from the *Bombyx mori*. Typically, an upturn at lower q is associated with aggregation. Here we suggested that the Mn colloids in the Tasar silk showed some kind of aggregation or maybe a fractal supra-structure along the silk. Similar behavior is also observed for the lower permanganate solution (5 mM) with Tasar silk and yet not for the *Bombyx mori* silk (data not shown).

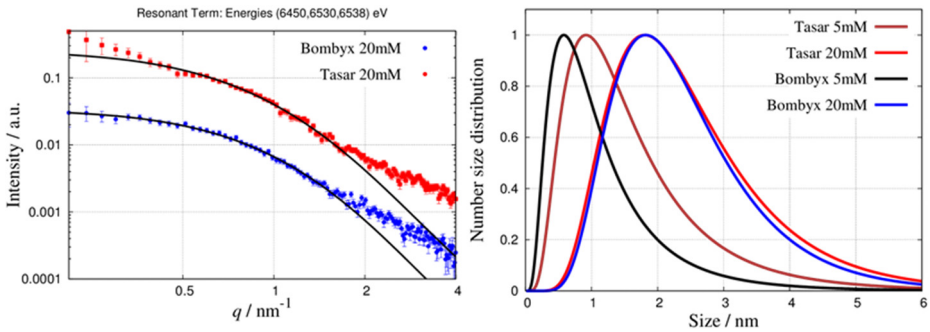

Figure 32.
The fit of the form factor (Left panel) and colloidal size distribution (Right panel). The model used to fit the resonant terms consists of spherical objects with a lognormal size distribution. Adapted from **Paper 5**.

Figure 32 (right panel) illustrates the size distribution of the Mn-colloids for the four cases. We observed that the size of the Mn-colloids increased when increasing the permanganate concentration. Interestingly, at low permanganate concentration, the *Bombyx mori* silk had smaller Mn-colloids than Tasar silks. At 20 mM permanganate, no differences were observed. The variation in size suggested an influence from the silks' morphologies, structures, and interfacial chemistries.

NEXAFS – Oxidation states

Figure 33 summarises the NEXAFS evaluation. Figure 33 (left panel) compares the 20 mM $KMnO_4$ treated silks with commercially available $Mn^{IV}O_2$ micro-particles. The three samples appeared very similar, suggesting that $Mn^{IV}O_2$ was the dominant form of Mn on the silks. For comparison, we measured the NEXAFS for commercially available Mn(II), Mn(III), Mn(IV), and the permanganate Mn(VII).

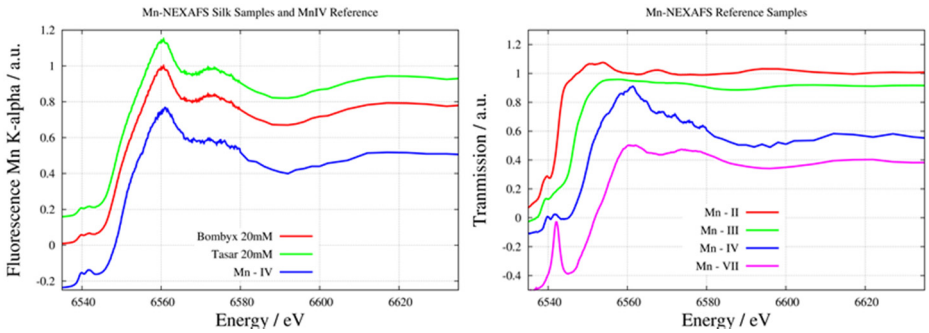

Figure 33.
NEXAFS data measured around the Mn K-edge: measured in transmission and as fluorescence of the Mn K_α emission line. The left panel shows the *Bombyx mori* and Tasar silks overlayed with a commercially available $Mn^{IV}O_2$. The right panel summarises the NEXAFS of commercially available Mn^{II}, Mn^{III}, Mn^{IV}, and Mn^{VII}. Adapted from **Paper 5**.

Chapter 4. Building multifunctionality in silk fiber using supercritical fluid impregnation and sonication

In Chapter 2 and Chapter 3, we demonstrated how each method—supercritical carbon dioxide ($scCO_2$) and sonication—help to develop a novel method to make functional silk hybrid nanomaterials.

In this chapter, we describe that selective processing with the combination of $scCO_2$ and sonication can achieve enhanced conductivity and catalytic efficiency in silk fiber using pyrrole and potassium permanganate ($KMnO_4$). The $scCO_2$ pressure and the pyrrole amount were optimized to maximize the conductivity of the polypyrrole (PPy)-modified silk fiber. Sonication-aided formation of MnO_2 provided catalytic activity to the already conductive fibers. With cyclic voltammetry, we showed that the obtained PPy-MnO_2 silk fibers could be used as a soft working electrode to detect H_2O_2.

Silk fiber from the silkworm *Bombyx mori* consists of chains of biopolymer protein that are strong and lightweight; however, they are not intrinsically conductive [38]. Traditionally, to mass-produce conductive yarns and fibers, the textile industry typically includes metal wires during yarn fabrication [203]. This method often limits the flexibility of the yarns when weaving fabrics and also yields losses in intrinsic textile properties. The bottom-up approach of synthesizing a conductive polymer layer on or into the fibers also has its challenges, namely heterogeneity of the conductive layer, brittleness, low conductivity, low fabrication reproducibility, and a significant decrease in conductivity with time [204-206].

The need exists to develop scalable methods that can yield fibers with good conductivity and yet retain the flexibility needed for fabric weaving or other smart textile applications. $ScCO_2$ impregnation provides such solutions [97, 107-109, 207]. $scCO_2$ aided-impregnation can facilitate and improve the fabrication of conductive silk fibers and textiles [111, 113, 208, 209]. Silk fiber under supercritical condition will swell, and the enhanced diffusivity of molecules will allow conductive monomers (e.g. pyrrole) to be impregnated in the fibers. Upon return to atmospheric conditions, the fibers contract back with the pyrrole monomer organized and ready for a standard oxidative polymerization.

In **Paper 6**, we presented experiments on selective impregnation and deposition methods with $scCO_2$ and sonication to produce conductive and catalytic silk fibers. Also, the experiments showed that using sc-CO_2 enables us to gain dramatically in conductivity from better alignment of the polypyrrole within the silk fibrils.

Characterization of polypyrrole (PPy)-MnO_2 silk

The XRD patterns of the fibers confirmed the presence of birnessite δ-MnO_2 and was verified with JCPDS accession no. 01-073-7861, with characteristic peaks at $2\theta = 36.7°$ and 65.7°. We observed no differences in the MnO_2 peaks between the control and the $scCO_2$ treated fibers. Also, we found no signal or peaks from PPy.

For $scCO_2$-PPy-silk, we could see a mixed pattern with bands of PPy and silk overlapping in the range of 1200–2000 cm^{-1}. Furthermore, for the atm-PPy-silk, the strongly absorbing PPy layer precluded any visible peaks. Similar peaks comparable to pure pyrrole vibrations were observed. We were not able to measure sufficiently strong signals from the silk because of the thick and highly absorbing PPy layer.

Application of $scCO_2$ impregnation to obtain high conductivity

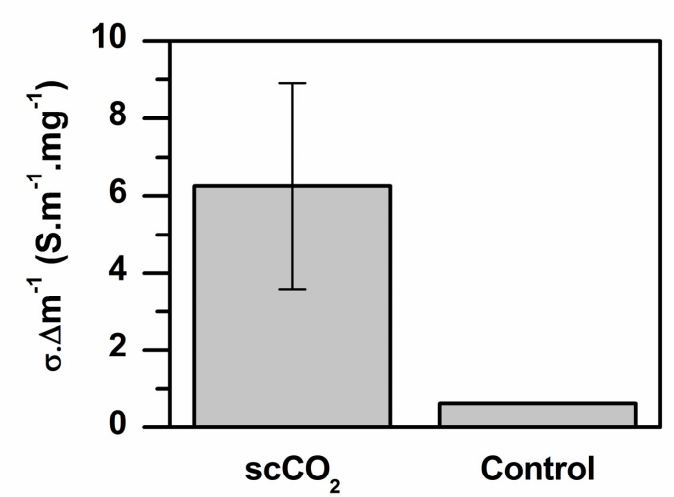

Figure. 34.
Comparison of the conductivity per unit mass of mass gained ($S.m^{-1}.mg^{-1}$) of the $scCO_2$, and atmospheric (control) prepared PPy-silk fiber. The conductivity of $scCO_2$-PPy-silk and atm-PPy-silk were 6.24 ± 2.65 and 0.62 ± 0.02 ($S.m^{-1}.mg^{-1}$), respectively. Adapted from **Paper 6**.

In both treatments, namely $scCO_2$ and atmospheric- (control) assisted, the final color of silk fiber turned completely black. This highlights the formation of PPy on the surface of the silk fibers. As demonstrated in Figure 35, the $scCO_2$-PPy-silk was 10 times more conductive per unit mass gained than the control. The optimal condition to achieve maximum conductivity was determined by varying the pyrrole monomer concentration (5, 10, 25 and 50% vol./vol.) and the $scCO_2$ pressure (0, 50 100 and 200 bars). The normalized conductivity by the mass gained of the $scCO_2$-PPy-silk was measured and calculated for samples prepared for a varying amount of pyrrole (and at a constant CO_2 pressure of 200 bars, Figure 35) and at different supercritical pressures (and at a constant pyrrole monomer amount of 5% vol./vol,). Based on Figure 35, normalized conductivity per unit mass gained of $scCO_2$-PPy-silk fiber was the highest for a pyrrole concentration of 5% vol./vol. at 200 bars. It was also observed that the impregnation of 5% vol./vol. of pyrrole at 100 and 200 bars was not significantly different. However, we progressed with 200 bars as the impregnation pressure to ensure we operated in the supercritical regime instead of the sub-critical. The impregnation time and temperature were 20 min and 40 °C, respectively.

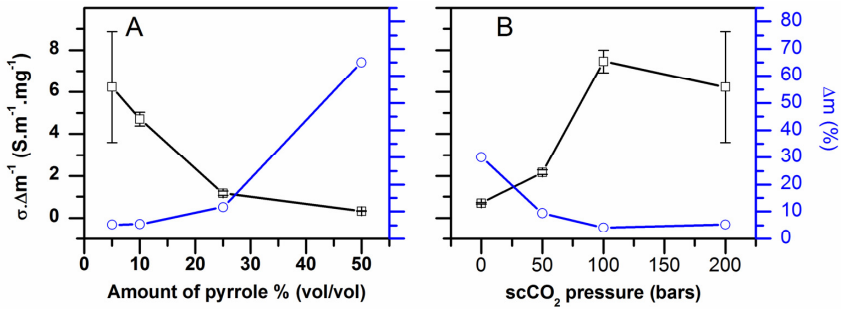

Figure 35.
Effect of different (A) varying amounts of pyrrole (at 200 bars $scCO_2$) and (B) $scCO_2$ pressures at a constant pyrrole monomer volume (5% vol./vol.) on the fiber's conductivity per unit mass gain. Note the mass gained (blue line and circles) is plotted on the right axis of each graph. The conductivity per unit mass gained for the different volumes of pyrrole (5, 10, 25 and 50% vol./vol.) was 6.24 ± 2.65, 4.7 ± 0.33, 1.18 ± 0.1, and 0.33 ± 0.01 ($S.m^{-1}.mg^{-1}$) respectively. The conductivity per unit gained for the different pressures (0, 50 100 and 200 bars) was 0.68 ± 0.04, 2.17 ± 0.1, 7.45 ± 0.53 and 6.24 ± 2.65 ($S.m^{-1}.mg^{-1}$), respectively. Adapted from **Paper 6.**

Enzyme-like polypyrrole (PPy)-MnO_2 silk fiber

Using the sonication method, we synthesized MnO_2 NPs on the PPy-silk fibers. As a result, the fiber acquired some enzyme-like oxidative properties. We found that it can degrade MB and H_2O_2, thus exhibiting oxidase-like activities. Figure 36 shows that the $scCO_2$-PPy-MnO_2 silk was much more effective in the degradation of MB and H_2O_2 compared to atm-PPy-MnO_2 (control).

In **Paper 3**, we showed the enzyme-like behavior of MnO_2-Silk fibers toward the oxidation of the H_2O_2, TMB, OPD substrates. Here, the oxidative properties of the PPy-MnO_2-Silk hybrid showed an enzyme-like behavior for the degradation of H_2O_2 with a Km of about 13 mM and a specific activity of 1470 ± 75 µmol/min/g. The control experiments, on the contrary, showed that the silk and the PPy-silk alone did not cause any disproportionation of H_2O_2 and MB.

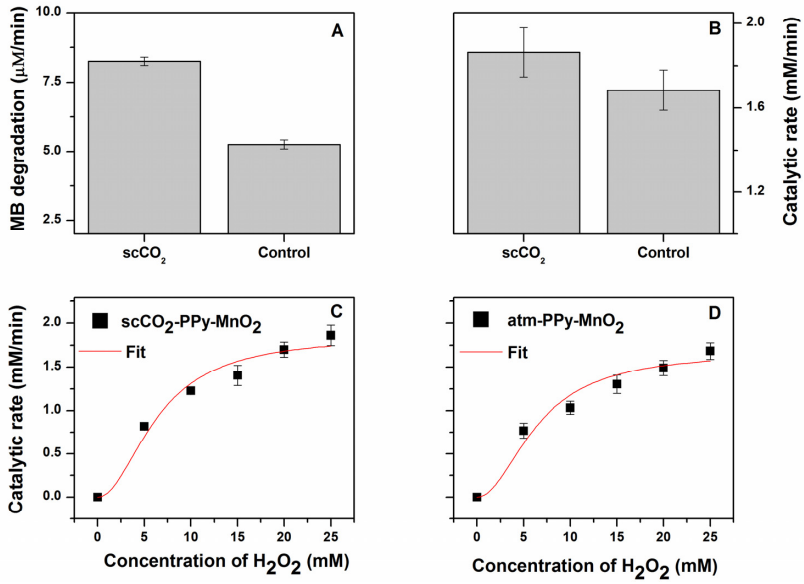

Figure 36.
Comparison of the catalytic activity of PPy-MnO_2 silk fiber with MB (panel A) and H_2O_2 (panel B) as substrates. The rates of MB degradation by scCO_2-PPy-MnO_2 and atm-PPy-MnO_2 (control) silk fibers were 8.3 ± 0.15 and 5.3 ± 0.17 μM/min, respectively. The catalytic rate of degradation of 25 mM H_2O_2 by scCO_2-PPy-MnO_2 and atm-PPy-MnO_2 silk fibers was 1.9 ± 0.11 and 1.7 ± 0.09 mM/min, respectively. Panel C and D show the fit of the Michaelis-Menten model to the catalytic rates as a function of H_2O_2 concentration. We found for scCO_2-PPy-MnO_2 silk a Km of 12.7 ± 2.3 mM and a V_{max} of 2.7 ± 0.22 mM/min (67.5 ± 5.5 μmol/min), and for atm-PPy-MnO_2-silk with a K_m of 12.9 ± 2.76 mM and a V_{max} of 2.48 ± 0.23 mM/min (62 ± 5.75 μmol/min). Adapted from **Paper 6.**

ScCO_2-PPy-MnO_2 silk fiber as a soft working electrode for sensing H_2O_2

PPy-MnO_2 silk fibers were tested to demonstrate the soft working electrode and sensing unit to detect H_2O_2. Figure 37 shows the increase in current for the scCO_2-PPy-MnO_2 silk in the presence of H_2O_2 compared with the same electrode with no H_2O_2 in the solution. This increase in current came from the oxidation of H_2O_2. The control (Figure 37) showed a weak enhancement, and the silk alone showed no responses (Figure 37). Furthermore, scCO_2-PPy-MnO_2 and atm-PPy-MnO_2 showed a decreasing catalytic activity after five cycles. The loss was more pronounced for the atm-PPy-MnO_2 than that for the scCO_2-PPy-MnO_2 silk.

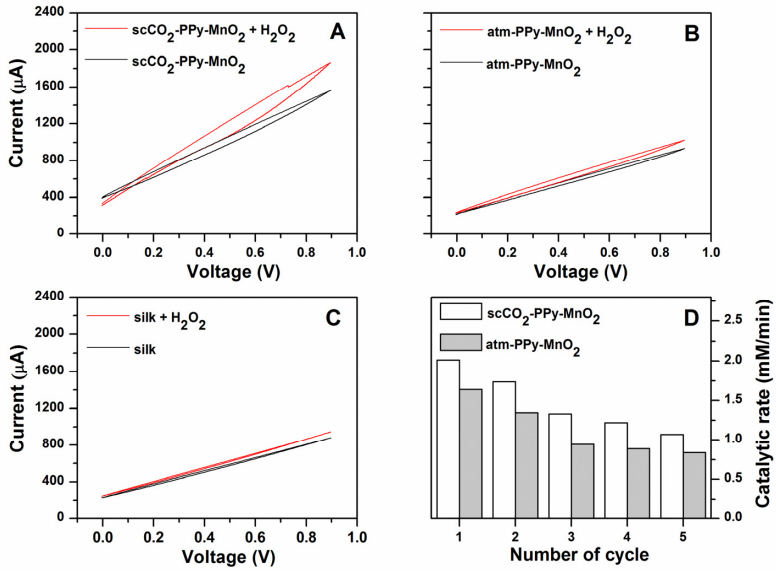

Figure 37.
Cyclic voltammetry measurements of the (A) $scCO_2$-PPy-MnO_2 silk, (B) atm-PPy-MnO_2 silk, and (C) silk (with or without 5 mM H_2O_2 in 50 mM PBS buffer pH 7.4 and a scan rate of 5 mV/s). (D) Operational stability of $scCO_2$-PPy-MnO_2 silk and atm-PPy-MnO_2 silk was tested over five consecutive cycles to degrade H_2O_2. Adapted from **Paper 6.**

Silk fibers show complex structural and chemical composition. Figure 38 summarizes the consensus models of *Bombyx mori* fibers and the steps of impregnation and sonication to manufacture the PPy-MnO_2-silk hybrid. In **Paper 6**, based on experimental evidence, we speculated PPy and MnO_2 were present inside the inter-fibrillar space, while MnO_2 appeared in areas where PPy was not present. This also reflected on the integration of two functionalities without impeding their activities.

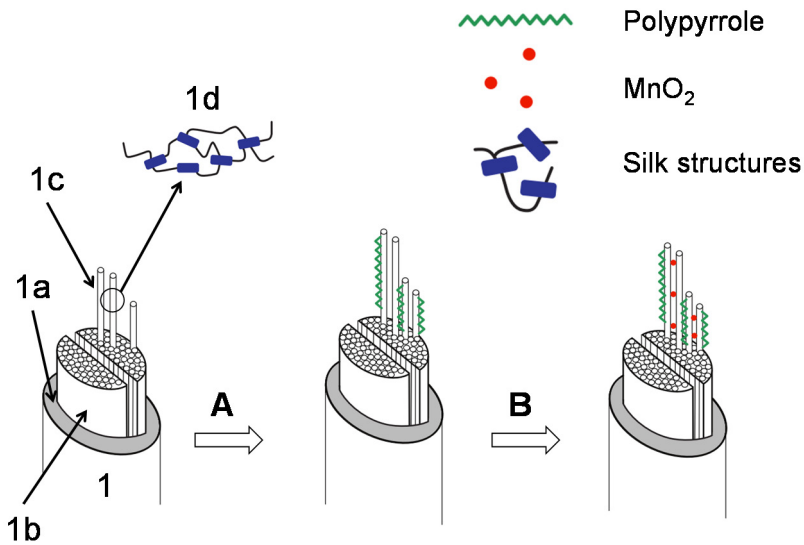

Figure 38.
Illustration of the processes yielding PPy-MnO_2-silk hybrid fiber. (1) Typical morphology of silk fiber, sericin coating (1a), fibroin brins (1b), fibrils (1c), and secondary structures (1d). Step A: $scCO_2$ impregnation and oxidation of pyrrole into PPy. We tentatively locate the PPy in the inter-fibrillar space. Step B: Sonication aided MnO_2 formation. It was adapted from **Paper 6.**

Chapter 5. Conclusion and Future perspective

Conclusion

Extensive applications of reinforced natural polymers with composites have been realized over the last few decades. The discovery of nanoparticles (NPs) in the 1980s created a new surge in the field of silk and textile nanocomposites. The potential of NPs to modify the features of a natural polymer or fiber matrix and enhance their functional properties has been widely explored in the literature. Silk is diverse in form, quality and cost. New properties can be added to silk by functionalizing it with nanoparticles. However, the addition of functionalities gets hampered by the silk's inert surface. Generally, the application of nanotechnology in textile is limited by the difficulties of loading the textile fibers with nanoparticles and, most importantly, by the uncontrolled leakage of the loaded particles.

In this thesis, we reported on the availability of space in silk fibers for the loading of NPs by $scCO_2$ assisted impregnation at low temperatures. The four silks (mulberry, eri, muga and tasar) displayed a remarkable capacity for the size of the Au NPs (up to 150 nm). The detailed study of the impregnation mechanism suggested the presence of a narrow window of process parameters, and no detrimental effect on the fiber structure was observed. The mechanism for impregnating NPs into a solid fiber substrate is yet to be resolved; we hypothesized that the transportation of the NPs was possible because of a surface tension gradient at the liquid–solid interface.

Next, we demonstrated that the MnO_2-Silk fiber obtained by sonochemical reduction of $KMnO_4$ could be successfully used and re-used for the degradation of TMB and OPD substrates. We found by potentiometric titration, one active species that we tentatively identify as $Mn_{1-x}^{4+}Mn_x^{3+}O_{2-x}(OH)_x$. We anticipated a broader application to oxidize a range of dyes structurally similar to the ones tested. The recovery of activity during the recycling process perhaps could be improved, since our findings are based on a low amount of MnO_2-Silk, which in turn might affect the physical recovery of the catalytic fibers. We explained our results by the ability of silk internal structures and chemistry to stabilize the MnO_2 reactive species and allow true catalytic activity.

Further, the *in-situ* method confirms that silk is playing a significant role in the reduction of $KMnO_4$ to MnO_2 NPs with the help of sonication. Overall, the work explains that sonication helps in forming smaller size, better dispersion of MnO_2 particles on the silk surface and deeper; thus, the formed MnO_2 NPs can have better interaction with the amino acid chain in the fibroin protein, in turn making them more stable. Our results have implications on the understanding of the catalytic origin and interaction of metal oxides NP with various biomaterials, especially of polypeptides and structural proteins.

Further, bi-functional polypyrrole (PPy)-MnO_2 *Bombyx mori* silk fibers were successfully prepared and used as soft bio-like sensors to detect and degrade H_2O_2. The use of $scCO_2$ and sonication enabled the integration of the two functionalities without lowering their activities. The exact mechanism for the impregnation of monomers and the location and distribution of PPy and MnO_2 is not precise. Nevertheless, experimental outcomes have led to speculations about the inter-fibrillar space and amorphous region within the silk fibers. The selective building of functionalities without compromises may have dramatic implications for how we design and think about the next generation of hybrid materials.

Future perspective

The field of polymer-based composites and nanocomposites is growing rapidly and widely. This thesis study on silk-based composite hybrid materials can be seen as a significant contribution to the silk-based hybrid material field. It also enables the envisioning of a large number of future studies. It is crucial to make stable nanoparticles (NPs) without any leakage on silk fiber in order to completely use the gained functionalities. However, the location specificity of the gold nanoparticles (Au NPs) with respect to their sizes in the silk matrix is still not clear. Hence, further morphological studies need to be carried out to thoroughly understand the structure of the composites with the impregnation of different sizes of NPs.

Further, the mechanism of impregnating the NPs under supercritical conditions is still highly precise, and the role of the muga fiber with high Au NP loading potential up to 50 nm for control impregnation is still not apparent. Therefore, further research on ternary systems comprising of "$scCO_2$ + non-soluble NPs + fibers (solid substrates)" is required for a detailed understanding of the mass transfer and diffusion processes in the substrate and their influences on the properties of the bulk material, such as crystallinity, morphology, anisotropy and reactivity.

For MnO_2-Silk, the operational test with the TMB and OPD substrate shows the constant rates observed with increasing cycle numbers. Therefore, from a

sustainability point of view, we were able to transform typically stoichiometric manganese oxides into catalytic manganese oxides for the degradation of TMB, and OPD substrate. However, it is still not clear, how are the silk fibers stabilizing the MnO_2? Hence, more work is required to understand the role of silk fiber in stabilizing NPs.

We suggested that the PPy could be loaded within the silk inter-fibrillar network. Still, the depth of the PPy in the fibers and thickness of the PPy layers need to be worked out. Hence, morphological studies on the cross-sectional images of the fibers need to be conducted. Further, it would help improve the understanding of the conductive difference between $scCO_2$ and fibers treated in atmospheric conditions. The results obtained from building the catalytic and conductive silk fibers may have significant implications on how we design the next generation of hybrid materials. With a better understanding of the silk template for different functionalities, we can now begin questioning how many more functionalities can be added to silk fibers and how applicable the methods would be for various materials. For example, functional metal/metal-oxides NPs such as FeO_x, Ag NPs, ZnO, CuO, CeO_x can be added to the conductive and catalytic silk fiber by utilizing oxidative, adsorptive properties of MnO_2 and templating properties of silk fiber. Therefore, it should be possible to manufacture conductive and catalytic silk fiber with more functionalities and broaden the scope of applications.

Acknowledgments

I am grateful for this opportunity to pursue my interest. This journey is nothing less than a dream come true, and I would like to thank everyone who has contributed to my learning curve and supported me through these years.

I would like to thank Cedric Dicko for his faith in me. He is an open-minded person, and I enjoyed working with him. During my initial Ph.D. years, he was instrumental in highlighting the importance of a critical and ethical research mindset. He has profound knowledge about the field, which led to great discussions during the course of my research. He has been incredibly patient in answering all my questions, and he always encouraged me to make mistakes. Under his supervision, we had a great collaboration with researchers at PTB Berlin and within Lund University. This opportunity was a critical step in my research, and we obtained some fantastic results together.

I am also thankful for the constant encouragement and everlasting support towards my research offered by my second supervisor, Estra Dey. Moreover, I can never forget the tasty Swedish kanelbullar and chocolate, which she always got for me. She is an approachable supervisor and made me feel comfortable in the lab. She always listened to my problems or dilemmas and motivated me to believe in myself.

I would like to thank Leif Bülow, who helped me deal with the administrative chores. I am thankful for his support during my moments of self-doubt in my journey. My thanks to Lei-Ye for allowing me to teach his course lab and supporting me to develop new skills and gain expertise, by teaching students.

I would also like to thank Karin and Alfia for helping me teach protein purification during the course lab. You both have been patient and kind in helping me understand the process from scratch.

To all the previous group members—Alix, Kishan, Mathias, Chris, Egle, Marc, Alessandra, Shruti, Marion and Charlotte—I offer my thanks for all our collaboration, good fun, loud laughs and out-of-office times. To my current group members, Milena, Bettina and Rodrigo, thank you for the healthy and knowledgeable group discussions and sharing of innovative project ideas.

I especially want to thank my collaborators Lo Gorton, Paolo Bollella, Raul Garcia, Michael and Christian for their cooperation and time on this research idea. This would be incomplete without you all.

I also want to thank Johan, Per-Olof, Nelida and Lieselotte Po, who have been greatly supportive of my research and always taught me something new based on their learnings in their respective research areas. From identifying the right journal to highlighting the importance of critical thinking, you have been incredibly encouraging.

Lastly, I want to thank my wife Snigdha and my family back home in India, for being my constant rock through thick and thin. This journey cannot be completed without their blessings and love.

References

1. Schindler, W.D. and P.J. Hauser, *Chemical finishing of textiles*.
2. Roy Choudhury, A. K., *Environmental impacts of the textile industry and its assessment through life cycle assessment*, in *Roadmap to Sustainable Textiles and Clothing: Environmental and Social Aspects of Textiles and Clothing Supply Chain*, S. S. Muthu, Editor. 2014, Springer Singapore: Singapore. p. 1–39.
3. *Introduction to textiles and the environment*, in *Textiles and Clothing*. p. 1–9.
4. Nayak, R., T. Panwar, and L.V.T. Nguyen, *1 - Sustainability in fashion and textiles: A survey from developing country*, in *Sustainable Technologies for Fashion and Textiles*, R. Nayak, Editor. 2020, Woodhead Publishing. p. 3-30.
5. Nayak, R., et al., *RFID in textile and clothing manufacturing: technology and challenges.* Fashion and Textiles, 2015. **2**(1): p. 9.
6. Journal, I. and T. Technology, *No Title.* 2008. **1**(5): p. 1-10.
7. Landoge, S.M., A.I. Wasif, and S.R. Parihar, *Application of nanotechnology in high performance textiless.* Textile Asia, 2014. **45**(8): p. 40-43.
8. Patra, J.K. and S. Gouda, *Application of nanotechnology in textile engineering : An overview.* 2013. **5**(June): p. 104-111.
9. Shabbir, M. and F. Mohammad, *Insights into the functional finishing of textile materials using nanotechnology.* 2017: p. 97–115.
10. Joshi, M. and A. Bhattacharyya, *Nanotechnology – A new route to high-performance functional textiles.* 2011. **5167**.
11. Yetisen, A. K., et al., *Nanotechnology in textiles.* ACS Nano, 2016. **10**(3): p. 3042–3068.
12. Siegfried, B., *NanoTextiles : Functions , nanoparticles and commercial applications.* 2007(December).
13. Manea, F., et al., *Nanozymes: Gold-nanoparticle-based transphosphorylation catalysts.* 2004: p. 6165–6169.
14. Ramaratnam, K., et al., *Ultrahydrophobic textiles: Lotus approach.* AATCC Review, 2008. **8**(1): p. 42-48.
15. Petra, A., et al., *Use of Nanomaterials in Textiles 1 Application description.* Fact Sheet Nano Products, 2013. **1**: p. 1-9.

16. Bhattacharya, M., *Polymer nanocomposites-A comparison between carbon nanotubes, graphene, and clay as nanofillers.* Materials, 2016. **9**(4): p. 1-35.
17. Zhao, X., et al., *Polymer-supported nanocomposites for environmental application: A review.* Chem. Eng. J., 2011. **170**(2-3): p. 381-394.
18. Saba, N., P.M. Tahir, and M. Jawaid, *A review on potentiality of nano filler/natural fiber filled polymer hybrid composites.* Polymers, 2014. **6**(8): p. 2247-2273.
19. Alongi, J., F. Carosio, and G. Malucelli, *Current emerging techniques to impart flame retardancy to fabrics: An overview.* Polymer Degradation and Stability, 2014. **106**: p. 138-149.
20. Dong, B. H. and J. P. Hinestroza, *Metal nanoparticles on natural cellulose fibers: Electrostatic assembly and in situ synthesis.* ACS Applied Materials & Interfaces, 2009. **1**(4): p. 797–803.
21. Onar, N., et al., *Antimicrobial, UV-protective and self-cleaning properties of cotton fabrics coated by dip-coating and solvothermal coating methods.* Fibers and Polymers, 2011. **12**(4): p. 461-470.
22. Li, G., et al., *Chemical assembly of TiO_2 and TiO_2@Ag nanoparticles on silk fiber to produce multifunctional fabrics.* J. Colloid Interface Sci., 2011. **358**(1): p. 307-315.
23. Shateri-Khalilabad, M., M.E. Yazdanshenas, and A. Etemadifar, *Fabricating multifunctional silver nanoparticles-coated cotton fabric.* Arab. J. Chem., 2017. **10**(0).
24. Tang, B., et al., *In-situ synthesis of gold nanoparticles for multifunctionalization of silk fabrics.* Dyes and Pigm., 2014. **103**: p. 183-190.
25. Tang, B., et al., *Colorful and antibacterial silk fiber from anisotropic silver nanoparticles.* Ind. Eng. Chem. Res., 2013. **52**(12): p. 4556–4563.
26. Park, J.-E., M. Atobe, and T. Fuchigami, *Sonochemical synthesis of conducting polymer–metal nanoparticles nanocomposite.* Electrochim. Acta, 2005. **51**(5): p. 849-854.
27. Abate, M. T., A. Ferri, and J. Guan, *We are IntechOpen, the world's leading publisher of open access books built by scientists, for scientists top 1% Supercritical CO_2 to impart.*
28. Mitrano, D. M., et al., *Presence of nanoparticles in wash water from conventional silver and nano-silver textiles.* ACS Nano, 2014. **8**(7): p. 7208–7219.
29. Hristozov, D. and I. Malsch, *Hazards and risks of engineered nanoparticles for the environment and human health.* Sustainability, 2009. **1**: p. 1161-1194.
30. Altman, G.H., et al., *Silk-based biomaterials.* Biomaterials, 2003. **24**(3): p. 401-416.

31. Davarpanah, S., et al., *Environmentally friendly surface modification of silk fiber: Chitosan grafting and dyeing.* Applied Surface Science, 2009. **255**(7): p. 4171-4176.
32. Hashimoto, T., et al., *Changes in the properties and protein structure of silk fibroin molecules in autoclaved fabrics.* Polymer Degradation and Stability, 2015. **112**: p. 20-26.
33. Zhong, J., et al., *Self-assembly of regenerated silk fibroin from random coil nanostructures to antiparallel β-sheet nanostructures.* Biopolymers, 2014. **101**(12): p. 1181-1192.
34. Volkov, V., A. V. Ferreira, and A. Cavaco-Paulo, *On the routines of wild-type silk fibroin processing toward silk-inspired materials: A review.* Macromolecular Materials and Engineering, 2015. **300**(12): p. 1199–1216.
35. Tao, H., D. L. Kaplan, and F. G. Omenetto, *Silk Materials – A road to sustainable high technology.* Advanced Materials, 2012. **24**(21): p. 2824–2837.
36. Koh, L.D., et al., *Structures, mechanical properties and applications of silk fibroin materials.* Progress in Polymer Science, 2015. **46**: p. 86-110.
37. Zhao, H.-P., X.-Q. Feng, and H.-J. Shi, *Variability in mechanical properties of Bombyx mori silk.* Materials Science and Engineering: C, 2007. **27**(4): p. 675-683.
38. Rockwood, D.N., et al., *Materials fabrication from Bombyx mori silk fibroin.* Nature Protocols, 2011. **6**(10): p. 1612-1631.
39. Shao, Z. and F. Vollrath, *Surprising strength of silkworm silk.* Nature, 2002. **418**(6899): p. 741-741.
40. Qi, Y., et al., *A Review of structure construction of silk fibroin biomaterials from single structures to multi-level structures.* International Journal of Molecular Sciences, 2017. **18**(3): p. 237.
41. Numata, K., P. Cebe, and D.L. Kaplan, *Mechanism of enzymatic degradation of beta-sheet crystals.* Biomaterials, 2010. **31**(10): p. 2926-2933.
42. Valluzzi, R., et al., *Orientation of silk III at the air-water interface.* International Journal of Biological Macromolecules, 1999. **24**(2): p. 237-242.
43. Marin, M.A., R.R. Mallepally, and M.A. McHugh, *Silk fibroin aerogels for drug delivery applications.* J. Supercrit. Fluids, 2014. **91**: p. 84-89.
44. Melke, J., et al., *Silk fibroin as biomaterial for bone tissue engineering.* Acta Biomaterialia, 2016. **31**: p. 1-16.
45. Mazzi, S., et al., *Comparative thermal analysis of Eri, Mori, Muga, and Tussar silk cocoons and fibroin fibers.* J. Therm. Anal. Calorim., 2014. **116**(3): p. 1337-1343.

46. Gupta, V.B., R. Rajkhowa, and V.K. Kothari, *Physical characteristics and structure of Indian silk fibres.* Indian Journal of Fibre and Textile Research, 2000. **25**(1): p. 14-19.
47. Sen, K. and M. K. Babu, *Studies on Indian silk. II. Structure–property correlations.* J. Appl. Polym. Sci., 2004. **92**: p. 1098–1115.
48. Sen, K., M.K. Babu, and K.M. Babu, *Studies on Indian silk. III. Effect of structure on dyeing behavior.* J. Appl. Polym. Sci., 2004. **92**: p. 1116-1123.
49. Sen, K. and M.B. K, *Studies on Indian Silk . I . Macrocharacterization and Analysis of Amino Acid Composition.* Polymer, 2003.
50. Guan, J., et al., *Glass transitions in native silk fibres studied by dynamic mechanical thermal analysis.* Soft Matter, 2016. **12**(27): p. 5926-5936.
51. Khanjani, S., A. Morsali, and S.W. Joo, *In situ formation deposited ZnO nanoparticles on silk fabrics under ultrasound irradiation.* Ultrasonics Sonochemistry, 2013. **20**(2): p. 734-739.
52. Xu, S., et al., *Fabrication of hierarchical structured Fe_3O_4 and Ag nanoparticles dual-coated silk fibers through electrostatic self-assembly.* Materials Letters, 2016. **164**: p. 274-277.
53. Khanjani, S. and A. Morsali, *Ultrasound-assisted coating of silk yarn with sphere-like Mn3O4 nanoparticles.* Ultrasonics Sonochemistry, 2013. **20**(1): p. 413-417.
54. Singh, M., et al., *Conductive and enzyme-like silk fibers for soft sensing application.* Biosensors and Bioelectronics, 2019: p. 111859.
55. Hu, X., J. Li, and Y. Bai, *Fabrication of high strength graphene/regenerated silk fibroin composite fibers by wet spinning.* Materials Letters, 2017. **194**: p. 224-226.
56. Song, J., et al., *Treatise Fabrication of hierarchical structured graphene oxide-Fe_3O_4 hybrid nanosheets and Ag nanoparticles bimetallic composite coated silk fibers through self-assembly.* 2017: p. 59-68.
57. Wang, J.-T., et al., *Directly obtaining high strength silk fiber from silkworm by feeding carbon nanotubes.* Materials science & engineering. C, Materials for biological applications, 2014. **34**: p. 417-421.
58. Wang, J.-T., et al., *Directly obtaining pristine magnetic silk fibers from silkworm.* International Journal of Biological Macromolecules, 2014. **63**: p. 205-209.
59. Wang, Q., et al., *Feeding single-walled carbon nanotubes or graphene to silkworms for reinforced silk fibers.* Nano Letters, 2016. **16**(10): p. 6695–6700.
60. Jin, H.-J., et al., *Human bone marrow stromal cell responses on electrospun silk fibroin mats.* Biomaterials, 2004. **25**(6): p. 1039-1047.

61. Sun, M., et al., *The structure–property relationships of artificial silk fabricated by dry-spinning process.* Journal of Materials Chemistry, 2012. **22**(35): p. 18372-18379.
62. Matsumoto, K., et al., *Studies on regenerated protein fibers. III. Production of regenerated silk fibroin fiber by the self-dialyzing wet spinning method.* Journal of Applied Polymer Science, 1996. **60**(4): p. 503-511.
63. Ke, J., et al., *Size-Dependent Uptake and Distribution of AgNPs by Silkworms.* ACS Sustainable Chemistry & Engineering, 2020. **8**(1): p. 460-468.
64. Cao, J. and C. Wang, *Multifunctional surface modification of silk fabric via graphene oxide repeatedly coating and chemical reduction method.* Applied Surface Science, 2017. **405**: p. 380-388.
65. Shaabani, A., Z. Hezarkhani, and E. Badali, *Natural silk supported manganese dioxide nanostructures: Synthesis and catalytic activity in aerobic oxidation and one-pot tandem oxidative synthesis of organic compounds.* Polyhedron, 2016. **107**: p. 176-182.
66. Xia, Y., J. Wan, and Q. Gu, *Silk fibroin fibers supported with high density of gold nanoparticles: Fabrication and application as catalyst.* Gold Bulletin, 2011. **44**(3): p. 171-176.
67. Peng, L., et al., *Silver nanoparticles coating on silk fabric with pretreatment of 3-aminopropyltrimethoxysilane in supercritical carbon dioxide.* Journal of Industrial Textiles, 2016. **47**(5): p. 883-896.
68. Rockwood, D.N., et al., *Materials fabrication from Bombyx mori silk fibroin.* Nature Protocols, 2011. **6**: p. 1612.
69. Toytziaridis, A. and C. Dicko, *Fabrication and Optimization of Stable, Optically Transparent, and Reusable pH-Responsive Silk Membranes.* International Journal of Molecular Sciences, 2016. **17**(11): p. 1897.
70. Menges, F. https://www.effemm2.de/spectragryph/about.html.
71. Noda, I. and Y. Ozaki, *Two-dimensional correlation spectroscopy. Applications in vibrational and optical spectroscopy*. 2005, Chichester: John Wiley & Sons, Ltd.
72. Brassard, P., J.R. Kramer, and P.V. Collins, *Binding site analysis using linear programming.* Environ. Sci. Technol., 1990. **24**: p. 195-201.
73. Davies, C.W., *Ion Association*. 1962, Washington: Butterworths. 190.
74. Cox, J.S., et al., *Characterizing heterogeneous bacterial surface functional groups using discrete affinity spectra for proton binding.* Environ. Sci. Technol., 1999. **33**: p. 4514-4521.
75. Westall, J.C., *FITEQL: a computer program for the determinationof chemical equilibrium constants from experimental data*. 1982.

76. Turner, B.F. and J.B. Fein, *Protofit: A program for determining surface protonation constants from titration data.* Computers and Geosciences, 2006. **32**(9): p. 1344-1356.
77. Henry, E.R. and J. Hofrichter, *[8] Singular value decomposition: Application to analysis of experimental data*, in *Methods in Enzymology*. 1992, Academic Press. p. 129-192.
78. Wentzell, P.D., et al., *Multivariate curve resolution of time course microarray data.* BMC Bioinformatics, 2006. **7**(1): p. 343.
79. Windig, W. and J. Guilment, *Interactive self-modeling mixture analysis.* Analytical Chemistry, 1991. **63**(14): p. 1425-1432.
80. Windig, W., et al., *A new approach for interactive self-modeling mixture analysis.* Chemometrics and Intelligent Laboratory Systems, 2005. **77**: p. 85-96.
81. Gleber, G., et al., *Traceable size determination of PMMA nanoparticles based on Small Angle X-ray Scattering (SAXS).* J Phys Conf Ser, 2010. **247**: p. 12027-12027.
82. Krumrey, M. and G. Ulm, *High-accuracy detector calibration at the PTB four-crystal monochromator beamline.* Nucl Instrum Meth A, 2001. **467-468**: p. 1175-1178.
83. Garcia-Diez, R., C. Gollwitzer, and M. Krumrey, *Nanoparticle characterization by continuous contrast variation in small-angle X-ray scattering with a solvent density gradient.* J Appl Crystallogr, 2015. **48**: p. 20-28.
84. Wernecke, J., et al., *Characterization of an in-vacuum PILATUS 1M detector.* J Synchrotron Radiat, 2014. **21**: p. 529-536.
85. Krumrey, M., et al., *Synchrotron radiation-based x-ray reflection and scattering techniques for dimensional nanometrology.* Meas Sci Technol, 2011. **22**: p. 94032-94032.
86. Ballauff, M. and A. Jusufi, *Anomalous small-angle X-ray scattering: analyzing correlations and fluctuations in polyelectrolytes.* Colloid and Polymer Science, 2006. **284**(11): p. 1303-1311.
87. Ingham, B., et al., *Elemental fingerprinting of mineral species in iron-fortified milk: anomalous small-angle X-ray scattering and resonant soft X-ray scattering studies.* Journal of Synchrotron Radiation, 2018. **25**(4): p. 1106-1112.
88. Henke, B.L., E.M. Gullikson, and J.C. Davis, *X-Ray Interactions: Photoabsorption, Scattering, Transmission, and Reflection at E = 50-30,000 eV, Z = 1-92.* Atomic Data and Nuclear Data Tables, 1993. **54**(2): p. 181-342.
89. Stuhrmann, H.B., *Contrast variation in X-ray and neutron scattering.* J. Appl. Cryst., 2007. **40**: p. s23--s27.

90. Vogtt, K., et al., *Anomalous small-angle x-ray scattering from mesoporous noble metal catalysts.* Colloid and Polymer Science, 2013. **291**(9): p. 2163-2171.
91. Yu, C., et al., *Size and composition distribution dynamics of alloy nanoparticle electrocatalysts probed by anomalous small angle X-ray scattering (ASAXS).* Faraday Discussions, 2009. **140**(0): p. 283-296.
92. Jeng, U.-S., et al., *Anomalous small- and wide-angle X-ray scattering and X-ray absorption spectroscopy for Pt and Pt-Ru nanoparticles.* Journal of Applied Crystallography, 2007. **40**(s1): p. s418-s422.
93. Brumberger, H., et al., *In situ anomalous small-angle X-ray scattering from metal particles in supported-metal catalysts. II. Results.* Journal of Applied Crystallography, 2005. **38**(2): p. 324-332.
94. Pirkkalainen, K., et al., *Structure of nickel nanoparticles in a microcrystalline cellulose matrix studied using anomalous small-angle X-ray scattering.* J Appl Crystallogr, 2007. **40**(Suppl. 1): p. s489-s494.
95. Vainio, U., et al., *Copper and copper oxide nanoparticles in a cellulose support studied using anomalous small-angle X-ray scattering.* European Physical Journal D, 2007. **42**(1): p. 93-101.
96. Brunner, G., *J. Supercrit. Fluids.* Annual Review of Chemical and Biomolecular Enginering, 2010. **1**: p. 321-342.
97. Gittard, S.D., et al., *Antifungal Textiles Formed Using Silver Deposition in Supercritical Carbon Dioxide.* J. Mater. Eng. Perform., 2009. **19**(3): p. 368-373.
98. Zhang, X., S. Heinonen, and E. Levänen, *Applications of supercritical carbon dioxide in materials processing and synthesis.* RSC Adv., 2014. **4**(105): p. 61137-61152.
99. Jiang, N., et al., *Carbon-Doped Metal Oxide Nanoparticles Prepared from Metal Nitrates in Supercritical CO2-Enabled Polymer Nanoreactors.* Particle & Particle Systems Characterization, 2019. **36**(9): p. 1900016.
100. Xu, Y., V. Musumeci, and C. Aymonier, *Chemistry in supercritical fluids for the synthesis of metal nanomaterials.* Reaction Chemistry & Engineering, 2019.
101. Lane, M.K.M. and J.B. Zimmerman, *Controlling metal oxide nanoparticle size and shape with supercritical fluid synthesis.* Green Chemistry, 2019. **21**(14): p. 3769-3781.
102. Cansell, F. and C. Aymonier, *Design of functional nanostructured materials using supercritical fluids.* Journal of Supercritical Fluids, 2009. **47**(3): p. 508-516.
103. Champeau, M., et al., *Drug loading of polymer implants by supercritical CO_2 assisted impregnation: A review.* Journal of Controlled Release, 2009. **209**: p. 248-259.

104. van der Kraan, M., et al., *Dyeing of natural and synthetic textiles in supercritical carbon dioxide with disperse reactive dyes.* J. Supercrit. Fluids, 2007. **40**(3): p. 470-476.
105. Fernandez Cid, M.V., et al., *Excellent dye fixation on cotton dyed in supercritical carbon dioxide using fluorotriazine reactive dyes.* Green Chemistry, 2005. **7**(8): p. 609-616.
106. Iheozor-Ejiofor, P. and E.S. Dey, *Extraction of rosavin from Rhodiola rosea root using supercritical carbon dioxide with water.* Journal of Supercritical Fluids, 2009. **50**(1): p. 29-32.
107. Weidner, E., *Impregnation via supercritical CO_2 - What we know and what we need to know.* J. Supercrit. Fluids, 2018. **134**: p. 220-227.
108. Kazarian, S.G., *Polymer processing with supercritical fluids.* Polym. Sci., 2000. **42**(1): p. 78-101.
109. Cooper, A.I., *Polymer synthesis and processing using supercritical carbon dioxide.* Journal of Materials Chemistry, 2000. **10**(2): p. 207-234.
110. Watkins, J.J. and T.J. McCarthy, *Polymer/Metal nanocomposite synthesis in supercritical CO_2.* Chem. Mater., 1995. **7**(11): p. 1991-1994.
111. Erkey, C., *Supercritical carbon dioxide extraction of metals from aqeous solutions: a review.* Journal of Supercritical Fluids, 2000. **17**: p. 259-265.
112. Wakayama, H. and Y. Fukushima, *Supercritical CO_2 for Making Nanoscale Materials.* Industrial & Engineering Chemistry Research, 2006. **45**(10): p. 3328-3331.
113. Kikic, I. and F. Vecchione, *Supercritical impregnation of polymers.* Current Opinion in Solid State and Materials Science, 2003. **7**(4-5): p. 399-405.
114. Zhang, Y., et al., *Supported platinum nanoparticles by supercritical deposition.* Ind. Eng. Chem. Res., 2005. **44**(11): p. 4161-4164.
115. Yu, Q., et al., *Synthesis of cellulose/titanium dioxide hybrids in supercritical carbon dioxide.* Green Chem., 2008. **10**(10): p. 1061-1061.
116. Alongi, J. and G. Malucelli, *Cotton flame retardancy: state of the art and future perspectives.* RSC Advances, 2015. **5**(31): p. 24239-24263.
117. Rastogi, A., et al., *Impact of Metal and Metal Oxide Nanoparticles on Plant: A Critical Review.* Frontiers in Chemistry, 2017. **5**(78).
118. Chih, Y.-W. and W.-T. Cheng, *Supercritical carbon dioxide-assisted synthesis of silver nano-particles in polyol process.* Materials Science and Engineering: B, 2007. **145**(1): p. 67-75.
119. Parandhaman, T., M.D. Dey, and S.K. Das, *Biofabrication of supported metal nanoparticles: exploring the bioinspiration strategy to mitigate the environmental challenges.* Green Chemistry, 2019. **21**(20): p. 5469-5500.
120. Hua, M. and X. Hua, *Polymer nanoparticles prepared by supercritical carbon dioxide for in vivo anti-cancer drug delivery.* Nano-Micro Letters, 2014. **6**(1): p. 20-23.

121. Wang, Y., R.N. Dave, and R. Pfeffer, *Polymer coating/encapsulation of nanoparticles using a supercritical anti-solvent process.* The Journal of Supercritical Fluids, 2004. **28**(1): p. 85-99.
122. Liu, Z.-T., et al., *Supercritical CO_2 Dyeing of Ramie Fiber with Disperse Dye.* Industrial & Engineering Chemistry Research, 2006. **45**(26): p. 8932-8938.
123. Guney, O. and A. Akgerman, *Synthesis of controlled-release products in supercritical medium.* AIChE Journal, 2002. **48**(4): p. 856-866.
124. Said-Galiyev, E., et al., *New Chelate Complexes of Copper and Iron: Synthesis and Impregnation into a Polymer Matrix from Solution in Supercritical Carbon Dioxide.* Industrial & Engineering Chemistry Research, 2000. **39**(12): p. 4891-4896.
125. Fan, Y., et al., *Synthesis of a Novel Disperse Reactive Dye Involving a Versatile Bridge Group for the Sustainable Coloration of Natural Fibers in Supercritical Carbon Dioxide.* Advanced Science, 2019. **6**(1): p. 1801368.
126. Peng, Q., et al., *Grafting of methyl methacrylate onto Antheraea pernyi silk fiber with the assistance of supercritical CO_2.* J. Appl. Polym. Sci., 2006. **100**(2): p. 1299-1305.
127. Poinern, E., *Gold nanoparticle treated textile-based materials for potential use as wearable Sensors.* International Journal of Sciences, 2016. **5**: p. 82-89.
128. Tang, B., et al., *In-situ synthesis of gold nanoparticles for multifunctionalization of silk fabrics.* Dyes and Pigments, 2014. **103**: p. 183–190.
129. Liu, J., et al., *Surface enhanced Raman scattering (SERS) fabrics for trace analysis.* Applied Surface Science, 2016. **386**: p. 296-302.
130. Hu, X., D. Kaplan, and P. Cebe, *Determining Beta-Sheet Crystallinity in Fibrous Proteins by Thermal Analysis and Infrared Spectroscopy.* Macromolecules, 2006. **39**(18): p. 6161-6170.
131. Park, H., et al., *Effect of temperature and pressure on surface tension of polystyrene in supercritical carbon dioxide.* J. Phys. Chem. B, 2007. **111**: p. 3859-3868.
132. Rengasamy, R.S., *Wetting phenomena in fibrous materials*, in *Thermal and moisture transport in fibrous materials*, N. Pan and P. Gibson, Editors. 2006, Woodhead.
133. Lin, Y., J. Ren, and X. Qu, *Catalytically active nanomaterials : A promising candidate for artificial enzymes*.Acc. Chem. Res. 2014. **47** (4): p. 1097-1105.
134. Wei, H. and E. Wang, *Nanomaterials with enzyme-like characteristics (nanozymes): next-generation artificial enzymes.* Chemical Society reviews, 2013. **42**(14): p. 6060-93.

135. Ragg, R., M.N. Tahir, and W. Tremel, *Solids Go Bio: Inorganic Nanoparticles as Enzyme Mimics.* European Journal of Inorganic Chemistry, 2016. **2016**(13-14): p. 1906-1915.
136. Gao, L., et al., *Intrinsic peroxidase-like activity of ferromagnetic nanoparticles.* Nature Nanotechnology, 2007. **2**(9): p. 577-583.
137. Fan, J., et al., *Direct evidence for catalase and peroxidase activities of ferritin-platinum nanoparticles.* Biomaterials, 2011. **32**(6): p. 1611-1618.
138. Wei, H. and E. Wang, *Fe_3O_4 Magnetic Nanoparticles as Peroxidase Mimetics and Their Applications in H2O2 and Glucose Detection.* Analytical Chemistry, 2008. **80**(6): p. 2250-2254.
139. Liu, X., et al., *BSA-templated MnO_2 nanoparticles as both peroxidase and oxidase mimics.* Analyst, 2012. **137**(19): p. 4552-4558.
140. André, R., et al., *V_2O_5 Nanowires with an intrinsic peroxidase-like Activity.* Advanced Functional Materials, 2011. **21**(3): p. 501-509.
141. Pollack, R.M., *From Enzyme Models to Model Enzymes.* Journal of the American Chemical Society, 2010. **132**(10): p. 3637-3637.
142. Wu, J., et al., *Nanomaterials with enzyme-like characteristics (nanozymes): next-generation artificial enzymes (II).* Chemical Society Reviews, 2019. **48**(4): p. 1004-1076.
143. Astruc, D., F. Lu, and J.R. Aranzaes, *Nanoparticles as Recyclable Catalysts: The Frontier between Homogeneous and Heterogeneous Catalysis.* Angewandte Chemie International Edition, 2005. **44**(48): p. 7852-7872.
144. Deng, H., et al., *Nanoparticulate peroxidase/catalase mimetic and its application.* Chemistry - A European Journal, 2012. **18**(29): p. 8906-8911.
145. Pirmohamed, T., et al., *Nanoceria exhibit redox state-dependent catalase mimetic activity.* Chemical communications (Cambridge, England), 2010. **46**(16): p. 2736-2738.
146. Song, Y., et al., *Label-Free Colorimetric Detection of Single Nucleotide Polymorphism by Using Single-Walled Carbon Nanotube Intrinsic Peroxidase-Like Activity.* Chemistry – A European Journal, 2010. **16**(12): p. 3617-3621.
147. Garg, B. and T. Bisht, *Carbon nanodots as peroxidase nanozymes for Biosensing.* Molecules, 2016. **21**(12): p. 1653-1653.
148. Song, Y., et al., *Graphene oxide: Intrinsic peroxidase catalytic activity and its application to glucose detection.* Advanced Materials, 2010. **22**(19): p. 2206-2210.
149. Tao, Y., et al., *Self-assembled, functionalized graphene and DNA as a universal platform for colorimetric assays.* Biomaterials, 2013. **34**(20): p. 4810-4817.

150. Asati, A., et al., *Oxidase-Like activity of polymer-coated cerium oxide nanoparticles.* Angewandte Chemie International Edition, 2009. **48**(13): p. 2308-2312.
151. Pirmohamed, T., et al., *Nanoceria exhibit redox state-dependent catalase mimetic activity.* Chemical Communications, 2010. **46**(16): p. 2736-2738.
152. André, R., et al., *V_2O_5 Nanowires with an Intrinsic Peroxidase-Like Activity.* Advanced Functional Materials, 2011. **21**(3): p. 501-509.
153. Sun, X., et al., *A Sensitive H_2O_2 Assay based on dumbbell-like PtPd-Fe3O4 nanoparticles.* Advanced Materials, 2013. **25**(1): p. 132-136.
154. Deng, H., et al., *Nanoparticulate Peroxidase/Catalase mimetic and its application.* Chemistry – A European Journal, 2012. **18**(29): p. 8906-8911.
155. Eberhardt, A.M., et al., *Immobilization of catalase from Aspergillus niger on inorganic and biopolymeric supports for H_2O_2 decomposition.* Applied Catalysis B: Environmental, 2004. **47**(3): p. 153-163.
156. Mu, J., et al., *Co_3O_4 nanoparticles as an efficient catalase mimic: Properties, mechanism and its electrocatalytic sensing application for hydrogen peroxide.* Journal of Molecular Catalysis A: Chemical, 2013. **378**: p. 30-37.
157. Triller, M.U., et al., *Preparation of highly efficient manganese catalase mimics* Inorganic Chemistry, 2002. **41**(21): p. 5544-5554.
158. Chen, W., et al., *Peroxidase-Like Activity of Cupric Oxide Nanoparticle.* ChemCatChem, 2011. **3**(7): p. 1151-1154.
159. Nagvenkar, A.P. and A. Gedanken, *$Cu_{0.89}Zn0_{.11}O$, A new peroxidase-mimicking nanozyme with high sensitivity for glucose and antioxidant Detection.* ACS Applied Materials & Interfaces, 2016. **8**(34): p. 22301-22308.
160. Zhao, H., et al., *Highly Dispersed CeO_2 on TiO_2 Nanotube: A Synergistic Nanocomposite with Superior Peroxidase-Like Activity.* ACS Applied Materials & Interfaces, 2015. **7**(12): p. 6451-6461.
161. Fan, J., et al., *Direct evidence for catalase and peroxidase activities of ferritin–platinum nanoparticles.* Biomaterials, 2011. **32**(6): p. 1611-1618.
162. Raynal, M., et al., *Supramolecular catalysis. Part 2: artificial enzyme mimics.* Chemical Society Reviews, 2014. **43**(5): p. 1734-1787.
163. Day, B.J., *Catalase and glutathione peroxidase mimics.* Biochemical Pharmacology, 2009. **77**(3): p. 285-296.
164. Garg, B. and T. Bisht, *Carbon nanodots as peroxidase Nanozymes for biosensing.* Molecules, 2016. **21**(12): p. 1-16.
165. Chelikani, P., I. Fita, and P.C. Loewen, *Diversity of structures and properties among catalases.* Cellular and Molecular Life Sciences CMLS, 2004. **61**(2): p. 192-208.

166. Vlasits, J., et al., *Hydrogen peroxide oxidation by catalase-peroxidase follows a non-scrambling mechanism.* FEBS Lett., 2007. **581**(2): p. 320-324.
167. Liang, M., et al., *Fe_3O_4 Magnetic Nanoparticle Peroxidase Mimetic-Based Colorimetric Assay for the Rapid Detection of Organophosphorus Pesticide and Nerve Agent.* Analytical Chemistry, 2013. **85**(1): p. 308-312.
168. Chacón-Patiño, M.L., et al., *Biocomposite of nanostructured MnO_2 and fique fibers for efficient dye degradation.* Green Chemistry, 2013. **15**(10): p. 2920-2928.
169. Singh, M., et al., *Rapid fabrication and optimization of silk fibers supported and stabilized MnO2 catalysts.* Fibers and Polymers, 2017. **18**(9): p. 1660-1670.
170. Remucal, C.K. and M. Ginder-Vogel, *A critical review of the reactivity of manganese oxides with organic contaminants.* Environmental Science: Processes & Impacts, 2014. **16**(6): p. 1247-1266.
171. Joshi, T.P., et al., *Adsorption of aromatic organoarsenic compounds by ferric and manganese binary oxide and description of the associated mechanism.* Chemical Engineering Journal, 2017. **309**: p. 577-587.
172. Tournassat, C., et al., *Arsenic(III) Oxidation by Birnessite and Precipitation of Manganese(II) Arsenate.* Environmental Science & Technology, 2002. **36**(3): p. 493-500.
173. Villalobos, M., I.N. Escobar-Quiroz, and C. Salazar-Camacho, *The influence of particle size and structure on the sorption and oxidation behavior of birnessite: I. Adsorption of As(V) and oxidation of As(III).* Geochimica et Cosmochimica Acta, 2014. **125**: p. 564-581.
174. Wang, Z., et al., *Uraninite oxidation and dissolution induced by manganese oxide: A redox reaction between two insoluble minerals.* Geochimica et Cosmochimica Acta, 2013. **100**: p. 24-40.
175. Wang, Y., et al., *Diffusion- and pH-Dependent Reactivity of Layer-Type MnO2: Reactions at Particle Edges versus Vacancy Sites.* Environmental Science & Technology, 2018. **52**(6): p. 3476-3485.
176. Shindo, H. and P.M. Huang, *Catalytic Effects of Manganese (IV), Iron(III), Aluminum, and Silicon Oxides on the Formation of Phenolic Polymers.* Soil Science Society of America Journal, 1984. **48**(4): p. 927-934.
177. Wang, Y. and A.T. Stone, *Reaction of MnIII,IV (hydr)oxides with oxalic acid, glyoxylic acid, phosphonoformic acid, and structurally-related organic compounds.* Geochimica et Cosmochimica Acta, 2006. **70**(17): p. 4477-4490.
178. Lin, K., C. Yan, and J. Gan, *Production of Hydroxylated Polybrominated Diphenyl Ethers (OH-PBDEs) from Bromophenols by Manganese Dioxide.* Environmental Science & Technology, 2014. **48**(1): p. 263-271.

179. Ukrainczyk, L. and M.B. McBride, *The oxidative dechlorination reaction of 2,4,6-trichlorophenol in dilute aqueous suspensions of manganese oxides.* Environmental Toxicology and Chemistry, 1993. **12**(11): p. 2005-2014.
180. Bertino, D.J. and R.G. Zepp, *Effects of solar radiation on manganese oxide reactions with selected organic compounds.* Environmental Science & Technology, 1991. **25**(7): p. 1267-1273.
181. Xyla, A.G., et al., *Reductive dissolution of manganese(III, IV) (hydr)oxides by oxalate: the effect of pH and light.* Langmuir, 1992. **8**(1): p. 95-103.
182. Kung, K.H. and M.B. McBride, *Electron Transfer Processes Between Hydroquinone and Iron Oxides.* Clays and Clay Minerals, 1988. **36**(4): p. 303-309.
183. Marafatto, F.F., B. Lanson, and J. Peña, *Crystal growth and aggregation in suspensions of δ-MnO_2 nanoparticles: implications for surface reactivity.* Environmental Science: Nano, 2018. **5**(2): p. 497-508.
184. Hirate, T., et al., *Effects of laser-ablated impurity on aligned ZnO nanorods grown by chemical vapor deposition.* Thin Solid Films, 2005. **487**(1): p. 35-39.
185. Wang, H., et al., *Preparation of nanocrystalline ceria particles by sonochemical and microwave assisted heating methods.* Physical Chemistry Chemical Physics, 2002. **4**(15): p. 3794-3799.
186. Sen, K. and K.M. Babu, *Studies on Indian Silk . I . Macrocharacterization and Analysis of Amino Acid Composition.* J. Appl. Polym. Sci., 2004. **92**(2): p. 1080-1097.
187. Babu, K.M., *Silk*. The textile institute book series. 2018: Woodhead Publishing.
188. Shaabani, A., H. Afaridoun, and S. Shaabani, *Natural hydroxyapatite-supported MnO2: a green heterogeneous catalyst for selective aerobic oxidation of alkylarenes and alcohols.* Applied Organometallic Chemistry, 2016. **30**(9): p. 772-776.
189. Broughton, D.B., R.L. Wentworth, and M.E. Laing, *Mechanism of Decomposition of Hydrogen Peroxide Solutions with Manganese Dioxide. II.* Journal of the American Chemical Society, 1947. **69**(4): p. 744-747.
190. Hasegawa, S., et al., *Surface active sites for dehydrogenation reaction of isopropanol on manganese dioxide.* Journal of Catalysis, 1977. **46**(2): p. 125-131.
191. Kanungo, S.B., K.M. Parida, and B.R. Sant, *Studies on MnO_2—III. The kinetics and the mechanism for the catalytic decomposition of H2O2 over different crystalline modifications of MnO2.* Electrochimica Acta, 1981. **26**(8): p. 1157-1167.
192. Chan, Z.M., et al., *Electrochemical trapping of metastable Mn 3+ ions for activation of MnO 2 oxygen evolution catalysts.* Proceedings of the National

Academy of Sciences of the United States of America, 2018. **115**(23): p. E5261-E5268.

193. Ryabova, A.S., et al., *Rationalizing the Influence of the Mn(IV)/Mn(III) Red-Ox Transition on the Electrocatalytic Activity of Manganese Oxides in the Oxygen Reduction Reaction.* Electrochimica Acta, 2016. **187**: p. 161-172.
194. Tebo, B.M., et al., *BIOGENIC MANGANESE OXIDES: Properties and Mechanisms of Formation.* Annual Review of Earth and Planetary Sciences, 2004. **32**(1): p. 287-328.
195. Gray, M.J., M.A. Malati, and M.W. rophael, *The point of zero charge of manganese dioxides.* Journal of Electroanalytical Chemistry and Interfacial Electrochemistry, 1978. **89**(1): p. 135-140.
196. Morgan, J.J. and W. Stumm, *Colloid-chemical properties of manganese dioxide.* Journal of colloid Science, 1964. **19**: p. 347-359.
197. Drozd, M., et al., *Pitfalls and capabilities of various hydrogen donors in evaluation of peroxidase-like activity of gold nanoparticles.* Analytical and Bioanalytical Chemistry, 2016. **408**(29): p. 8505-8513.
198. Jaumot, J., A. de Juan, and R. Tauler, *MCR-ALS GUI 2.0: New features and applications.* Chemometrics and Intelligent Laboratory Systems, 2015. **140**: p. 1-12.
199. Römer, L. and T. Scheibel, *The elaborate structure of spider silk.* Prion, 2008. **2**(4): p. 154-161.
200. Malay, A.D., et al., *Relationships between physical properties and sequence in silkworm silks.* Scientific Reports, 2016. **6**(1): p. 27573.
201. Zhang, Y., et al., *Antheraea pernyi silk fiber: a potential resource for artificially biospinning spider dragline silk.* Journal of biomedicine & biotechnology, 2010. **2010**: p. 683962-683962.
202. Martel, A., et al., *Silk Fiber Assembly Studied by Synchrotron Radiation SAXS / WAXS and Raman Spectroscopy.* 2008(20): p. 17070-17074.
203. Perumalraj, R., B.S. Dasaradhan, and G. Nalankilli, *Copper, stainless steel, glass core yarn, and ply yarn woven fabric composite materials properties.* Journal of Reinforced Plastics and Composites, 2010. **29**(20): p. 3074-3082.
204. Boschi, A., et al., *Properties and performance of polypyrrole (PPy)-coated silk fibers.* Fibers and Polymers, 2008. **9**(6): p. 698-707.
205. Chatterjee, A. and S. Maity, *A comparative study of reaction kinetics of in-situ chemical polymerization of polypyrrole onto various textile fibres.* Surface and Coatings Technology, 2017. **324**: p. 569-576.
206. Malhotra, U., S. Maity, and A. Chatterjee, *Polypyrrole-silk electro-conductive composite fabric by in situ chemical polymerization.* Journal of Applied Polymer Science, 2015. **132**(4): p. 1-10.
207. Yu, J. and J. He, *Preparation of conductive polypyrrole (PPy) composites under supercritical carbon dioxide conditions.* 2007(December 2014).

208. Harlin, A., et al., *Development of polyester and polyamide conductive fibre.* Journal of Materials Science, 2005. **40**(20): p. 5365-5371.

209. Tang, M., et al., *Synthesis of electrically conductive polypyrrole–polystyrene composites using supercritical carbon dioxide II. Effects of the doping conditions.* European Polymer Journal, 2003. **39**: p. 151-156.

Silks are diverse in form, quality, and cost. Silk fibers offer untapped internal structures to template the formation of nano-objects and active coatings. The aim of the thesis is to identify and exploit silk templating ability to create value-added multifunctional hybrid materials with enhanced conductive and catalytic properties.

Printed by Media-Tryck, Lund 2020 NORDIC SWAN ECOLABEL 3041 0903

LUND UNIVERSITY

ISBN: 978-91-7422-728-4

Pure and Applied Biochemistry
Faculty of Engineering
Lund University